FABRICATION OF ADVANCED CERAMIC COMPONENTS USING SLURRY-BASED THREE DIMENSIONAL PRINTING

by

SCOTT A. UHLAND

B.S., Ceramic Engineering
Rutgers – The State University of New Jersey, 1996

Submitted to the Department of Materials Science and Engineering in Partial Fulfillment of the Requirement for the Degree of

DOCTOR OF PHILOSOPHY
in Ceramics

at the
MASSACHUSETTS INSTITUTE OF TECHNOLOGY

September 2000

Signature of Author: Signature redacted
Department of Materials Science and Engineering
June 14, 2000

Certified by: Signature redacted
Professor Michael J. Cima
Sumitomo Electric Industries Professor of Materials Science and Engineering
Thesis Supervisor

Accepted by: Signature redacted
Professor Carl V. Thompson
Stavros Salapatas Professor of Materials Science and Engineering
Chairman, Departmental Committee on Graduate Students

FABRICATION OF ADVANCED CERAMIC COMPONENTS USING SLURRY-BASED THREE-DIMENSIONAL PRINTING

by

Scott A. Uhland

Submitted to the Department of Materials Science and Engineering
on June 14, 2000 in Partial Fulfillment of the
Requirements for the Degree of Doctor of Philosophy in
Materials Science and Engineering

ABSTRACT

Advanced ceramics have been manufactured using Slurry-Based Three-Dimensional Printing (S-3DP). This achievement is attributed to the development of a process standard for removing the imbedded printed components from the cohesive powder bed, i.e. the part retrieval process. The development of the part retrieval process was facilitated by identifying the strength of binder-free agglomerates, and controlling the counteracting redispersive forces and cohesive strength of the printed component. Existing fracture models were employed to resolve the dominant inter-particle force(s), namely van der Waals attraction and solid bridging phenomena, responsible for agglomerate strength, which ranged from 0.1 to 0.6 MPa. Deagglomeration was achieved by addition of polyethylene glycol (PEG) to the composition of the agglomerate. A PEG solution is formed within the agglomerated structure during redispersion. This resulted in an osmotic pressure gradient that forced water into the agglomerate, creating a tensile stress on the particle network with magnitudes as high as 0.6 MPa. Thus, the principle to achieving redispersion was to tailor the materials system such that the osmotic pressure exceeded the cohesive strength of the agglomerated structure. A cross-linkable polyacrylic acid based binder (2.5 vol.% : solids basis) was used to form green bodies capable of withstanding the redispersive osmotic forces. The resulting components exhibited green strengths that ranged from 0.7 MPa to 9.0 MPa. The efficacy of the binder was primarily dictated by adsorption of the polymer onto the ceramic surface. These three principles of part retrieval have been proven for a wide range of model oxide systems (TiO_2, SiO_2 and Al_2O_3) and are successfully applied to the $(1\text{-}x)BaNd_2Ti_5O_{14}$: xBi_2O_3 system to form components with complex geometries.

Thesis Supervisor: Michael J. Cima

Title: Sumitomo Electric Industries Professor of Materials Science and Engineering

Table of Contents

CHAPTER THREE

ADDITIVE ENHANCED REDISPERSION OF CERAMIC AGGLOMERATES

CHAPTER FOUR
THE MECHANICAL PROPERTIES OF GREEN CERAMICS WITH LOW BINDER CONTENT

CHAPTER FIVE
THE FORMATION OF S-3DP ADVANCED CERAMIC COMPONENTS

CHAPTER SIX
Conclusions

APPENDIX A
COLLOIDAL STABILIZATION THEORY AND MR2 SLURRY FORMULATION

List of Figures

CHAPTER ONE
INTRODUCTION

CHAPTER TWO
THE STRENGTH OF BINDER-FREE CERAMIC AGGLOMERATES

CHAPTER THREE
ADDITIVE ENHANCED REDISPERSION OF CERAMIC AGGLOMERATES

CHAPTER FOUR
THE MECHANICAL PROPERTIES OF GREEN CERAMICS WITH LOW BINDER CONTENT

CHAPTER FIVE
THE FORMATION OF S-3DP ADVANCED CERAMIC COMPONENTS

CHAPTER SIX
CONCLUSIONS

APPENDIX A
COLLOIDAL STABILIZATION THEORY AND MR2 SLURRY FORMULATION

List of Tables

CHAPTER TWO
THE STRENGTH OF BINDER-FREE CERAMIC AGGLOMERATES

CHAPTER THREE
ADDITIVE ENHANCED REDISPERSION OF CERAMIC AGGLOMERATES

CHAPTER FOUR
THE MECHANICAL PROPERTIES OF GREEN CERAMICS WITH LOW BINDER CONTENT

CHAPTER FIVE
THE FORMATION OF S-3DP ADVANCED CERAMIC COMPONENTS

to Stephanie, for your love and support

Acknowledgements

My four years at M.I.T. has been an invaluable time in my life. There have been many challenging periods during the four years that I have spent at M.I.T. These experiences have served to promote my professional development, while they have also given me the opportunity to develop many friendships.

First of all, I would like to thank my thesis advisor, Professor Michael Cima. He has been an important inspiration throughout my graduate education. His insight and encouragement have helped to foster a sense of intellectual curiosity that will remain with me for the rest of my life.

I would like to extend gratitude to my thesis committee members. Professor Emanuel Sachs has broadened my understanding of applied science through both his helpful suggestions and his expertise in solid freeform fabrication. I would also like to thank Professor Chris Scott and Professor Sandi Burkett for their discussions, which have been beneficial to the development of my research.

The members of the 3DP laboratory have been a tremendous help throughout my research at M.I.T, especially Jim Serdy and Dave Brancazio. Their compliance and eagerness have been major reasons for the success of my research. I am also very grateful to the Ceramics Processing Research Laboratory. Lenny Rigione, John Centorino and Barbara Layne are the foundation of the laboratory, and they have always been willing to offer their assistance. Past and present CPRL members have played an important role in my graduate experience, and special thanks go to Sherry Morissette for her encouragement.

I have been fortunate to have a chance to work with Richard Holman, a brilliant scientist and a good friend. We worked very well together and were able to generate great results. I value our friendship that we have developed over the last three years and good luck to you in the future.

Gregory Farrey has been a great friend throughout my college years at Rutgers and at M.I.T. I cherish the times we spent together as roommates, and they will always be the best of memories.

I would like to thank Richard and Barbara Stutzmann. You have become an important part of my life and you have given me the greatest inspiration of all... my wife and best friend, Stephanie.

Most importantly, I am grateful to Stephanie and to my parents, Albert and Anna. Without your love and strength, this would not have been possible.

Chapter One

Introduction

1.1. Motivation

Products incorporating ceramic components frequently demand properties and shapes that challenge contemporary forming techniques. This is particularly true for electronic ceramic components, which must continuously meet new electronic design specifications requiring a strict set of dielectric properties while possessing complex geometries with precise dimensions. These electronic ceramic parts are often an important component of hierarchical circuitry in a technology in which miniaturization is an ever-increasing driving force. It is well established that the macrostructure, as well as the microstructure, in such components are associated with the consolidation techniques used to create the shape. Thus, much of ceramics processing research has been focused on improving the reliability of existing forming processes, such as casting, molding, and pressing. More recently, many questions have arisen regarding the ability of such forming methods to address both the need for increasing complexity in shape and the need for responsiveness in product development. Shape restrictions, research costs and development delays force the rejection of ceramic components in favor of alternative design approaches. Even quickly accessible molding methods, coupled with green machining, can place many constraints on the shapes that can be reliably produced. Undercut features and narrow sections are difficult, if not impossible, to produce using standard forming methods. As a result, a flexible, more reliable processing technique is required for the fabrication of complex ceramic shapes in order to contend with other designs, or the market(s) for these components may face extinction.

1.2. Traditional Forming Techniques

This section outlines traditional ceramic consolidation techniques and addresses their disadvantages for forming complex shaped ceramic parts. Numerous literature sources[1-7] are available for full descriptions of each technique.

1.2.1. Tape Casting

Tape casting involves spreading a colloidal suspension over an impermeable substrate with a blade, yielding a film with a predetermined thickness. Slurries used for tape casting are typically well stabilized and have a high solids content. The impermeable substrate is a polymer carrier film that is rolled up as the tape is cast onto its surface. Volatile organic solvents are commonly used in order that the ceramic tape develops some cohesiveness prior to being rolled, since the cast tape can dry from only the top surface. One-sided drying can result in concentration gradients with respect to the powder and/or organic additives and is a significant problem for thicker tapes ($\geq$ 500 μm). These variations lead to difficulties such as cracking and warping due to differential shrinkages during drying and sintering. Components formed using tape casting suffer a major disadvantage because of the technique's limited shape capabilities. One example is in the electronic packaging industry in which many labor-intensive steps, which include multiple machining and stacking sequences, are required to form hybrid ceramic components.

1.2.2. Slip Casting

Slip casting is one of the oldest techniques for forming ceramic components. In this technique, a colloidal suspension is poured into a porous mold. A layer of consolidated powder forms at the mold surface as the slurry solvent system penetrates into the mold. This layer continues to increase in thickness as more solvent is drawn into the pores of the mold. The consolidated ceramic takes the shape of the mold's interior and can be either solid or hollow by removing the slurry prior to complete casting. Slip cast components are very limited in size and shape complexity. Large components necessitate very long casting times (thickness $\propto$ time^2) and they must survive large stresses developed during lengthy drying processes. Secondly, the shape is constrained to the shape of the mold and precise features are often impossible to produce. The characteristics of the ceramic powder used in the slip casting process are limited to a small average particle size with a large size distribution. Large particles will settle relatively quickly forming a gradient in slip cast density. A narrow size distribution can produce non-optimum packing thus reducing the cracking resistance during drying.

However, if the particle size is too fine, the particles can close off the pores of the mold increasing the casting times for a given thickness.

1.2.3. Injection Molding

Injection molding is a cyclic process in which a granular ceramic-binder mix is heated until softened, and then forced into a mold cavity. In this cavity, the mix cools and resolidifies to produce a part with the desired shape. A number of process-related problems include binder removal, dimensional stability, reproducibility and high tooling costs.[8] Typical formulations of the mix may contain polymers at concentrations ranging up to 60 vol.%, which causes many difficulties. Complete polymer removal, i.e. dewaxing, is a very challenging process due to its high concentration. A "skin" can form during the molding process usually resulting from excessive cavity pressure. Knit lines, also known as weld or flow lines, are flaws in a molded part that occur when two flow fronts meet. These defects can be caused by improper mold design and/or poor flow characteristics of the mix. Cracks are the most common defect. Their presence is highly dependent on shape complexity. The cracks are generally caused by localized stress concentration resulting from uneven packing during molding, the part geometry, and mold adhesion or non-uniform shrinkage during the dewaxing and cooling periods.

1.2.4. Pressing

Pressing is the simultaneous compaction and shaping of a powder or granular material, which is confined in a rigid die or a flexible mold. The ceramic powder used for pressing is typically in the form of spray-dried granules that contain organic additives. There are two general pressing techniques: dry pressing and isostatic pressing. Dry pressing is the process by which ceramic powders are consolidated inside a cavity into a predetermined shape by applying pressure in a uniaxial direction. Dry pressing is a common technique used for the automated production of many components. However, this technique is restricted to ceramic parts with basic shapes and low length-to-diameter ratios. Packing density variations are typically present due to the non-uniform filling of the die and/or stress gradients resulting from die wall effects. These variations usually produce warped, fired components. Isostatic pressing consolidates powder by uniformly applying pressure in all directions. The process is accomplished by enclosing the powder

in a deformable mold and then collapsing the mold by applying pressure using a fluid medium. In general, isostatic pressing has two major disadvantages. This process is limited to shapes with simple internal features. In addition, the shape and dimensional control is very poor with tolerances of only ±8%.

Generally, these traditional processing techniques require additional green machining steps in order to produce the required shape complexity. Despite the use of green machining, many constraints still exist, such as the inability to precisely produce undercut features, internal sections and narrow walls. Even when these standard methods are accessible, costly tooling equipment and long product delivery periods are necessary. Finally, the product yield can be relatively low due to the many labor-intensive steps during the processing of traditionally "brittle" materials. These drawbacks add to the cost of the ceramic components and limit their use as advanced materials.

Over the last twenty years, many studies have been carried out with the objective of increasing the speed and reliability with which the ceramic components are manufactured, particularly those with complex shapes. A new group of processing techniques, known as "Solid Freeform Fabrication" has emerged in order to meet this demand.

1.3. Ceramic Solid Freeform Fabrication Processes

Many Solid Freeform Fabrication (SFF) technologies have emerged because of the global demand for cheaper processing techniques with shorter product development cycles. All SFF methods share the feature that components are constructed through sequential lamination of thin sections. Each section represents a cross section of the component chosen at a position along and perpendicular to a vector selected through the component. This vector is known as the "build direction" for the particular fabrication session and is selected to optimize part specifications, such as dimensional precision, surface finish, and dielectric properties. The information required to prepare each section is most conveniently obtained from a "solid model" of the component. The term, solid model, refers to the subset of computer-aided-design (CAD) descriptions of parts in which the component is represented as the union of mathematically described surfaces.

Numerous SFF technologies have been developed and many classification systems exist. The following sections review some of the more popular SFF techniques for the fabrication of ceramic components, while highlighting their weaknesses in terms of their applicability for ceramic manufacturing.

1.3.1. Stereolithography (SLA)

Stereolithography is an example of an SFF technique that uses light/photon energy to pattern the layered structure, as shown in Figure 1- 1. Stereolithography uses lasers (ex: HeCd) to cure liquid polymers, which develops the pattern for each layer. The cured component(s) is then lowered into the liquid polymer bath a distance equal to the prescribed layer thickness. The newly deposited polymer layer is polymerized to form the subsequent layer. Once the curing process is complete, part retrieval is accomplished by raising the underlying platform to allow the uncured polymer to flow away from the cured components. A post-curing step is often necessary in order to achieve complete polymerization. Ceramic green bodies can be created with stereolithography by utilizing a curable suspension of a ceramic powder[9-11]. To date, several ceramic materials have been used to form parts, including Al_2O_3, Si_3N_4 and SiO_2.

There are several important disadvantages with for forming ceramics using SLA. The ceramic green body is formed from a "resin" containing 40-55% powder and 45-60% curable polymer. Similar to injection molding, these high polymer contents prove unfavorable for several reasons. High strains result upon polymer removal, which produces defects such as shape distortions and large internal voids. Long pre-sintering "burn-out" steps are needed in order to eliminate residual carbon in the ceramic body. These processing steps may prove unsuccessful due to limitations in temperature and atmosphere. The development of a fully diversified range of ceramic material systems is challenging due to the complex chemistries required for resin stabilization. Furthermore, formulated resins are often toxic and involve careful handling procedures. Undercut features pose a shape constraint in that they require temporary support structures to be incorporated into the forming process, since polymerization is not instantaneous[12].

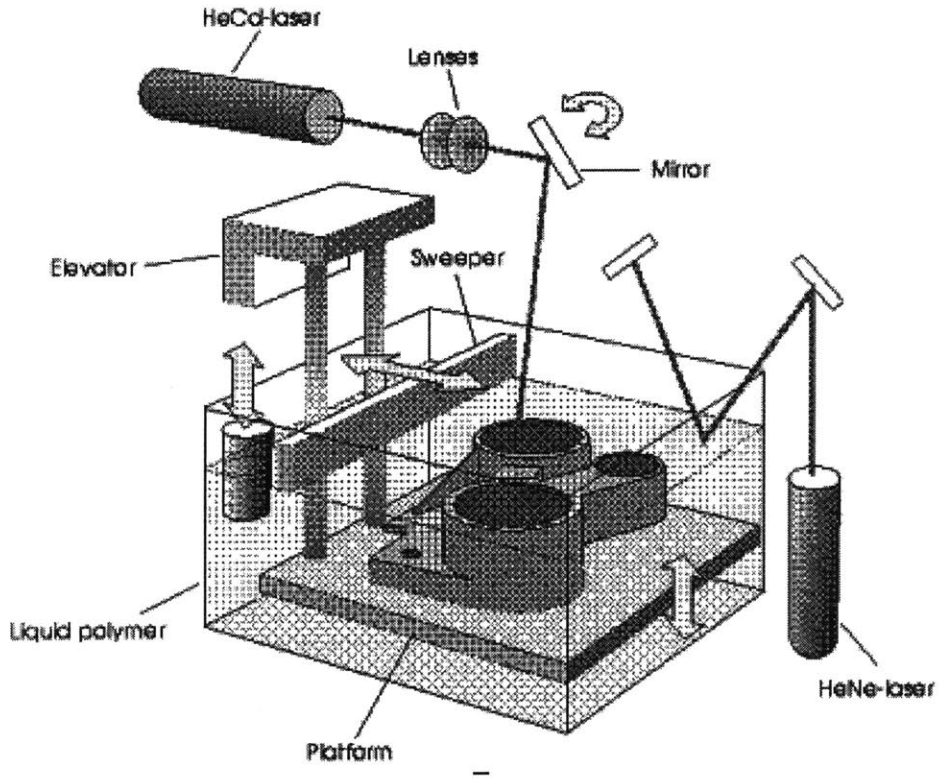

Figure 1- 1: Stereolithography (SLA).[13]

1.3.2. Selective Laser Sintering (SLS)

Selective laser sintering is another technique based on the application of light/photon energy to define each layer of the SFF components. SLS uses a laser to form each layer by fusing ceramic particles, which have been coated with a thermoplastic binder (see Figure 1- 2). The laser is directed by rotating mirrors that are positioned based on the respective CAD information. The piston is lowered once a layer has been fused and a new layer of unbound powder is rolled evenly across the powder bed surface. Once the component is complete, the unbound powder is brushed away and the green part is removed.

Many materials, including Al_2O_3[14], SiC[15] and Zr composites[16], have been used to fabricate components using the SLS technique. The components formed using SLS typically exhibit a very poor surface finishes. The high roughness results from the hardening of the powder near the thermal "boundary" of the outlined layer and additional tooling may be required in order that the component meet dimensional specifications[17]. Another limitation is a size restriction of the starting powder. The ability to spread a dry powder places constraints on the size and form of the powder. Generally, large particle (>10 μm) or spray-dried granules must be used to avoid agglomeration and ultimately low density powder beds. These relatively large particles reduce the driving force for sintering while the granules form large pores, making it difficult to sinter to fully density. Infiltration and/or high pressure sintering steps may be used to achieve near-theoretical densities.

1.3.3. Laminated Object Manufacturing (LOM)

The laminated object manufacturing technique uses a computer-controlled laser to cut the respective layer pattern from pre-formed "sheets" of material. The cutting path is determined from the CAD model of the part being manufactured. The laser cuts the tape to create the first layer. A second sheet of material is pressed and laminated to the

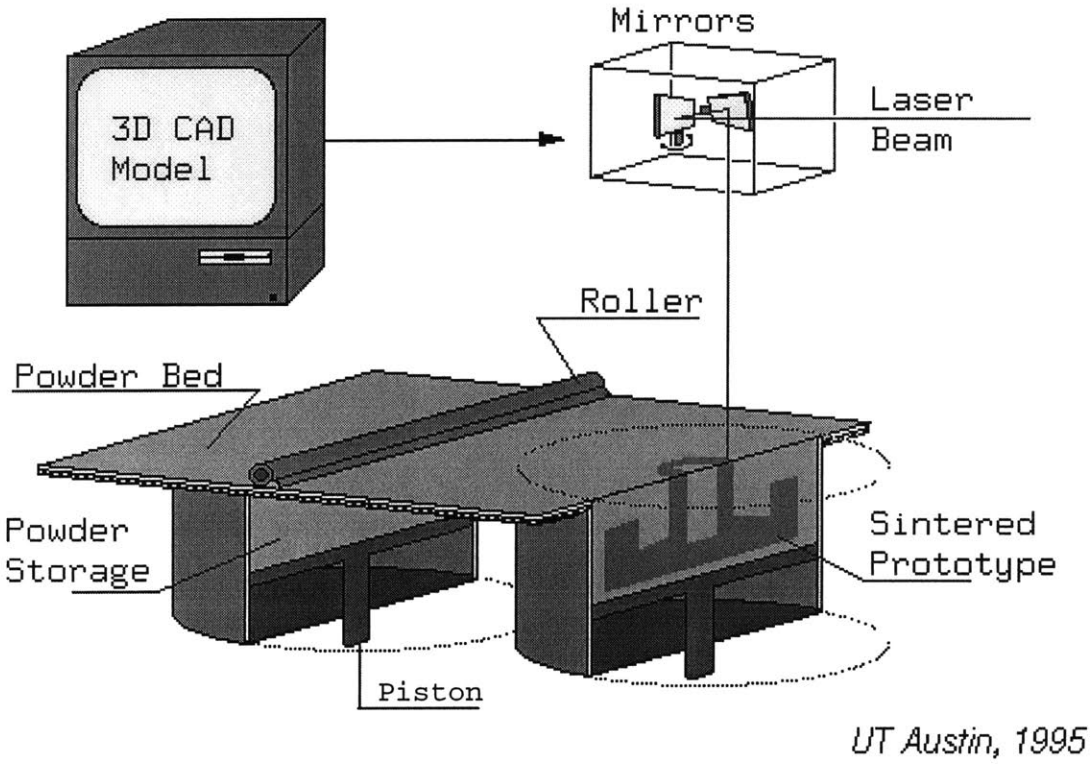

Figure 1- 2: Selective Laser Sintering (SLS). [18]

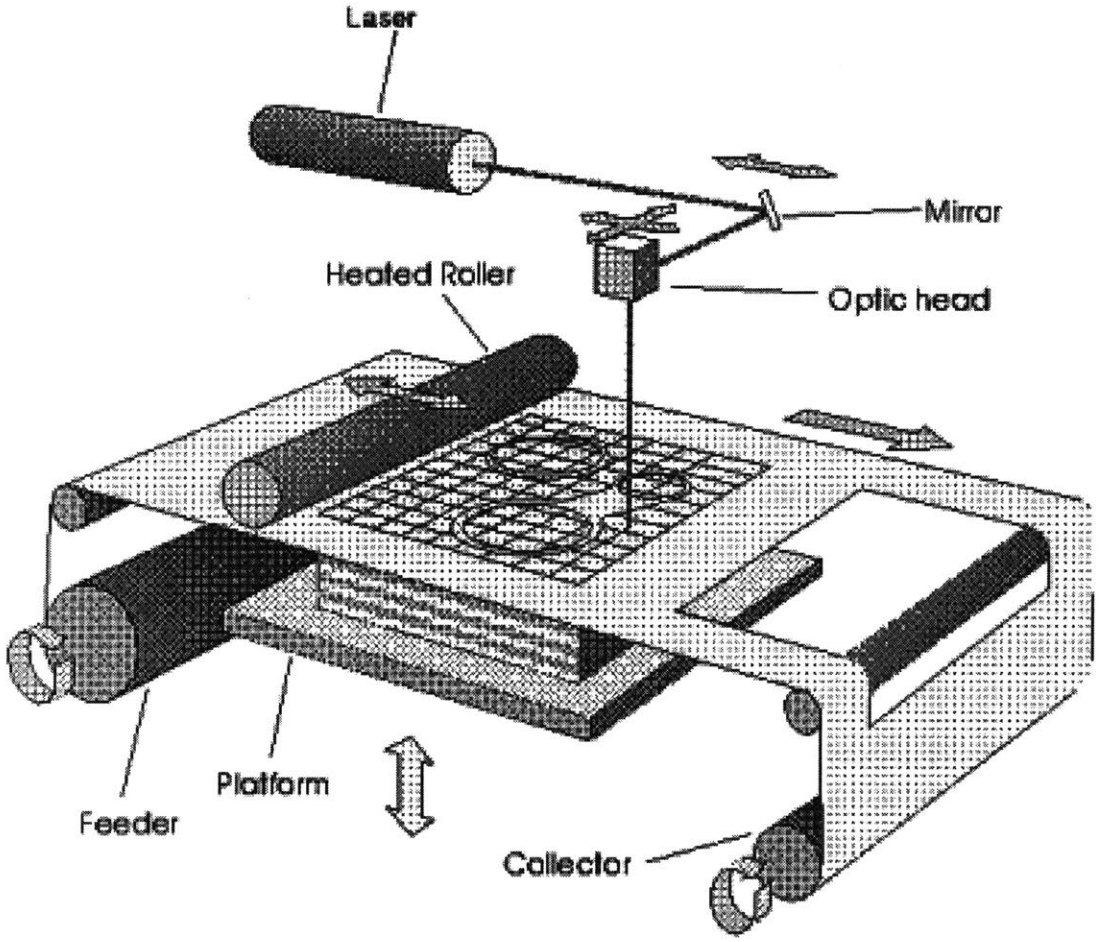

Figure 1- 3: Laminated Object Manufacturing (LOM).[13]

previous layer, and the second layer is laser patterned[19]. This process is repeated until the component is completed, as illustrated in Figure 1- 3. LOM has been successfully demonstrated for the manufacturing of structural ceramics[20,21]. The most successful results were based used Ce-ZrO_2 and Al_2O_3 composites. Klosterman, et al.[22] have manufactured SiC component using LOM, coupled with reaction bonding processing methods. The mechanical properties of the LOM parts were found to be within the range of traditional reaction bonded SiC.

Essentially, LOM requires the integration and complete compatibly of an entirely different processing technique: tape casting. While the previously outlined difficulties with respect to tape casting must be considered, LOM also requires the tape cast sheets to form strong bonds or delamination defects will be present the component. Other limitations with LOM are with respect to shape capabilities. Hollow parts with thin walls are difficult to produce by cutting a laminate structure, while poor surface finishes may result from inefficient cutting of the sheet material[17]. LOM components contain high levels of polymer, representing many challenges similar to those in the SLA process.

1.3.4. Computer Aided Manufacturing of Laminated Engineering Materials

The principles involved for Computer Aided Manufacturing of Laminated Engineering Materials (CAM-LEM) are very similar to those in LOM. CO_2 lasers are used to pattern layers from pre-formed ceramic sheets. The layers are then robotically assembled to reconstruct the structure (see Figure 1- 4). Lamination is achieved using conventional warm isostatic pressing methods. Silicon nitride and alumina[23] components have been fabricated using this technique.

The disadvantages of the CAM-LEM technique parallel those for LOM. CAM-LEM offers improved surface features, due to the ability to form beveled edges. An added limitation is the inability to form large undercut features in the plane perpendicular to the building direction.

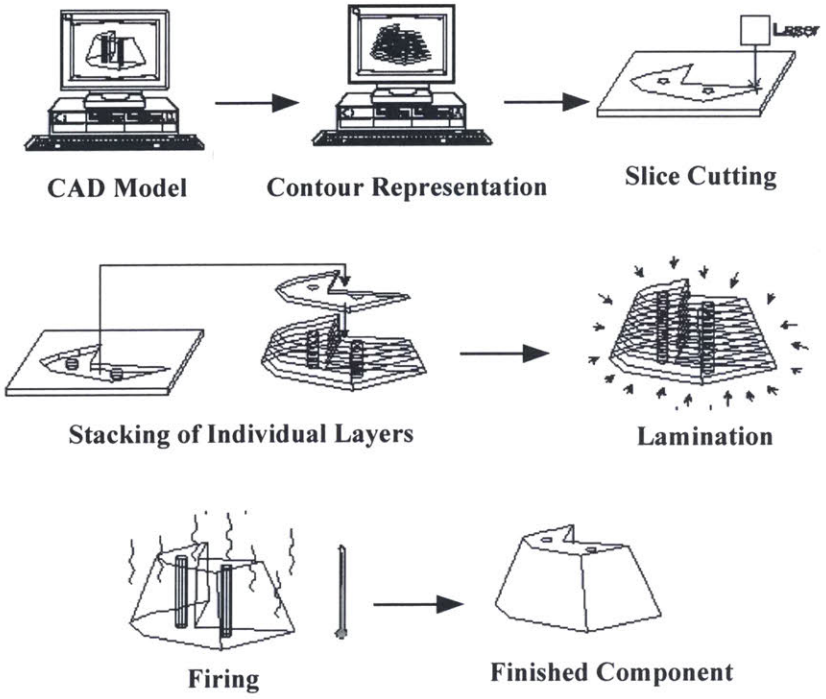

Figure 1- 4: Computer Aided Manufacturing of Laminated Engineering Materials (CAM-LEM).[24]

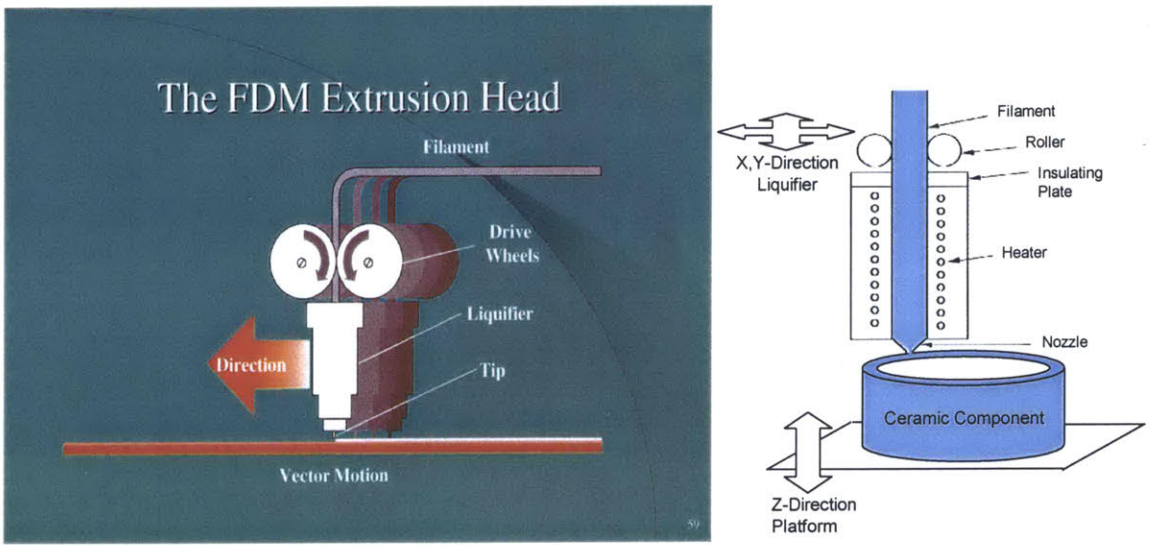

Figure 1- 5: Fused Deposition Modeling (FDM).[13]

1.3.5. Fused Deposition Modeling (FDM)

Fused deposition modeling is a technique based on the extrusion of a polymer/wax filament, which is used as a carrier and binder for the powdered material. The material is deposited in vector-scanning fashion. The layers are formed from flowing a filament material out of a heated extrusion head, as pictured in Figure 1- 5.

The FDM process has been used to form SiO_2, Al_2O_3 and PZT components. Agarwala et al,[25] have also used the FDM process to manufacture Si_3N_4 parts. The green component contained nearly 47% polymer with a density of ~52%. The fired density was 98%, after hot pressing. The fired-shrinkages were anisotropic (~16% x-y and >19% z) while the mechanical properties had a large variance with an average below that of conventional hot isostatic pressed parts. Nearly half of the component's volume is a polymer, which must be removed prior to solidifying the porous body. Other detrimental characteristics include shape distortions due to variations in the flow properties of the filament. This results from the lack of temperature control and the presence of thermal gradients in the component. Again, additional support structures are needed in order to form undercut features, while the dimensional accuracy is limited by the size of the filament, which tends to be ~1.0 mm in diameter.

1.3.6. Three Dimensional Printing (3DP)

One very versatile SFF technique is the 3DP process, which is illustrated in Figure 1- 6. 3DP is based on granular raw material that is selectively glued together. The granular material is spread in a thin layer onto a piston, the bottom of which can be lowered by small increments. An ink-jet printer, suspended above the piston, is used to selectively deposit binder in the layer. This binder locally glues together particles within the layer and to the layer below. The piston is then instructed to lower and the next layer of the powder is deposited. Only selected volume elements of the powder bed are thereby bound together and, at completion of the last layer, the unbound powder may be removed to expose the component. In most cases, the resulting component is green and must be fired or post processed to achieve its final strength and density. The process has been used to make ceramic, metal, and polymer parts[26-29].

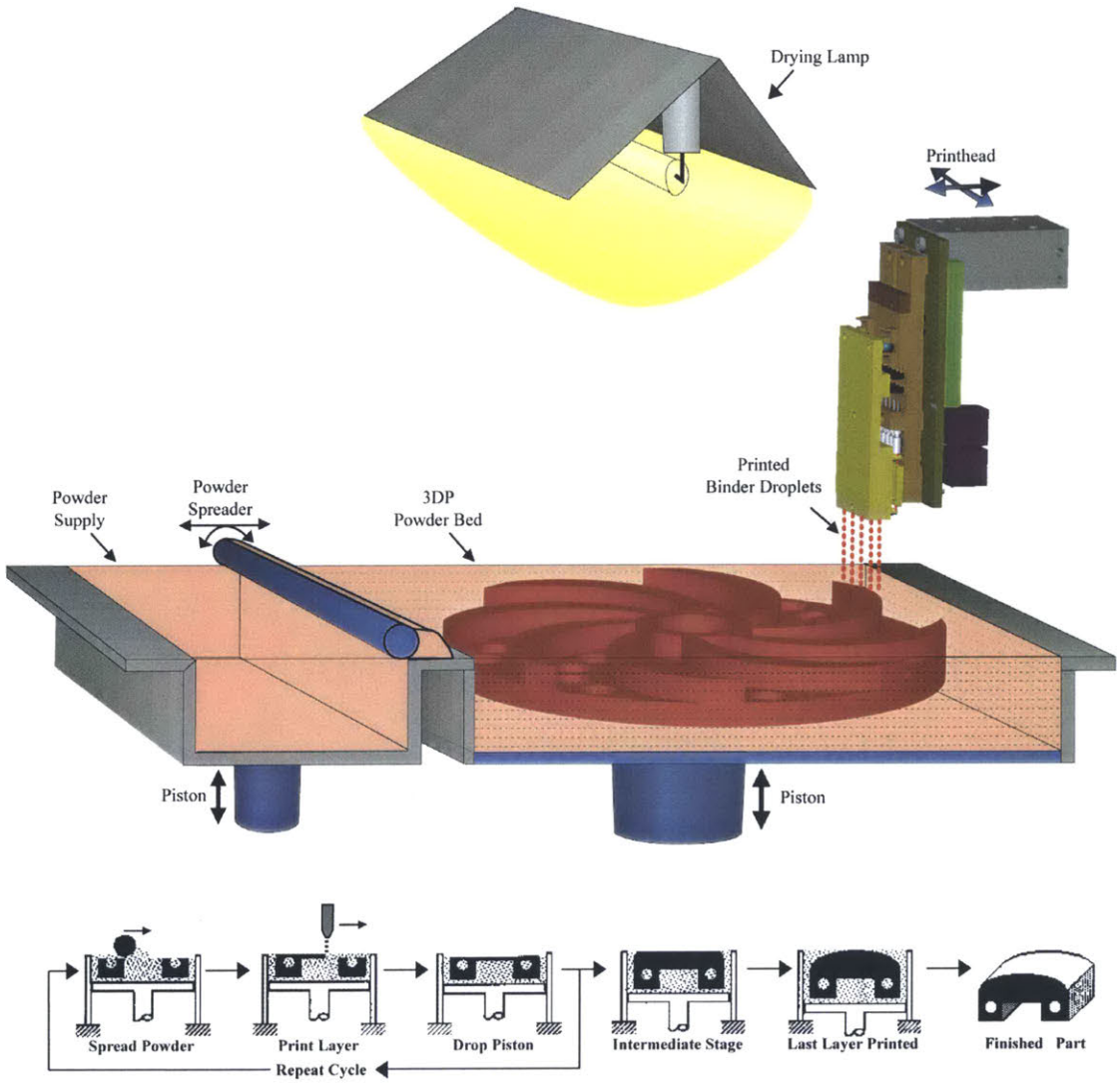

Figure 1- 6: Three Dimensional Printing (3DP).

The nature of the 3DP process places limitations on the range of powder sizes that can be used in the 3DP process[30,31]. The powder material must be sufficiently large so that the particles spread easily. Fine powders do not flow well enough to spread into defect-free layers due to van der Waals attractive forces or water vapor condensation at the particle contacts. This particle size limitation poses a severe challenge for direct use of the dry-powder based 3DP to fabricate dense ceramic components.

The particle size of the ceramic powder is an important factor in the sintering process. Densification mechanisms occur by transport of the ceramic species to the particle necks along many possible paths (Figure 1- 7). The driving force for diffusional processes results from the relatively high chemical potential of vacancies at the particle neck. The increase in the chemical potential can be calculated as

$$\Delta\mu = (RT\ln c - RT\ln c_o), \tag{1.1}$$

where c is the vacancy concentration at the neck and c_o is the equilibrium value over a flat surface. The relationship between average particle size and vacancy concentration can be calculated using the pressure difference across a curved surface[32],

$$c = c_o \exp\left[\frac{\gamma V_m}{RT}\frac{2}{r}\right]. \tag{1.2}$$

Smaller particles increase atomic mobility and therefore producing a greater driving force for densification.

Fine particle size is not the only prerequisite for producing high quality dense ceramics. Uniform, dense microstructures are critical in order to sinter the ceramic to full density. The removal of pores from the green state depends on their stability. Pore stability is controlled by the boundary curvature between the pore and grain phases. The curvature is dependent on both the dihedral angle, ϕ, at the pore boundary intersection

$$\cos\frac{\phi}{2} = \frac{\gamma_{gb}}{\gamma_s}, \tag{1.3}$$

Transport #	Transport Path	Source of Atoms	Sink of Atoms
1	Surface Diffusion	Surface	Neck
2	Lattice Diffusion	Surface	Neck
3	Vapor Transport	Surface	Neck
4	Boundary Diffusion	Grain Boundary	Neck
5	Lattice Diffusion	Grain Boundary	Neck
6	Lattice Diffusion	Dislocations	Neck

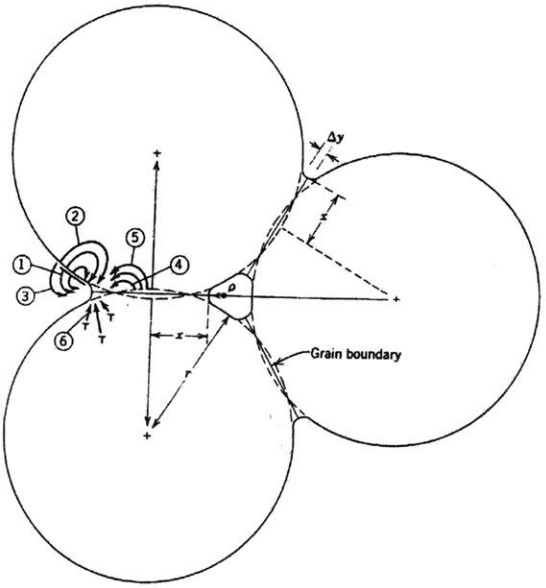

Figure 1- 7: Various Transport Processes During Sintering.[33]

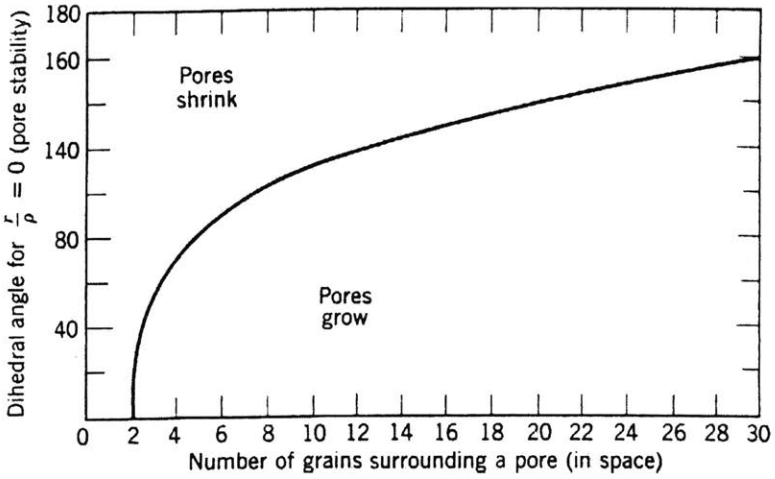

Figure 1- 8: Conditions for pore stability.[33]

where γ_{gb} and γ_s are the grain boundary and surface interfacial energies, and on the number of surrounding particles (grains). Kingery[33] has defined the relationship between the boundary dihedral angle and the number of surrounding grains for pore stability, i.e., $r/\rho = 0$, where r = radius of circumscribed sphere containing the pore and ρ = radius of curvature at the grain-pore interface. Pore stability is reduced as the number of surrounding grains decreases, as shown in Figure 1- 8. Typical dihedral angles in many oxide systems are ~ 110° and in order to develop the necessary driving force to eliminate pores, they must be surrounded by ~ 8 grains or less. Therefore, an efficiently compacted powder is necessary for complete pore removal during sintering processes.

Additionally, uniform microstructures are essential for producing components with high strengths. A major aspect of the strength is its importance during the handling of the powder compact. Large flaws in the green body act as stress intensifiers that decrease the component's resistance to applied stresses encountered during post-consolidation steps, consequently producing failures. Moreover, gradients in pore sizes and concentrations lead to differential shrinkages that produce strains within the sintered body. These internal strains can lead to warping of the ceramic components while larger stresses may produce fractures.

The functionality of advanced ceramics is highly dependent on their microstructure[34]. Clearly, a major modification to the 3DP process is necessary so that the process is capable of generating uniform components with high green densities using fine powders. A colloidal processing technique is necessary to meet these requirements[35].

1.4. Slurry-Based Three Dimensional Printing (S-3DP)

Colloidal processing techniques have been integrated into the 3DP process in order to generate ceramic components with high green densities using fine powders, i.e., slurry-based 3DP (S-3DP)[36] and is described in detail by Grau[37]. Figure 1- 9 illustrates the S-3DP process flowchart. The powder bed is formed by dispensing a slurry through a nozzle, which is raster-scanned over a porous substrate. The binder is printed into the

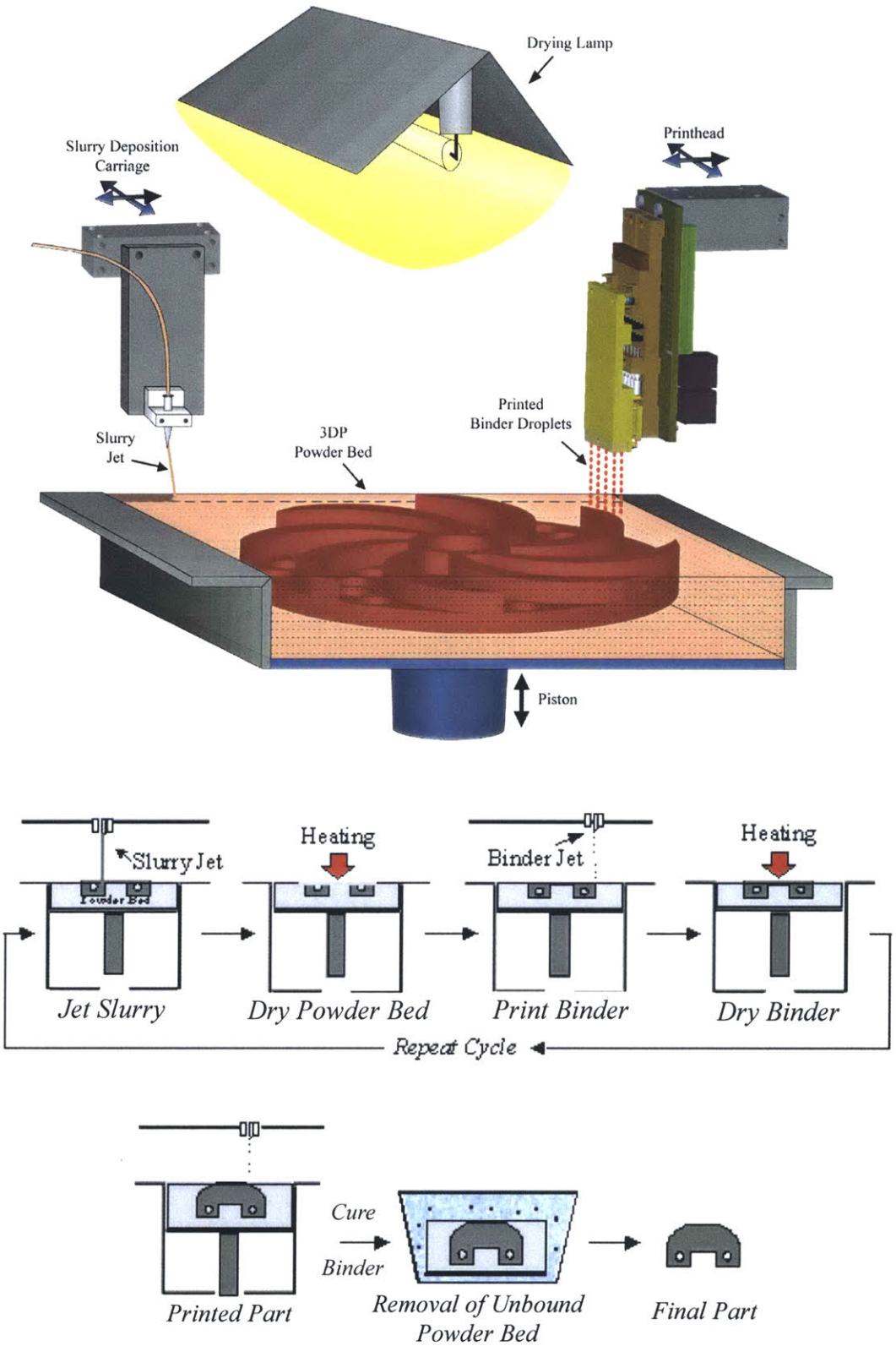

Figure 1- 9: Slurry-Based Three Dimensional Printing (S-3DP).

powder bed to define the shape of the component by the selective placement of binder droplets. Drying steps are performed in order to provide open pore space for the infiltration of the binder. The process is repeated until the component is completed. An important characteristic of the slurry-based 3DP process is that the printed parts are imbedded within the powder bed matrix. The unprinted powder bed is cohesive due to the slip casting nature of the powder bed fabrication process. Retrieving the imbedded components from this brick-like structure is therefore a critical step and is typically accomplished by manually brushing away the unprinted powder bed in a water bath.

1.4.1. Initial S-3DP Advanced Ceramics

Ceramic components have been formed using the slurry-based 3DP process. The macrostructural capabilities, was well as reliability, of the part retrieval process were inadequate with respect to the processing requirements outlined in Chapter One. Typically, failures occurred during the part retrieval process due to delaminations, as illustrated in Figure 1- 10a. The labor-intensive part retrieval process generally introduced erratic shape deformations to the remaining parts (Figure 1- 10b and Figure 1- 10c). Dimensional control was nonexistent since the geometry of parts was defined by gentle "rubbing" and brushing of surfaces, while more intricate features were essentially "carved out" with dental tools (see Figure 1- 10a). Parts that endured the retrieval process were typically short-lived because of delaminations during the sintering process.

Another primary source for the dimensional deficiencies of slurry-based 3DP was the binder system. The binder system used for the fabrication of the preliminary components was a styrene-acrylic co-polymer (Joncryl®, S C Johnson). This polymer system produced very fragile parts that fractured easily during part retrieval process. Moreover, internal features had to be shaped manually since sonication would quickly deteriorate the geometry (Figure 1- 10c). Higher binder concentrations (~10 vol.%) were used in order to minimize defect generation. Unfortunately, while the defects remained intact, new flaws developed in the components, such as poor part resolution due to binder bleeding and differential slip casting defects.

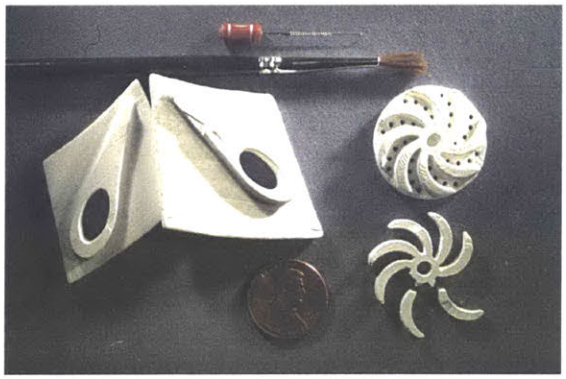

a)

b)

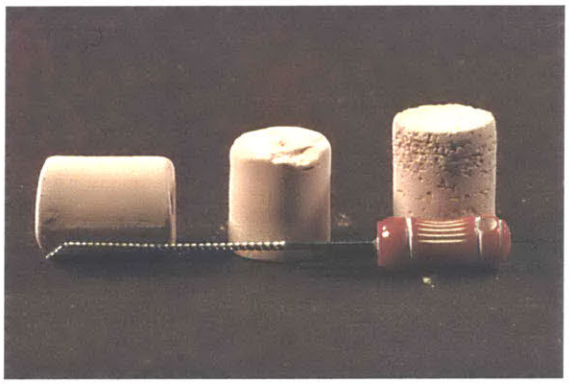

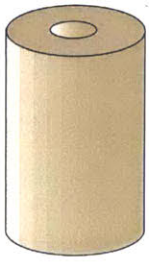

c)

Figure 1- 10: a) Delaminated Al_2O_3 Stators (left), Fractured Al_2O_3 Rotors (right), Redispersion Tools (top), b) Fractured Si_3N_4 Rotors with Rough Surfaces and c) Deformed $(1-x)BaNd_2Ti_5O_{14} : xBi_2O_3$ RF Resonators.

Binder–powder bed interaction plays an important role in controlling printing resolution, surface finish, and microstructure of the 3DP part. An important aspect of the binder–powder bed interaction is a differential casting effect of the slurry during the powder bed formation. The effect of the binder system on part formation in the slurry-based 3DP process has been defined by Grau[37], who used the model of Aksay and Schilling[38] to calculate the casting rates of the slurry. The casting process is a colloidal filtration in which the solvent in the slurry is removed rapidly from the thin layer of slurry. The filtration rate is dependent upon the viscosity of the solvent in the slurry, the pore fraction and pore size of the powder bed, and the contact angle of the liquid on the solid. The rate of colloidal filtration is expected to differ locally for slurry-based 3DP powder beds since selected regions are printed with a polymeric binder solution. The regions in the powder bed that are printed with binder will have different pore structures and wetting behavior than regions that do not contain binder.

The casting rate of the slurry was much lower over the binder-printed region than over the unprinted region when using the Joncryl binder system. It was observed that the slurry caste quickly over the region that was not printed with binder, while the slurry remained fluid over the region printed with binder. Slurry migrated from the binder-printed region towards the surrounding unprinted powder bed. The differential casting kinetics produced major structural defects (illustrated in Figure 1- 11a), which are described as: a bump at the interface of the binder-printed region; increased surface roughness on the printed region; a curved top surface; depression of the printed surface; and two distinct packing densities, i.e., $\rho_{part} \neq \rho_{powder\ bed}$.

Appreciable differential casting defects develop when using the Joncryl binder system. The casting defects for Si_3N_4 and $(1\text{-}x)BaNd_2Ti_5O_{14}$: xBi_2O_3 S-3DP powder beds are shown in Figure 1- 11b and Figure 1- 11c. Large depressions (> 600 μm) are visible, which produced components with deformed surfaces. Two methods were used to attempt to over come these structural defects. A razor blade was used to "plane" the top surface of the powder bed, which was required about every 10 to 15 layers throughout the build. Parts produced using the shaving process delaminated along many different layers during the part retrieval process. A second technique was based on decreasing the binder

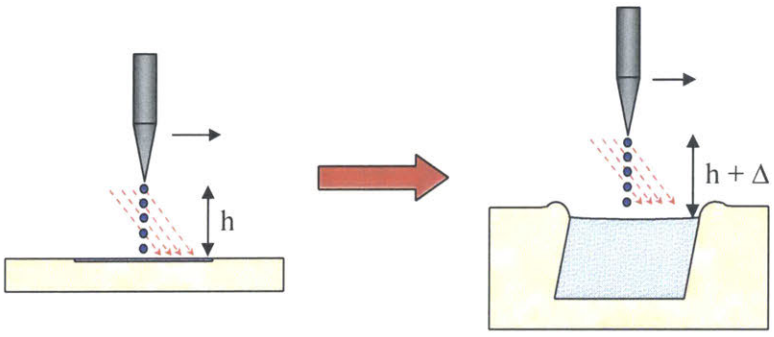

a)

b)

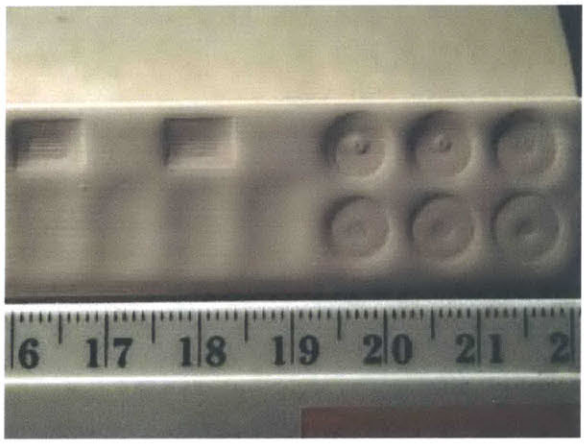

c)

Figure 1- 11: a) Schematic illustration of Differential Casting Defects[39] and Surface Depression and Defects due to Differential Slip Casting for b) Si_3N_4 and c) (1-x)$BaNd_2Ti_5O_{14}$: xBi_2O_3 Powder Beds.

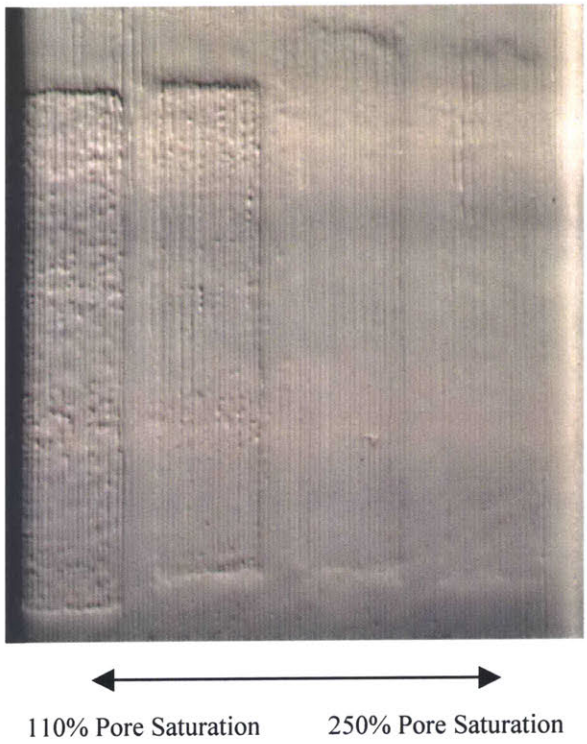

Figure 1- 12: 3DP Al2O3 Parts Illustrating Differential Casting Defects as a Function of Binder Solution Pore Saturation at Constant Binder Solids Concentration.

printing solution concentration and increasing the binder solution saturation (Figure 1- 12) in order to maintain the same overall binder content in the part. The high printing saturations effectively "washed" out the binder printed interface and reduced casting differences. Unfortunately, this "washing" technique also resulted in poor part resolution due to binder bleeding. The prescribed printing parameters produced binder-printing saturations in excess of 200% of the part's pore volume. Obviously, generating parts with complex geometries and precise dimensions is nearly impossible using these techniques.

1.5. Theme and Organization of the Thesis

Clearly, the primary processing issues that control part retrieval must be analyzed and mastered in order to manufacture advanced ceramic components using the S-3DP process. The two key topics are identified as: powder bed redispersion and the binder system. Reliable part retrieval requires the unprinted powder bed to redisperse easily. The first step to improving redispersion is to understand the factors that control the strength of the binder-free powder bed. Chapter Two discusses the mechanical properties of binder-free "agglomerates" in detail. The cohesive strength of dry binder-free agglomerated TiO_2, SiO_2, Al_2O_3 and MR2 ($(1-x)BaNd_2Ti_5O_{14}$: xBi_2O_3, TDK, Japan) ceramic bodies is correlated to microstructural observations using existing fracture models, which provide information with respect to the inter-particle cohesive forces.

Chapter Three examines the enhanced redispersion of dense ceramic compacts that contain a water soluble polymer. More specifically, the redispersion of S-3DP powder beds containing PEG is studied as a function of polymer concentration and molecular weight. The induced osmotic stresses are compared to the cohesive strength of the agglomerated structure. The ceramic system used to model these phenomena is titania. The redispersion principles that are outlined by the TiO_2 system are also applied to the SiO_2, Al_2O_3 and MR2 ceramic systems.

Chapter Four explores the binding mechanisms as a function of ceramic surface chemistry using a cross-linkable polyacrylic acid (PAA). PAA is an excellent candidate because it is representative of a class of acrylic based polymers that are commonly used

as binder systems for many different ceramic forming processes. Additionally, PAA can be crosslinked using a variety of techniques, which allows for excellent control over the mechanical and chemical properties of the binder phase. The ceramic systems investigated are SiO_2, TiO_2, Al_2O_3 and MR2, which represent a wide range of surface chemistries. The mechanical properties are measured and compared with the binder-free counterparts. The impact of the crosslinked PAA binder on the strength and fracture toughness of the green bars is contrasted with PAA's mechanical and surface adsorption characteristics.

Chapter Five defines the part retrieval mechanism by uniting the results of Chapters 2 through 4. This mechanism is applied to fabricate MR2 advanced ceramic components using S-3DP. The process and the properties of the resulting components are analyzed. Chapter 6 concludes the dissertation by summarizing the results and outlining key areas of research for future S-3DP applications.

Chapter Two

The Strength of Binder-Free Ceramic Agglomerates

2.1. Introduction

The term agglomerate is used to describe cohesive particulate bodies that are present during a wide range of processing methods and procedures. Agglomeration commonly occurs contrary to processing objectives during the storage, grinding and mixing of powders. On the other hand, many practices exist which target the systematic formation of agglomerated bodies. Several consolidation examples include granulation, powder compaction and solid freeform fabrication techniques such as Slurry-Based Three-Dimensional Printing (S-3DP)[40].

The strength of agglomerates is of considerable importance for many stages during the processing of ceramic powders. Agglomerates able to withstand consolidation processes produce large flaws in the compacted green bodies. These flaws yield inadequate densification rates and often remain within the sintered body[34,35]. One specific processing technique that requires deagglomeration is the S-3DP part retrieval process, during which complex-shaped parts are removed from a cohesive powder compact. Understanding agglomerate strength will help to facilitate part retrieval from the binder-free agglomerated matrix. The strength of agglomerates also plays an important role in a compact's resistance to fracture during drying and impact. Knowledge of the fracture characteristics will reduce the defects produced during manufacturing.

2.2. The Strength of Agglomerated Ceramic Bodies

Many fracture models have been developed that relate the strength of an agglomerate to its primary microstructural characteristics. Rumpf[41] was one of the first to derive a general expression for a compact's mean theoretical tensile strength as a function of particle size, packing density and inter-particle force(s).

Figure 2- 1 schematically represents the cross-sectional area for a fracture plane within the agglomerate. Rumpf's model is based upon many important assumptions regarding the physical properties of the agglomerate. They are:

1. the agglomerate is composed of mono-sized spherical particles,
2. the particles and their respective cohesive forces are distributed randomly throughout the particle,
3. the number of particle–particle contacts is high for a given cross section,
4. the stressed cross section is homogeneous,
5. fracture occurs straight across void space and
6. all inter-particle bonding forces throughout the agglomerate structure have the same average value.

Rumpf calculated the average tensile strength by summing the projections of all cohesive forces in the tensile direction, which resulted in the following equation:

$$\sigma = \frac{9\phi}{32\pi r^2} z F_A, \tag{2.1}$$

where ϕ is the packing fraction of the particles, r is the particle radius, z is the average number of contacts per particle and F_A is the inter-particle force. Assuming a close–packed structure, the average number of contacts per particle as a function of packing density has been calculated by Smith *et. al.*[42] to be:

$$z \approx \frac{3}{1-\phi_P}. \tag{2.2}$$

Substituting Eq. 2.1 into Eq. 2.2 yields the expression for the tensile strength as:

$$\sigma = \frac{27\phi}{32(1-\phi)\pi r^2} F_A, \tag{2.3}$$

Rumpf's theory for the strength of agglomerates has been applied to ceramic systems. Kamiya[43] has shown that the strength of Si_3N_4 granules increases with small additions of dispersant, in which case the additive acts as a binder, thus increasing F_A.

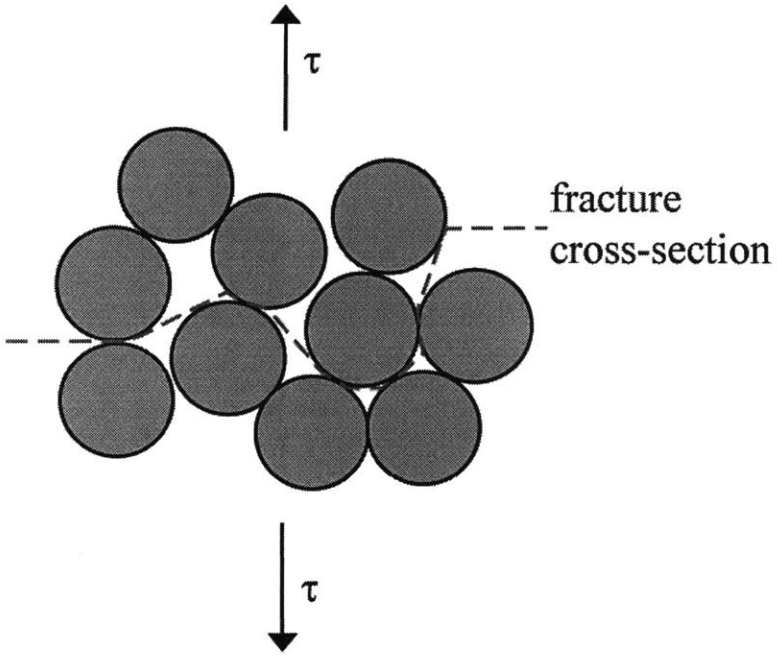

Figure 2- 1: Model Fracture Geometry.

Kuhn[44] has also used Rumpf's theory to describe the increase in strength of ceramic agglomerates having higher packing densities and smaller particles sizes.

Cheng[45] has proposed a modified version of Rumpf's model that describes the tensile strength of a powder compact as a system in which the particles are touching at the asperities of surface protrusions. This model expresses the strength as:

$$\sigma = \frac{3h_o S_A r \phi F_P^A}{2v(1-\phi)}, \tag{2.4}$$

where h_o is the theoretical surface separation distance at zero tensile strength, F_P^A is the inter-particle force per unit area, S_A is the average particle surface area and v is the average particle volume. A more complex model proposed by Hartley[46] argues that the separation distances for submicron particles vary due to deformation at the particle–particle contact area. Hartley's relationship for the tensile strength of a powder compact and the inter-particle force per unit area is

$$\sigma = \frac{9\phi(2r+h)(h_o-h)}{16(1-\phi)r^2} F_P^A . \tag{2.5}$$

where h_o is determined by extrapolating a plot of tensile strength as a function of packing density. Clearly, the three models show similar relationships between the strength, packing density and particle size, while the strength is directly proportional to the inter-particle force in all cases.

2.3. The Attractive Forces in Agglomerated Bodies

There are many possible cohesive mechanisms that govern the strength of a particulate body, including: van der Waals interactions, liquid bridges, solid bridges, magnetic forces and mechanical interactions (interlocking of irregularly shaped particles). Any of these forces may dominate the overall inter-particle force under particular circumstances; however, the strength of dry agglomerated ceramic particulates is generally dominated by the ever-present van der Waals forces and solid bridging phenomena[1,47,48]. The total cohesive force at the particle–particle contact under these conditions is given as:

$$F_A^T = F_A^{vdW} + F_A^B, \tag{2.6}$$

where F_A^{vdW} is the attraction due to van der Waals forces and F_A^B is the cohesive force resulting from inter-particle bridging.

Van der Waals attraction is a primary cohesive phenomenon for agglomerates consisting of sub-micron particles. This attractive force results from the interaction of atomic and molecular dipoles and has been calculated by Hamaker[49] for two macroscopic bodies. Hamaker's calculation for the attractive force between two interacting spheres is:

$$F_A^{vdW} = \frac{Ar}{6h^2}, \tag{2.7}$$

where r is the sphere radius, h is the separation distance between spheres and A is the Hamaker constant.

Bridging is another primary cohesive mechanism within an agglomerated body. Solid bridges in polymer-free ceramic systems are typically generated by the crystallization of dissolved species. Colloid processing techniques subject the ceramic material to a liquid phase, such as water, in which the particulates have some degree of solubility. The dissolved species crystallize and form bridges at the points of contact upon drying. The crystallized species may be in the form of hydrated "salts", but the exact composition, porosity and physical properties are very difficult to evaluate. The effects of crystallization on the strength of agglomerates are most reliably determined by adhesion and fracture analyses. This high degree of uncertainty, as well as the need to maintain compositional control, necessitates processing conditions that minimize crystallization.

2.4. Linear Elastic Fracture of Agglomerated Ceramic Bodies

Rumpf's model assumes that all particle contacts make similar contributions to the strength of the agglomerated body. This neglects the presence of large flaws in the body and their effects on the fracture strength. However, one can gain an understanding of the effects of flaws by using linear elastic fracture mechanics. Applying Griffith's energy balance theory[50], the criteria for failure due to crack propagation is related to the flaw size as:

$$\sigma = \left(\frac{ER}{\pi c}\right)^{\frac{1}{2}} = \frac{K_{IC}}{(\pi c)^{\frac{1}{2}}}, \tag{2.8}$$

where E is the elastic modulus, c is the flaw size, R is the fracture energy and K_{IC} is the fracture toughness.

There are several methods available for assessing the cohesive strength of powders[51], which include measuring the angle of repose, flow behavior and fracture strength. The most common are unconfined individual agglomerate fracture (diametrical compaction) and uniaxial powder compaction (die pressing). These specific techniques are narrowly focused on the strength of granules under pressing stresses, which limits the appropriateness of the data. Additionally, the scientific reliability of these methods is questionable since the loading mechanics are not predictable and the agglomerate strength is typically measured by "manually" determining the point of failure[52]. Kendall[53] has used four point bending techniques to determine the strength of agglomerated ceramic bodies. This method is more accurate since the loading mechanics are well known. The disadvantage of Kendall's technique is that high binder contents are required in order to form the bend specimen. This can lead to strength measurements that are not representative of the pure oxide body.

The following study utilizes a 4-point bending technique to determine the cohesive strength of dry binder-free agglomerated TiO_2, SiO_2, Al_2O_3 and MR2 ceramic bodies. The agglomerated ceramic bend bars are formed using the S-3DP process in which the samples are directly fabricated without the use of organic binders. The strength of the agglomerates is correlated to microstructural observations using existing fracture models, which provide information with respect to the inter-particle cohesive forces. Notched bend bars are also evaluated in order to determine the fracture toughness of the agglomerated structures by applying Griffith's theory of brittle fracture. The resulting linear elastic properties are compared and contrasted with known and theoretical values.

2.5. Procedures and Methods

2.5.1. Materials

The fracture properties were determined for four ceramic materials: SiO_2 (99.5 wt.%, Quartz, Alfa Aesar), TiO_2 (99.5 wt.%, Rutile, Alfa Aesar), Al_2O_3 (99.7 wt.%, Ceralox) and MR2 ($(1-x)BaNd_2Ti_5O_{14} : xBi_2O_3$, TDK, Japan). The average particle size and the specific surface area were measured using light scattering and single point BET, respectively. The physical properties of the powders are provided in Table 2- 1.

2.5.2. Slurry Formulation

Various slurry formulations were used for sample formation. The slurry chemistries are given in Table 2- 2. All slurries were prepared in polyethylene bottles with ~1/4" zirconia milling media. Materials were added to the slurry in the following sequence:

1. Solvent
2. Adjust pH
3. Dispersant
4. Powder

Stock solutions of 1.0 M HNO_3, 1.0 M KOH and 1.0 M NH_4OH were used to adjust the pH. The dispersant (ammonium polyacrylate, MW = 2400, Aron A-30 SL, Toagosei, Japan) was mixed thoroughly with the solvent followed by the addition of milling media (~1/3 of the volume of the mixing bottle). One half of the powder was introduced into the solvent and the mixture was ball-milled for approximately thirty minutes. The remainder of the powder was added in quarters and the slurry was milled for ~16 hours.

2.5.3. Sample Preparation

Powder beds were generated using the S-3DP[40] process, which provided a means of fabricating very reproducible agglomerated bodies with uniform density and composition. The slurry was delivered through a 127 μm nozzle (Gaiser Tool Company, Ventura, CA) from a pressurized re-circulating system[54] (Figure 2- 2). The system pressure was adjusted in order to maintain a constant slurry flow rate. The nozzle was

Table 2- 1: Properties of S-3DP Processed Ceramic Powders.

Material	Density (g/cc)	APS [STDEV] (μm)	SSA (m^2/g)	Modulus (GPa)	A – Air (J)[55]
SiO_2	2.49	0.74 [0.80]	5.1	75[33]	$6.5*10^{-20}$
TiO_2	4.26	0.52 [0.36]	3.3	280[53]	$43*10^{-20}$
Al_2O_3	3.96	0.48 [0.22]	3.9	400[33]	$14*10^{-20}$
MR2	5.9	1.26 [0.67]	1.1	116[56]	-

Table 2- 2: S-3DP Slurry Chemistries.

Ceramic	Solids (vol.%)	Solvent	pH	Dispersant
SiO_2	30.0	Water/MeOH = 1	9.5	-
TiO_2	27.5	Water	9.5	-
Al_2O_3	30.0	Water/MeOH = 1	4.0	-
MR2	27.5	Water/MeOH = 1	9.5	0.4 wt.% Aron

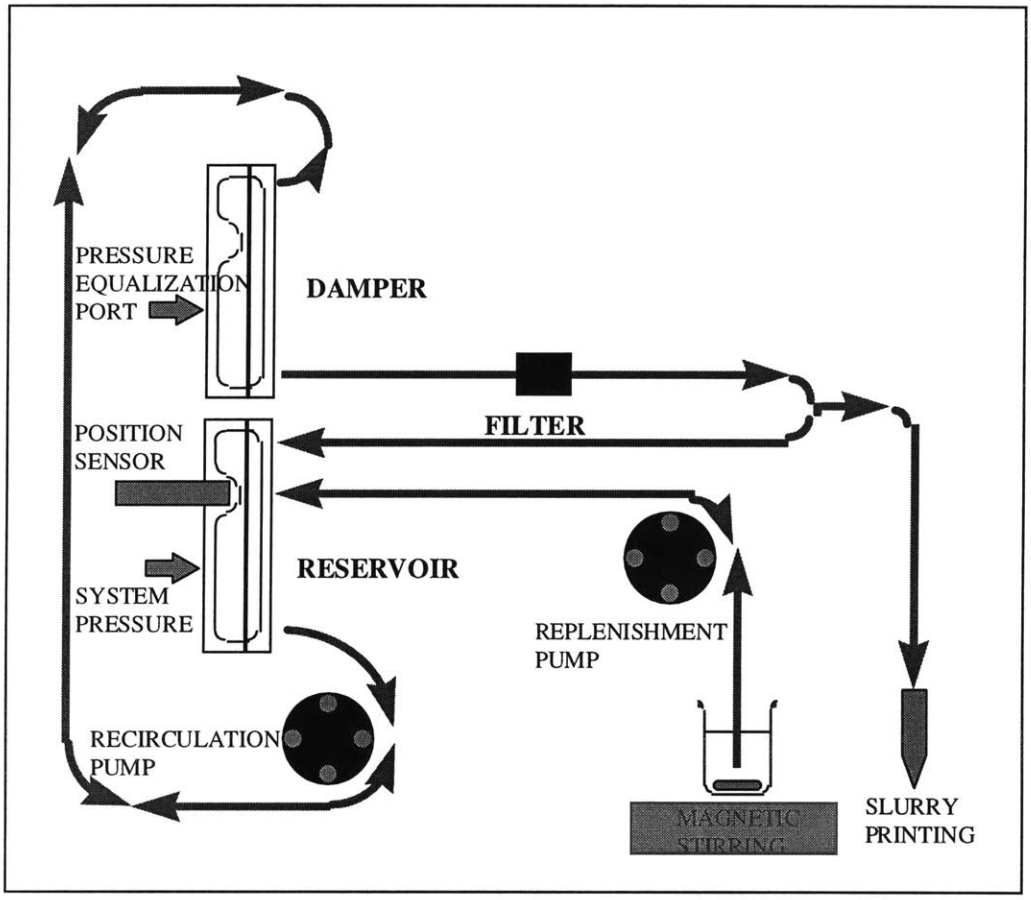

Figure 2- 2: Slurry Recirculating System.

raster-scanned over a porous substrate (borosilicate filter, Ace Glass, Vineland, NJ) such that single lines of slurry stitch together to form a powder bed layer, as illustrated in Figure 2- 3a and Figure 2- 3b. Once a single layer was complete, the piston lowered the powder bed a predetermined distance, i.e., the layer height, and the "wet" slip-cast layer was dried for 30 seconds using an IR heat lamp. Sequential layers were deposited to reach a desired powder bed height (Figure 2- 3c).

All powder beds consisted of fifty-five layers, each having a thickness of ~55 μm. Powder beds were cut to length using a 3" x 0.006" wafering blade (Buehler, Lake Bluff, IL). Samples were notched using a using a 2" x 0.002" carbide saw (Robb Jack, Lincoln, CA). The samples were dried at 110 °C for 1 hour and stored in a desiccator. MR2 powder beds were fabricated using an ammonium polyacrylate dispersant. One half of the sectioned samples were retained for analysis while the remaining samples were heated to 500 °C in air to remove the dispersant prior to fracture testing.

2.5.4. Microstructural Evaluation

The bulk density and pore size distribution of green components were determined via mercury porosimetry (Autopore 9220, Micromeritics, Norcross, GA). Polished cross-sections of epoxy infiltrated powder beds were examined using SEM (S-530, Hitachi, Tokyo, Japan).

2.5.5. Strength Measurements

ASTM Standard C 1161-94[57] was used in order to determine the flexural strength for 8 – 10 samples of each ceramic. Sample dimensions were l = 25 mm, w = 4 mm and h = 3 mm. The tests were performed using a 4-point bend configuration (Instron 4204, Canton, MA) with a 10 N load cell. The specifications of the sample fixture are given in Figure 2- 4. The fracture toughness was measured according to ASTM Standard C 1421-99[58] using bend specimen having the previously outlined dimensions. Pre-crack notches were placed across the 4 mm face of the powder bed samples. The notched faces were placed in tension during the measurement. Notch widths were 40 to 50 μm wide and lengths, c_n, were in the range of $0.12 \leq c_n/w \leq 0.30$.

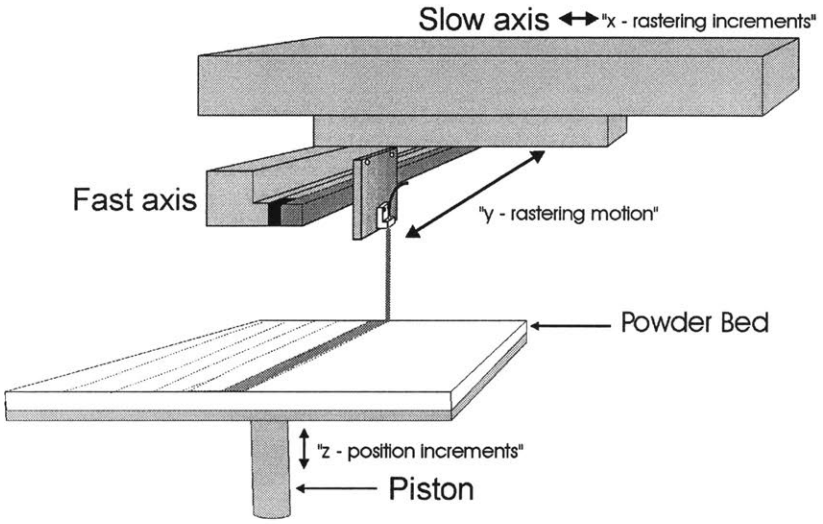

a) S-3DP Rastering Schematic

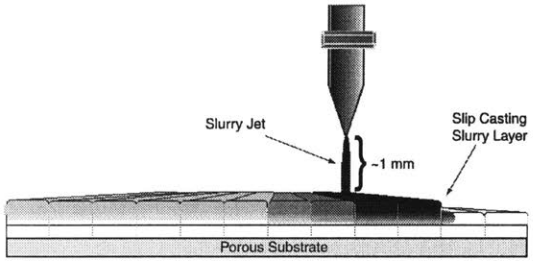

b) Deposition of Initial Layers

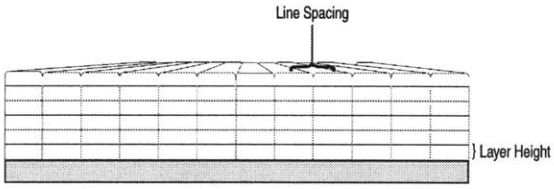

c) Completed Powder Bed

Figure 2- 3: Powder Bed Deposition Process.

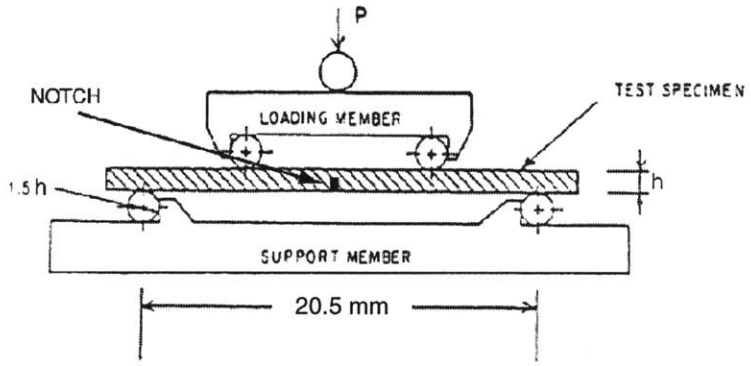

Figure 2- 4: 4-Point Loading Fixture.[57]

2.6. Results

2.6.1. Microstructural Characteristics of SiO_2, TiO_2, Al_2O_3 and MR2

The average pore sizes for the SiO_2, TiO_2, Al_2O_3 and MR2 systems are 0.6, 0.4, 0.3 and 1.0, respectively. The corresponding size distributions (Figure 2- 5a, Figure 2- 6a, Figure 2- 7a and Figure 2- 8a) indicate that the majority of pores are within the 0.1 μm to 1.0 μm range for all systems. The SiO_2 and TiO_2 samples contained bi-modal pore distributions with peaks centered around 0.1 μm - 0.5 μm and 0.1 μm - 0.3 μm, respectively. The alumina and MR2 systems represented more uniform pore distributions. Average pore sizes are shown to decrease with decreasing particle size (Table 2- 1). The MR2 system has a largest average pore size (1.0 μm) while Al_2O_3 contained the smallest (0.3 μm). The Al_2O_3 system packed most efficiently with a bulk density of 2.12 g/cc (53%). The packing density of the SiO_2 powder beds was 52% while the titania and MR2 systems had similar particle volume fractions (0.48 and 0.49).

SEM micrographs representing the polished cross-sections of the porous bodies were used to determine the presence of large flaws that may not have been detected during Hg intrusion porosimetry. The microstructure of the silica body is shown in Figure 2- 5b. Pores are uniformly distributed throughout the body and no large flaws are present. The cross section indicates that larger pores, ~ 5 μm, exist within the agglomerate. The titania and alumina cross-sections have very uniform microstructures (Figure 2- 6b and Figure 2- 7b) with no large defects. MR2 samples contain pores as large as ~ 5 μm, which are also uniformly distributed.

2.6.2. Mechanical Properties of SiO_2, TiO_2, Al_2O_3 and MR2 Agglomerates

Stress-strain curves representative of the mechanical behavior for SiO_2, TiO_2 and Al_2O_3 systems are shown in Figure 2- 9. The corresponding properties are presented in Table 2- 3. Alumina powder beds proved to have the highest fracture stress and modulus with values of 0.340 MPa and 186 MPa, respectively. Silica agglomerates demonstrated

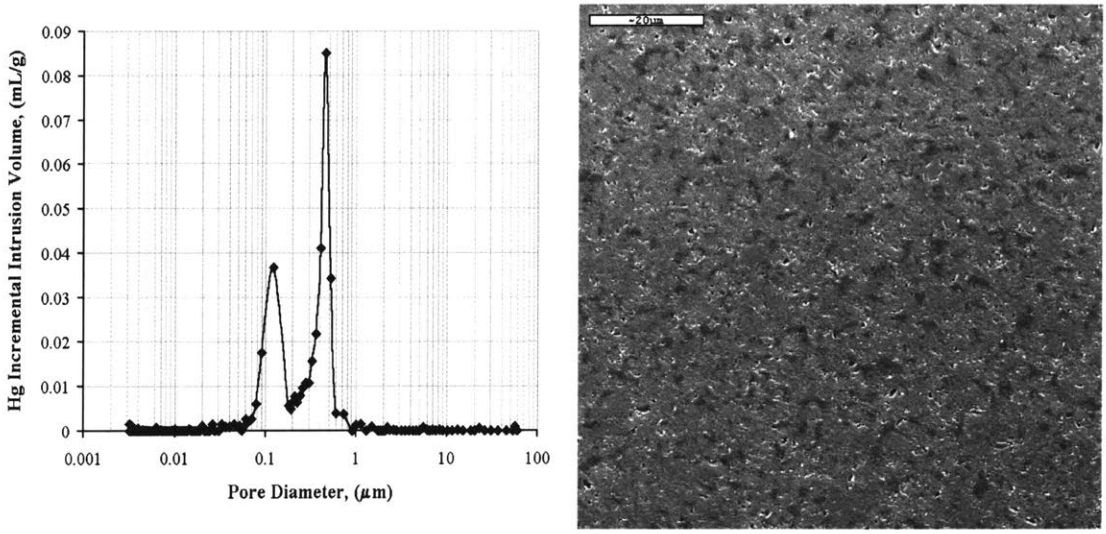

a) b)

Figure 2- 5: SiO_2 S-3DP Powder Bed a) Pore Size Distribution and b) Cross-Section of Microstructure.

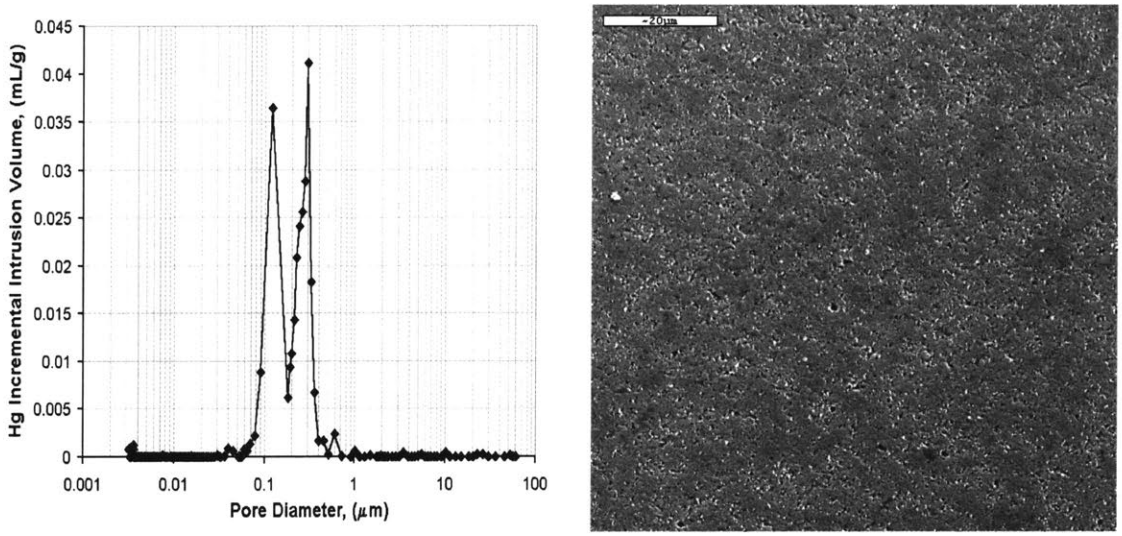

a) b)

Figure 2- 6: TiO_2 S-3DP Powder Bed a) Pore Size Distribution and b) Cross-Section of Microstructure.

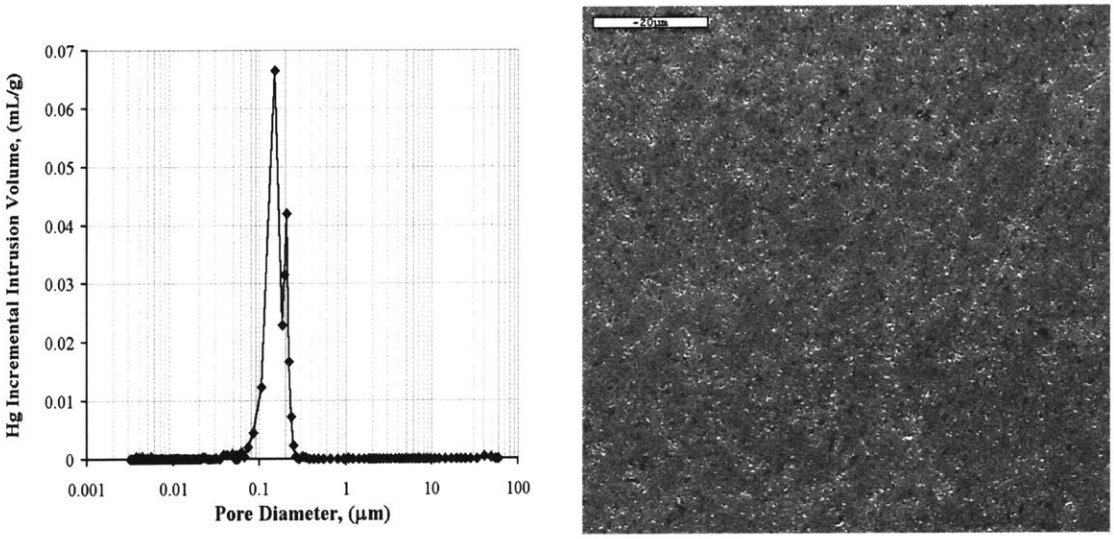

a) b)

Figure 2- 7: Al_2O_3 S-3DP Powder Bed a) Pore Size Distribution and b) Cross-Section of Microstructure.

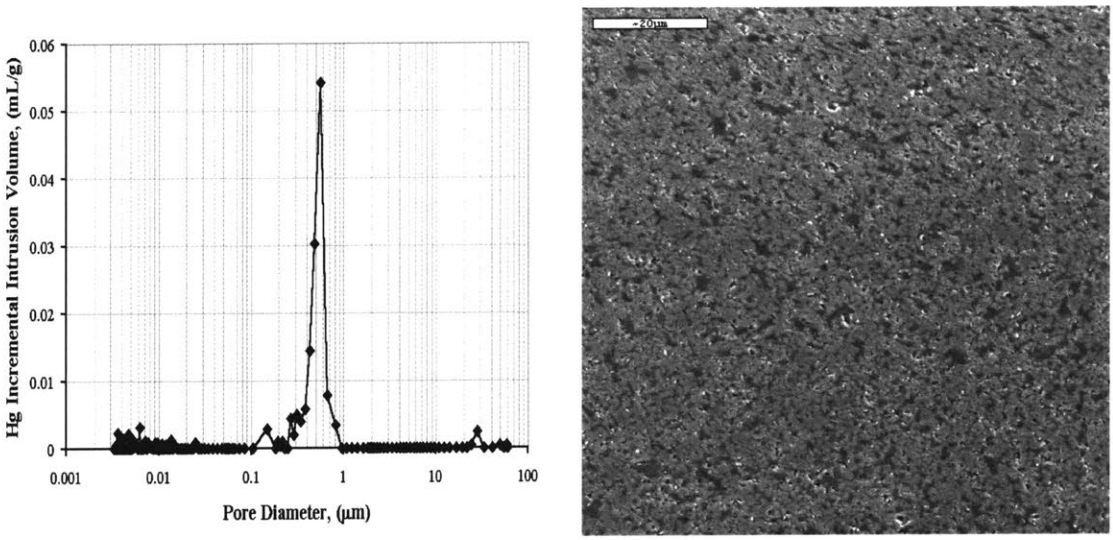

b)

Figure 2- 8: MR2 S-3DP Powder Bed a) Pore Size Distribution and b) Cross-Section of Microstructure.

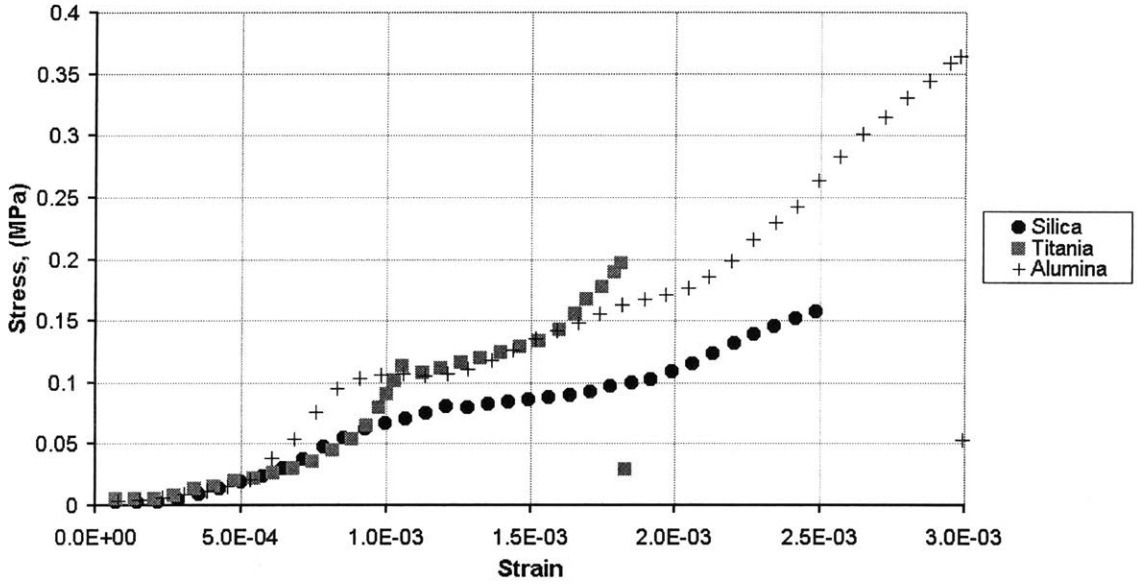

Figure 2- 9: Stress – Strain Behavior for Silica, Titania and Alumina.

Table 2- 3: Fracture Properties for Silica, Titania and Alumina.

Ceramic	Stress (MPa)	Modulus (MPa)	K_{IC} (MPa*m$^{1/2}$)	Fracture Energy R, (J/m^2)
SiO_2	0.157 ± 0.017	81.6 ± 13.8	$2.8*10^{-3} \pm 0.3*10^{-3}$	$9.8*10^{-2} \pm 2.0*10^{-2}$
TiO_2	0.177 ± 0.012	177 ± 20.0	$3.5*10^{-3} \pm 0.9*10^{-3}$	$7.2*10^{-2} \pm 3.6*10^{-2}$
Al_2O_3	0.340 ± 0.022	186 ± 29.6	$7.2*10^{-3} \pm 1.1*10^{-3}$	$2.8*10^{-1} \pm 8.8*10^{-2}$

the lowest strength with an average fracture stress of 0.157 MPa and a modulus of 82 MPa at rupture. All samples are shown to deviate from ideal elastic behavior. Deviations in the elastic moduli during loading are observed for all samples.

Representative stress-strain characteristics for notched specimen (c_n ~ 600 μm) are shown in Figure 2- 10. The corresponding linear elastic properties obtained from the notched fracture tests (Eq. 2.8) are summarized in Table 2- 3. Alumina compacts proved to have the highest fracture resistance ($7.2*10^{-3}$ MPa*$m^{1/2}$) while the lowest values were recorded for silica ($2.8*10^{-3}$ MPa*$m^{1/2}$).

Table 2- 4 summarizes the mechanical properties for MR2 agglomerates. The strength of MR2 agglomerates was strongly affected by the presence of the dispersant. The corresponding stress-strain profiles are shown in Figure 2- 11. MR2 containing 0.4 wt.% Aron is approximately twice as strong as MR2 compacts without the polymer. Dispersant-free MR2 samples had an average fracture stress of 0.6 MPa, which is greater than the SiO_2, TiO_2 and Al_2O_3 systems. Removing the dispersant did not cause an apparent change in the elastic modulus of the agglomerated bodies. There were also considerable reductions in the linear elastic fracture properties of the MR2 systems. The stress-strain profiles are shown for notched (c_n ~ 300 μm) MR2 specimens in Figure 2- 12. The calculated fracture toughnesses decreased from $2.18*10^{-2}$ MPa*$m^{1/2}$ to 0.89 MPa*$m^{1/2}$ due to dispersant removal, while the fracture energy was reduced by 84 %.

2.7. Discussion

2.7.1. Measured Strengths and Cohesive Mechanisms

The average cohesive strength of the silica, titania and alumina agglomerates were determined to be 0.157 MPa, 0.177 MPa and 0.340 MPa, respectively. These measured strengths are within the range of strength values reported in the literature. The strength of silica agglomerates have been previously measured to range from 1 MPa[59] down to 80 kPa[60]. Hartley has measured the tensile strength of titania to vary from 700 Pa up to 11 kPa[61] for compact densities ranging from 14% to 29%, respectively. Kendall[62] has observed strengths as high as 4.5 MPa for titania compacts composed of particles with an

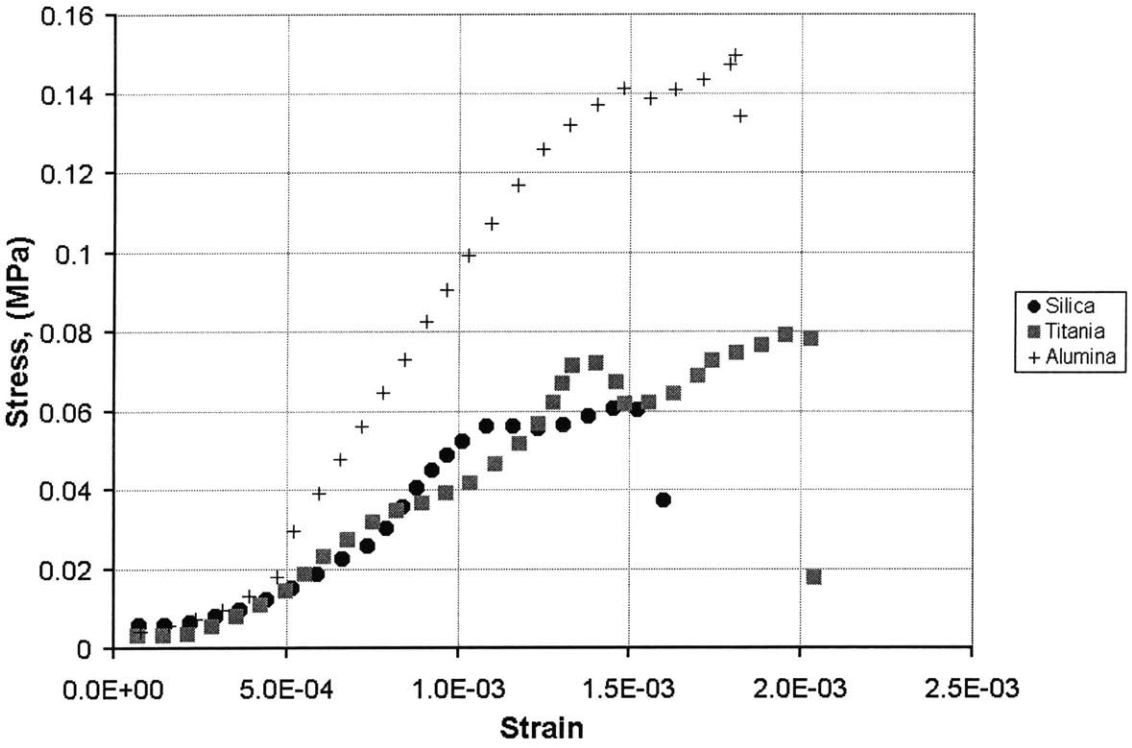

Figure 2- 10: Stress – Strain Behavior for Notched Silica, Titania and Alumina (c_n = 600 μm).

Table 2- 4: Fracture Properties of MR2 Powder Beds.

Property	MR2	MR2 + 0.4 wt.% Dispersant
Fracture Stress (MPa)	0.611 ± 0.054	1.44 ± 0.054
Modulus (MPa)	334 ± 15.8	311 ± 32.3
K_{IC} (MPa*$m^{1/2}$)	$8.91*10^{-3} \pm 1.6*10^{-3}$	$2.18*10^{-2} \pm 2.2*10^{-3}$
Fracture Energy, R (J/m^2)	0.243 ± 0.090	1.54 ± 0.32

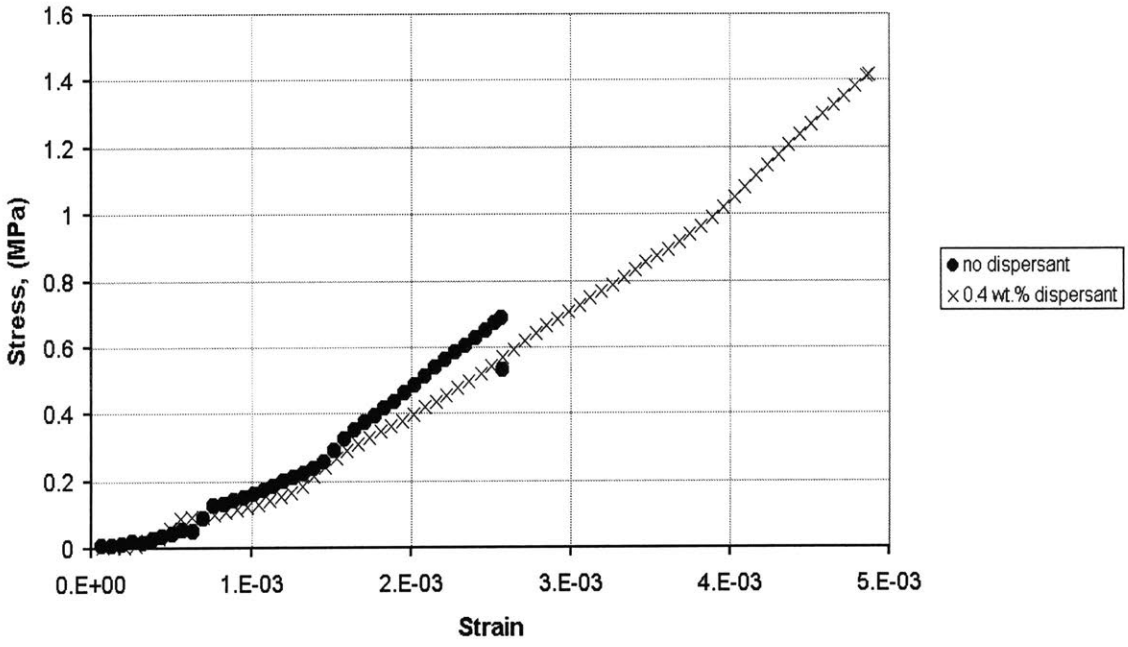

Figure 2- 11: The Effect of NH_4-Polyacrylate on the Strength of MR2.

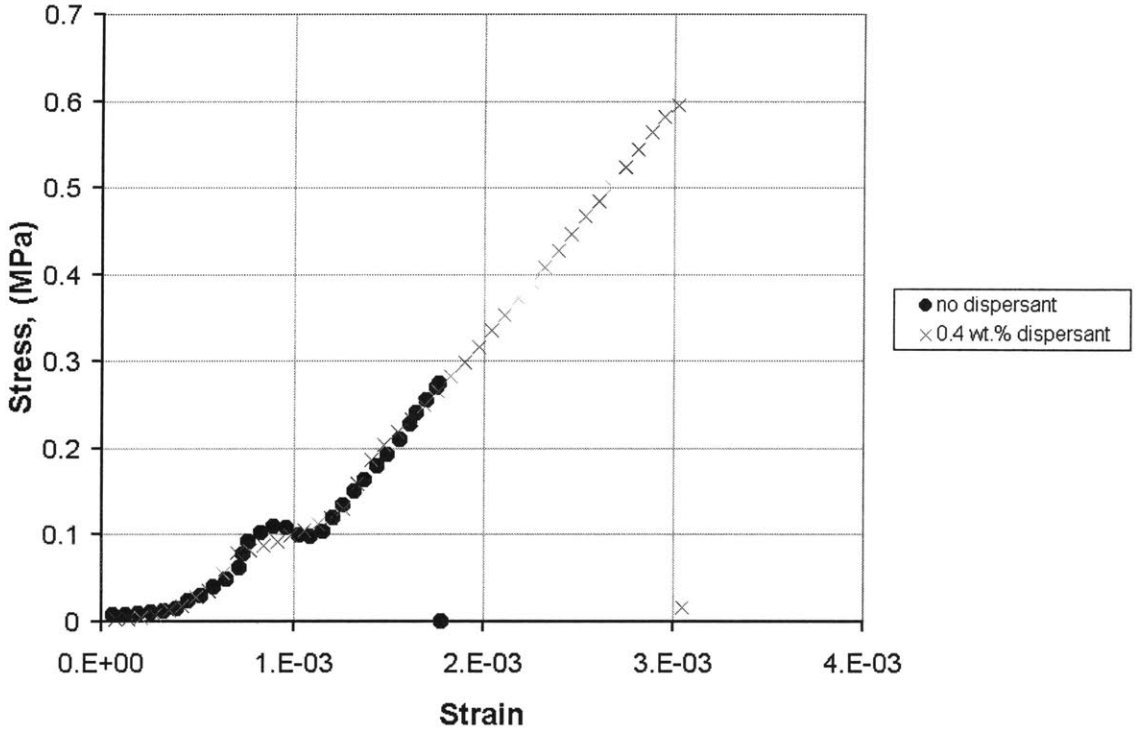

Figure 2- 12: The Effect of NH_4-Polyacrylate on the Strength of Notched MR2 Agglomerates, (c_n = 300 μm).

average size of 230 nm. Cohesive strengths of alumina agglomerates have been reported to range from 5400 Pa[63] to 1.1 MPa[52].

The theoretical cohesive strength of an agglomerate due solely to van der Waals force is calculated by combining Eq. 2.3 and Eq. 2.7:

$$\sigma = \frac{9\phi_P A}{256(1-\phi_P)\pi r h^2}, \tag{2.9}$$

and using known Hamaker constants (Table 2- 1[55]). Figure 2- 13 shows the theoretical strength as a function of particle separation distance for silica agglomerates having a packing fraction of 0.52 and an average particle size of 0.74 μm. The maximum theoretical strength is 17 kPa, which corresponds to a minimum separation distance equal to the lattice parameter of quartz. The figure shows that the measured strength exceeds the calculated strength by an order of magnitude. Similarly, the observed inter-particle force is $7*10^{-8}$ N (Eq. 2.3) and the maximum possible van der Waals force is $8*10^{-9}$ N. Therefore, van der Waals forces are not the only cohesive mechanism present within the agglomerate. Maskara and Smith[64] have observed that the strength of silica agglomerates increases by a factor of 8 as slurry pH increased from 5 to 10. The silica agglomerates in this study were fabricated using slurries that were stabilized at a pH of 9.5. Iler and Goto[65] show that the solubility of silica increases with increasing pH (Figure 2- 14). Hence, particle dissolution during processing produces dissolved silicate species that precipitate at the particle-particle interface upon drying. These precipitates act to re-enforce the strength of the silica agglomerate by forming solid bridges or silicate crosslinks.

The measured strength and the calculated strength for the titania agglomerates are shown in Figure 2- 15. The measured strength of the titania agglomerates does not exceed the maximum theoretical strength due to van der Waals interactions and intersects the calculated strength at a separation distance of $5*10^{-4}$ μm. Thus, the cohesive strength can be assumed to be primarily due to van der Waals forces with no solid bridging effects. This is logical since titania is considered to be insoluble in water over a wide pH range at room temperature[66,67].

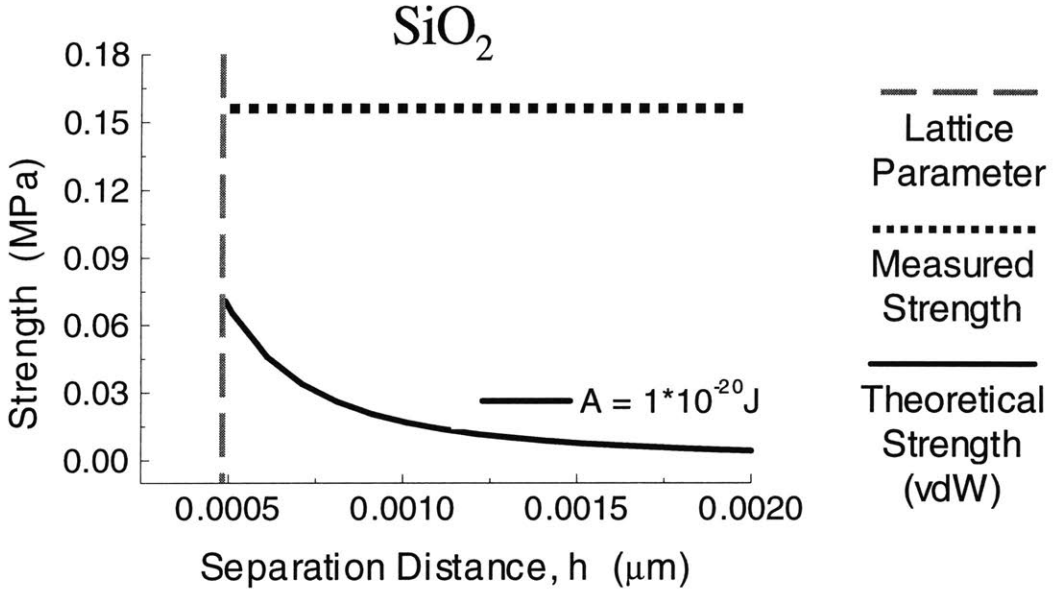

Figure 2- 13: Measured Strength of SiO_2 Compacts vs. Calculated Strength[41] due to van der Waals Forces.

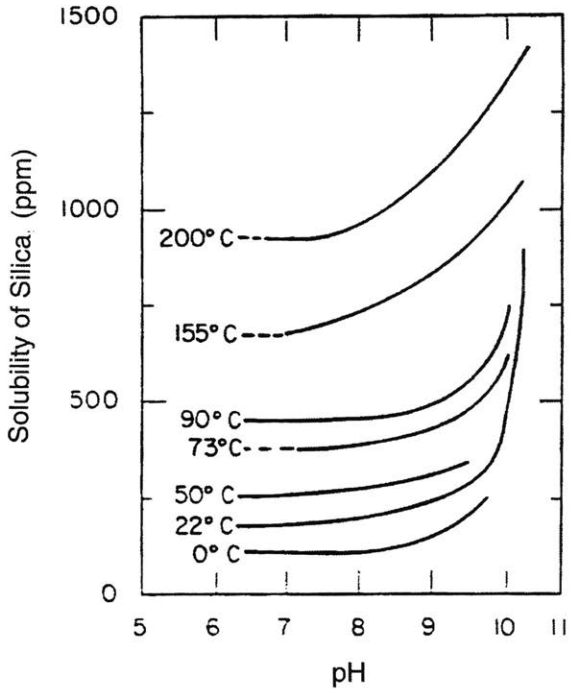

Figure 2- 14: Solubility of Silica as a Function of pH.

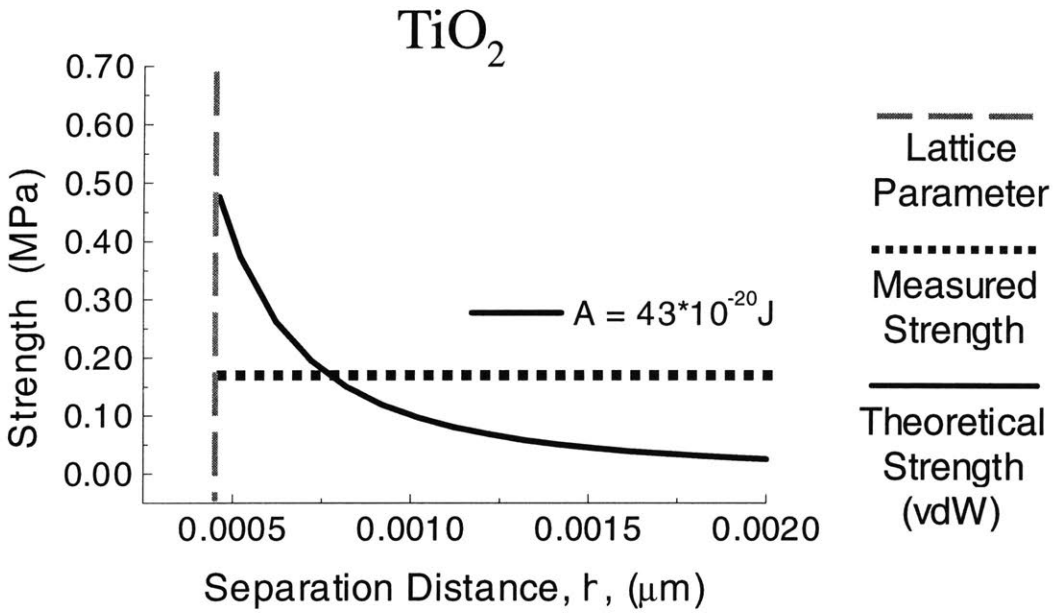

Figure 2- 15: Measured Strength of TiO_2 Compacts vs. Calculated Strength[41] due to van der Waals Forces.

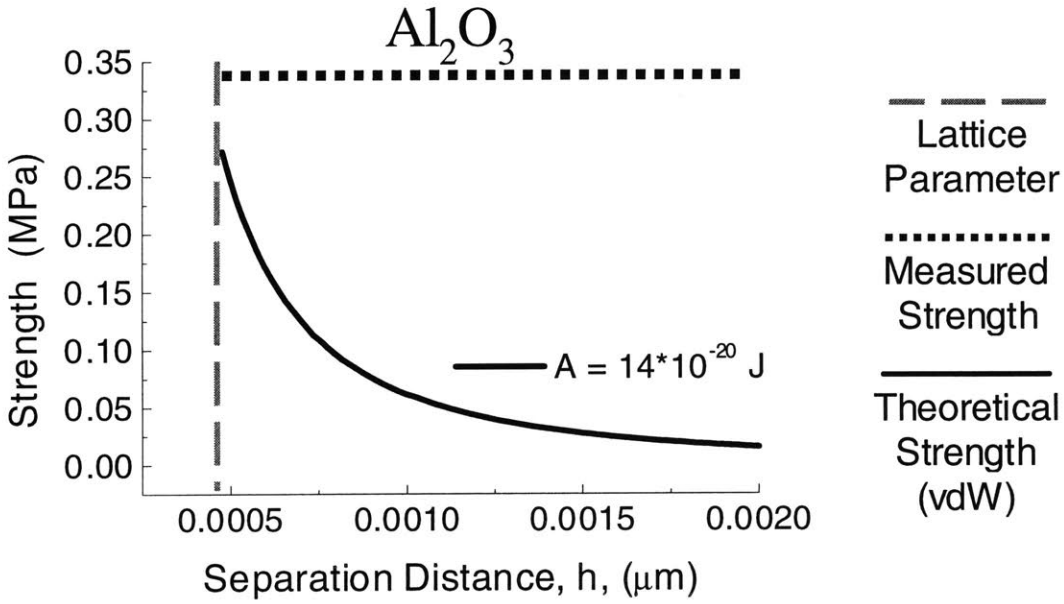

Figure 2- 16: Measured Strength of Al_2O_3 Compacts vs. Calculated Strength[41] due to van der Waals Forces.

The calculated strength for alumina agglomerates is given as a function of separation distance in Figure 2- 16. The measured strength is shown to be 5 times greater than the theoretical maximum strength resulting from van der Waals attraction. This indicates the presence of solid bridges at the particle necks. The alumina slurries were processed at pH 4.0 in order to maximize their stability without the use of an organic dispersant. Wefers[68] has shown that the solubility of aluminum hydroxide begins to increase dramatically at ~pH 3.5 to 4.0 (Figure 2- 17). The dissolved $Al(OH)_3$ species precipitate at the particle necks and increase the strength of the agglomerate.

The presence of a dispersant is shown to increase the strength of the MR2 powder compacts. The strength of the MR2 agglomerates with 0.4 wt.% Aron is 1.44 MPa which corresponds to an inter-particle force of $2*10^{-6}$ N. The strength and inter-particle force decrease to 0.61 MPa and $8*10^{-7}$ N after burning out the polymeric dispersant. The enhanced strength is a result of the dispersant acting as a binder at the particle necks. Kamiya[43] has shown a similar behavior for Si_3N_4 agglomerates in which granule strength increased by a factor of 2.5 due to the presence of a maleic anhydride polymer. The inter-particle force of the dispersant-free MR2 agglomerates remained over an order of magnitude larger than the forces for the TiO_2, SiO_2 and Al_2O_3 systems. This is likely a result of bridges remaining at the particle necks. These bridges may be composed of residual carbon left behind at the particle necks. A second possible bridging phenomenon is the crystallization of dissolved species. Oxides containing barium, such as MR2, are known to be soluble in aqueous environments,[69,70] and the solubility can be appreciable if pH is not carefully monitored.

This approach to modeling the strength of agglomerates is useful in determining the cohesive mechanisms that may be present within the agglomerated ceramic body. However, Rumpf's model suffers from two major disadvantages. Eq. 2.9 assumes that every particle contact makes an equal contribution to the strength of the agglomerate. Secondly, failure is assumed to occur simultaneously across the body. These two hypotheses neglect the effect of intrinsic flaws present within the agglomerate, which generally serve as strength limiting defects.

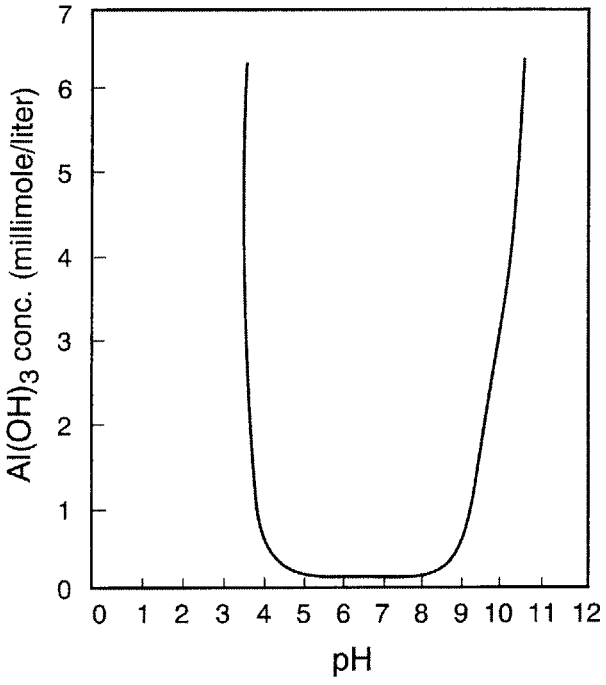

Figure 2- 17: Solubility of $Al(OH)_3$ as a Function of pH[68].

2.7.2. *Fracture Toughness and Strength Limiting Flaws*

Observations from the notched fracture experiments (ASTM 1421-99[58]) were used to calculate the fracture toughness of the four materials systems in this study:

$$K_{IC} = \sigma\sqrt{\pi c_n}\ , \tag{2.10}$$

where σ is the measured fracture strength and c_n is the length of the notch. The average values determined for the silica, titania and alumina samples were $2.8*10^{-3}$ MPa*m$^{1/2}$, $3.5*10^{-3}$ MPa*m$^{1/2}$ and $7.2*10^{-3}$ MPa*m$^{1/2}$, respectively.

The fracture toughness of the agglomerates are related to the fracture energy, R, and elastic modulus of the compact, E^C, as:

$$K_{IC} = (E^C R)^{1/2}\ . \tag{2.11}$$

Kendall et al. [62,71] have derived an expression based on Hertzian contact mechanics for the fracture energy of agglomerates consisting of elastic spheres as:

$$R = 56\phi^4\left(\frac{\Gamma^5}{E^2 a^2}\right)^{\frac{1}{3}}, \tag{2.12}$$

where Γ is the interfacial surface energy at the particle contact, E is the elastic modulus of the particle and a is the particle size. Kendall experimentally determined Γ experimentally to be 14 J*m^{-2} and 21 J*m^{-2} for the titania and alumina systems, respectively. The calculated K_{IC} values (Eqs. 2.11 and 2.12) for titania and alumina based on Kendall's interfacial fracture energy and the measured elastic moduli given in Table 2- 3 are $3.9*10^{-3}$ MPa*m$^{1/2}$ and $6.3*10^{-3}$ MPa*m$^{1/2}$. These values are within the standard deviations for the observed toughness values in this report. Moreover, Chiu[72] has studied the fracture behavior of thin granular films and reported the fracture toughnesses of alumina and silica films to be $1*10^{-2}$ MPa*m$^{1/2}$ and $7*10^{-3}$ MPa*m$^{1/2}$. The packing fractions of the alumina and silica films used in Chiu's studies were 0.62 and 0.60, respectively. These values are higher than the packing fractions for the alumina and silica samples used in this study (0.53 and 0.52). Chiu's Al_2O_3 and SiO_2 toughness values are expected to be higher by $3*10^{-3}$ MPa*m$^{1/2}$ and $2*10^{-3}$ MPa*m$^{1/2}$ due to the

packing differences, according to Eqs. 2.11 and 2.12. These toughness values are very close to the measured values after correcting for density differences.

The observed particle interfacial fracture energies, Γ, for the silica, titania and alumina agglomerates are 21 J*m^{-2}, 35 J* m^{-2} and 41 J* m^{-2} based on Eq. 2.12 and the fracture energies, R, given in Table 2- 3. Ideally, the interfacial fracture energy for two identical particle should be equivalent to the respective surface energy of the particles:

$$\Gamma = 2\gamma, \tag{2.13}$$

where γ is the surface free energy of the particle. Bruce[73] has determined the surface energies of SiO_2, TiO_2 and Al_2O_3 to be 0.9 J*m^{-2} , 0.8 J*m^{-2} and 1.2 J*m^{-2}. According to Eq. 2.13, the interfacial facture energies are 1.8 J*m^{-2}, 1.6 J*m^{-2} and 2.4 J*m^{-2}. These values are more than an order of magnitude less than the measured interfacial fracture energies. This indicates that energy is being dissipated during fracture. This is reasonable since the stress-strain curves for all agglomerates show variations in the elastic moduli that represent permanent deformation phenomena.

The linear elastic fracture properties of the MR2 system are dramatically affected by the presence of a polymeric dispersant (0.4 wt.% Aron). The stress-strain behavior is characteristically brittle and, therefore, the notched four-point bending measurements represent accurate toughness values, which are given in Table 2- 4. The particle interfacial fracture energy (Eq. 2.12) for the dispersant–free MR2 agglomerates has an average value of 39 J*m^{-2}. The interfacial energy increases by 46% to 57 J*m^{-2} upon addition of 0.4 wt.% ammonium acrylate. The bond strength is increased due to the presence of the dispersant at the particle-particle interface.

The intrinsic flaw sizes, c, for the agglomerates are determined by using the average fracture toughness, K_{IC} and the observed fracture strength, σ, in Eq. 2.10. The average flaw sizes for the four systems are given in Table 2- 5. The flaw sizes are approximately two orders of magnitude larger than the respective particle and pore dimensions for all materials. The flaw size distribution for all four systems is presented in Figure 2- 18. Clearly, the flaw populations are centered around 50 μm, 100 μm and 150 μm. While no large defects were observed in the SEM micrographs (Figure 2- 5b through Figure 2- 8b), the dimensions of the flaws are characteristic of the fabrication

Table 2- 5: Calculated Intrinsic Critical Flaw Size.

Ceramic	$c^{critical}$ (μm)
SiO_2	102
TiO_2	108
Al_2O_3	139
MR2 (without dispersant)	46
MR2 (0.4 wt.% dispersant)	58

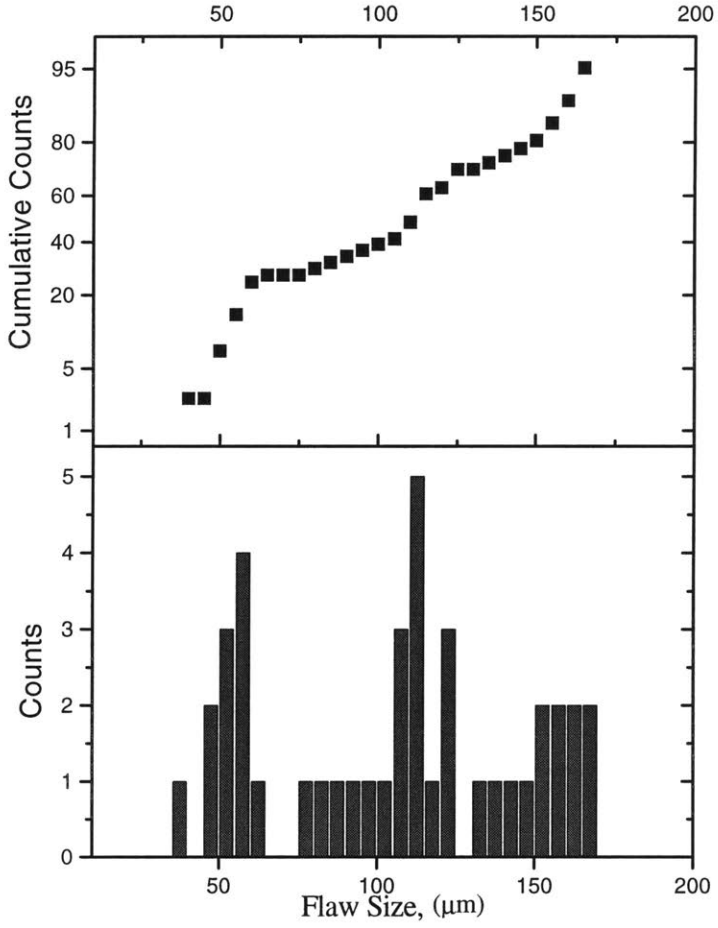

Figure 2- 18: Cumulative Distribution of Flaw Sizes for the SiO_2, TiO_2, Al_2O_3 and MR2 Systems.

process. The S-3DP technique produces bodies that are constructed of many individual slip cast layers, each having a thickness of ~ 55 μm. All of the calculated intrinsic flaw sizes are on the order of a layer thickness, or multiples thereof. The critical flaw sizes represent one of two scenarios: large pre-existing defects exist within the agglomerate, or several powder bed layers mechanical fracture prior to catastrophic failure. The former is expected for brittle agglomerates; however, the non-linear deformation mechanisms observed in the stress-strain profiles correspond to the latter. Nevertheless, the distribution proves that the strength of an agglomerated body is influenced by the processing technique and that the flaw size is not necessarily determined by the primary microstructural dimensions.

2.8. Conclusion

Agglomerates are present duringthroughout many different stages in ceramics processing. Knowledge of their strength and cohesive mechanisms is essential in order to promote either their destruction for the formation of a dispersion, or their preservation in consolidation processes. Flexural strength measurements are an effective method for determining the cohesive strength of agglomerates. The fracture model proposed by Rumpf is the basis for many agglomerate fracture theories and it is useful in order to determine the dominant inter-particle forces that control the agglomerate's cohesive strength. The cohesiveness of dry, binder-free agglomerates can be mostly attributed to van der Waals attraction and bridging due to the precipitation of dissolved species at the particle-particle necks. The fracture toughness of powdered compacts can be determined with moderate accuracy by measuring the fracture strength of notched bend bars using standard ASTM techniques. The application of Griffith's energy criterion has provided evidence that the strength of the agglomerate is controlled by flaws inherent to the formation technique.

Chapter Three

Additive Enhanced Redispersion of Ceramic Agglomerates

3.1. Introduction

Deagglomeration of ceramic powders is usually accomplished by immersion of powders in a surfactant containing liquid vehicle followed by milling. This chapter focuses on mechanisms that augment the classical milling approach by adding a chemical pressure to break up the agglomerate. This study explores the enhanced redispersion of TiO_2 ceramic compacts that contain a non-ionic water soluble polymer, polyethylene glycol (PEG). PEG forms a polymer solution within the agglomerate structure during redispersion. The resulting osmotic pressure gradient forces water into the porous structure and creates a tensile stress on the particle network with magnitudes as high as 0.6 MPa. Thus, the principle to achieving redispersion is to develop osmotic pressures that exceed the cohesive strength of the agglomerated structure. A critical PEG concentration of 2.0 vol.% PEG 400 has been determined for the titania system, below which redispersion is minimal. These redispersion principles are successfully applied to silica and alumina systems by using 7.0 vol.% PEG 400 to generate an osmotic pressure of 0.6 MPa, which exceeds their cohesive strengths of 0.15 MPa and 0.34 MPa, respectively.

The redispersion of systems containing cohesive particulate bodies is of great universal interest. Reversible separation and particulate dispersion operations are of considerable importance in colloidal science and in various industrial fields such as water treatment, sludge processing and paper making. Two primary applications exist in the ceramics industry, which focus on the redispersion of consolidated particulate bodies. Suspension concentration and the subsequent redispersion of the agglomerated cake prior to use may dramatically diminish transportation costs. Initial conditioning of the slurry such that the suspending medium could be removed would significantly decrease the shipping capacity requirements in addition to minimizing expenses. Redispersing "waste" bodies is also very appealing to manufacturers of advanced ceramics. The

redispersion of unused agglomerated ceramic bodies facilitates the reclamation of costly materials such as the tungsten carbide–cobalt or Si_3N_4 systems.

The successful fabrication of ceramics using the S-3DP[37] process also requires the redispersion of an agglomerated powder bed. The nature of the formation process produces a cohesive bed from which a binder-printed part must be removed. Tailoring the S-3DP process and chemistry to control redispersion is paramount for manufacturing ceramic components with complex geometries.

3.2. Peptization vs. Redispersion

Two attractive states are possible for a colloidal system: a secondary minimum, M_S, and a primary minimum, M_P (see Figure 3- 1). Flocculation occurs when particles fall into the secondary minimum. The reversibility of this attractive state, i.e., peptization, has been well documented over the past several decades[55,74,75]. Generally, the colloid can be redispersed by controlling the thermal energy of the particle or by altering the ionic strength of the suspending solution to increase electrostatic repulsive forces. Reversible flocculation has been utilized since the early 1900's in order to control the stability of colloidal suspensions, e.g., AgI dispersions[76]. Many other applications have evolved that include management of soil drainage properties[77] and control of the stability and efficiency of many sol-based pharmaceutical techniques.

The second attractive state is the primary minimum. The particle repulsive forces are very small compared to van der Waals forces and coagulation results. This primary minimum represents the thermodynamic equilibrium state of the system. DLVO theory defines this cohesive condition to be irreversible[74,78]; however, some exceptions exist that utilize dispersive mediums with tunable solvencies[79]. These cases are examples of the redispersion of coagula.

Existing repulsive forces are removed upon drying. Particles agglomerate and form a cohesive compact structure. Agglomerates are more resilient than the previously described systems because many attractive forces may be present, which act to reinforce the ever-present van der Waals force. The act of breaking apart these powdered compacts is referred to as the *redispersion of agglomerates.*

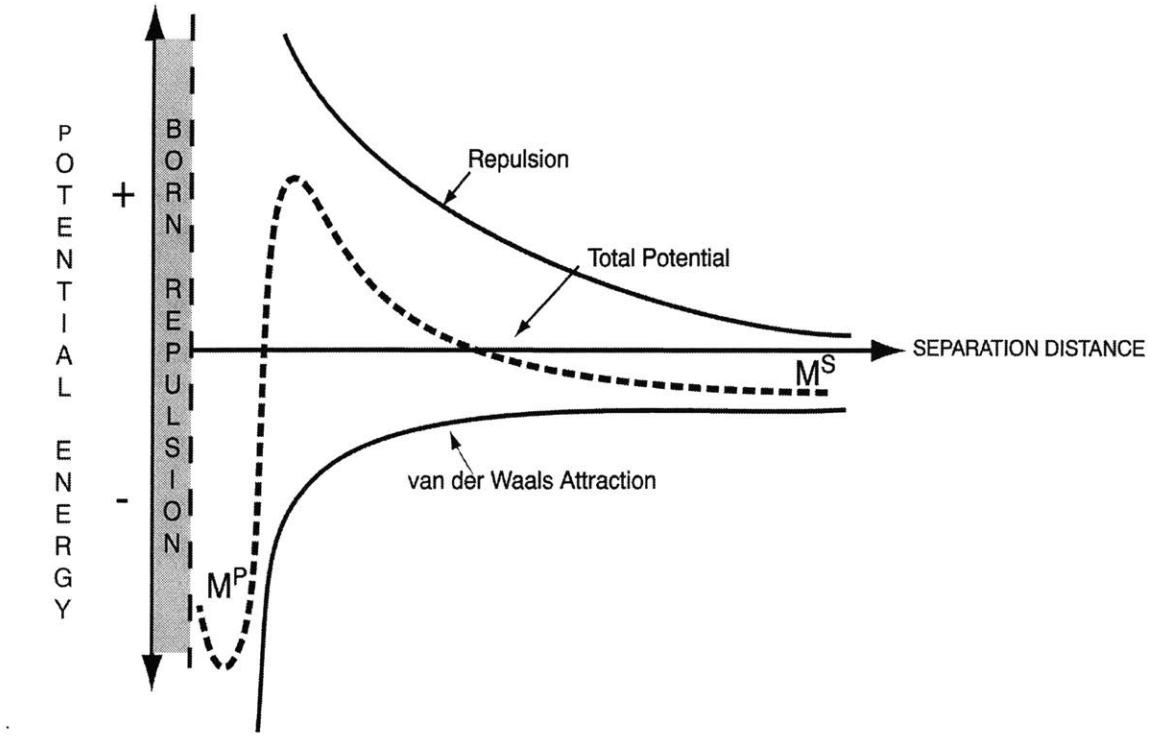

Figure 3- 1: The Total Potential Between Two Spherical Particles.

3.3. The Redispersion of Agglomerates

The process of agglomerate redispersion consists of several stages:

1. incorporation of the agglomerate into a liquid medium,
2. liquid infiltration of the particulate body and
3. dispersion of the agglomerated structure into primary particles.

These processes are ultimately controlled by the third and final stage. The efficiency of this disagglomeration stage is referred to as the redispersibility of the agglomerated structure. Agglomerate redispersibility is best described by the amount of energy required to break up the cohesive particle assembly, where lower energies represent systems that redisperse more easily.

There are two sources of energy. The most common is mechanical energy. Traditionally, attrition and sonication methods are used in order to provide sufficient mechanical energy to deagglomerate the body. A second source is chemical energy. The composition of the agglomerate may include soluble additives that supply energy upon mixing. Controlling the initial chemistries of the agglomerate and the redispersing medium facilitates the optimization of the chemical energy. Consequently, the amount of required mechanical input energy is minimized. This is extremely valuable for processing techniques in which the application of mechanical energy is not feasible, i.e., S-3DP.

The success of chemically enhanced redispersion of agglomerated bodies requires knowledge of two factors: the strength of the agglomerate and the counteracting, chemically–enhanced redispersive forces.

3.3.1. The Strength of Green Ceramic Bodies

There are several methods available for assessing the cohesive strength of powders[51], which include measuring the angle of repose, flow behavior, and fracture strength. Models have been developed that relate tensile strength to various properties of the consolidated component. Cheng[45] has developed a complex model that focuses on the influence of particulate separation distances on the tensile strength. More recently, Hartley et al.[46] have developed a model which correlates the strength of compacts to van

der Waals forces. Many additional models[80] have been developed, all of which are based on the initial theory proposed by Rumpf[41]. Rumpf was one of the first to derive an expression for the mean theoretical strength of an agglomerate as a function of particle size, packing density and inter-particle force. Rumpf's mathematical model for the strength of a randomly packed agglomerate is:

$$\sigma = \frac{27\phi}{32(1-\phi)\pi r^2} F_A, \tag{3.1}$$

where ϕ is the particle volume fraction, r is the average particle radius and F_A is the inter-particle attractive force. Many cohesive mechanisms exist that can influence the inter-particle forces in powdered materials. It is well known that the strength of agglomerated ceramic particulates is generally dominated by van der Waals and bridging phenomena[47]. The total cohesive force at the particle-particle contact under these conditions is:

$$F_A^T = F_A^{vdW} + F_A^B, \tag{3.2}$$

where F_A^{vdW} is the attraction due to van der Waals forces and F_A^B is the cohesive force resulting from inter-particle bridging.

Many researchers have analyzed the strength of ceramic agglomerates[1,72]. Studies have shown that the strengths of binder-free ceramic systems are generally less than 1 MPa[43,81]. Chapter Three has described the mechanical properties for a wide range of ceramic agglomerates, including titania, silica and alumina, that have been determined using standard four-point bending techniques. Agglomerated ceramic bend bars were formed using the S-3DP process in which uniform samples were directly fabricated without the use of organic binders. The fracture strengths of the agglomerate systems were in the range of 0.1 – 0.6 MPa. Existing fracture models were employed in order to resolve the dominant inter-particle force(s) responsible for agglomerate strength. The inter-particle forces were observed to be 10^{-8} – 10^{-6} N, which suggests that van der Waals forces and solid bridges are the primary cohesive mechanism in binder-free agglomerates.

3.3.2. *Chemically Induced Redispersive Forces*

Soluble polymeric additives within the pore structure of the agglomerate dissolve upon infiltration of the redispersing medium. The phenomena governing these processes obey the thermodynamic principles of polymer solutions. Therefore, the theory of polymer solutions is essential in order to understand their effects on the redispersibility of agglomerates.

Traditionally, the theory of Flory[82] and Huggins[83] has been used to describe the behavior of many polymer solutions[84,85]. The theory concentrates on the difference between the total interaction energy of the polymer and solvent components in the solution and that for the pure components. The change in free energy due to mixing is:

$$\Delta G_M = \Delta H_M - T\Delta S_M , \tag{3.3}$$

where the total change in entropy, ΔS_M, is assumed to be represented by the change configurational entropy, ΔS_M^C. Flory used a binary solution lattice containing polymer units and solvent units to derive the configuration entropy as:

$$\Delta S_M^C = -k(n_S \ln v_S + n_P \ln v_P), \tag{3.4}$$

where k is Boltzmann's constant, n_S and n_P are the number of solvent and polymer molecules and v_S and v_P are the volume fractions of the solvent and polymer, respectively. The intermolecular interactions are represented by the van Laar expression for the heat of mixing of a two component system, which is:

$$\Delta H_M = kT\chi n_S v_P , \tag{3.5}$$

where χ is the polymer-solvent interaction parameter (dimensionless) and χkT represents the energy required to replace one polymer molecule with one solvent molecule. Combining Eqs. 3.4 and 3.5 into Eq. 3.3 yields:

$$\Delta G_M = kT\left(n_S \ln v_S + n_P \ln v_P + \chi n_S v_P\right), \tag{3.6}$$

Differentiation of this expression with respect to n_S gives the change in chemical potential of the solvent in the polymer solution, μ_S, relative to its chemical potential in the pure solution, μ_S^o as:

$$\Delta\mu = \mu_S - \mu_S^o = RT\left[\ln(1-v_P)+\left(1-\frac{1}{x}\right)v_P + \chi_1 v_P^2\right] = RT\ln a_S, \qquad (3.7)$$

where x is the number of segments in the polymer chain and a_S is the activity of the solvent in the solution. Thermodynamic relations also state $\Delta\mu$ as:

$$\Delta\mu = N\frac{\delta\Delta G_M}{\delta n_1}\bigg|_{T,P,n_2} = -\pi \mathrm{v}_S. \qquad (3.8)$$

where v_S is the molar volume of the solvent and π is the *osmotic potential* of the system. Expanding Eq. 3.7 (first two terms) and equating it with Eq. 3.8 yields

$$\pi = \frac{RT}{\mathrm{v}_S}\left[\frac{v_P}{x}+\left(\frac{1}{2}-\chi\right)v_P^2\right]. \qquad (3.9)$$

This expression for the osmotic potential of a polymer solution is more conveniently expressed in terms of molecular weight and concentration of the polymer:

$$\pi = \frac{RT}{\mathrm{M_w}}C + \frac{RT\bar{v}_P^2}{\mathrm{v_S}}\left(\frac{1}{2}-\chi\right)C^2, \qquad (3.10)$$

where $\bar{v}_P$ is the partial specific volume of the polymer. It is important to emphasize that the osmotic potential is entirely chemical in nature. However, this potential is commonly referred to as the *osmotic pressure* since it is presented with units of pressure. The osmotic pressure corresponds to an applied pressure that would be required in order to raise the free energy of the solvent in the polymer solution to that of the pure solvent.

Many techniques utilizing osmotic pressure have been developed over the past decades. Osmotic techniques are used extensively to concentrate dilute protein solutions[86], while other processes[87,88] use osmotic pressure to probe the forces that exist between a wide range of surfactants and macromolecules. Osmotic pressure has also been integrated into the field of ceramics processing. Miller and Zukoski[89] have successfully formed high-density green bodies by osmotically consolidating suspensions. The green bodies were formed by placing a colloidal suspension within a semi-permeable membrane, which is then placed into a polymer solution (polyethylene glycol, (PEG)). A potential gradient is established between the slurry solvent and that of the surrounding

solution. This driving force causes the solvent to be extracted from the suspension yielding a consolidated particulate body.

The following sections explore the enhanced redispersion of dense ceramic compacts that contain a water soluble polymer. This study is especially interesting since the redispersion process represents the antithesis of traditional ceramic powder processing procedures. More specifically, the redispersion of S-3DP powder beds[40] containing PEG is studied as a function of polymer concentration and molecular weight. PEG is an excellent candidate because it is inexpensive, it is readily available in a wide range of molecular weights and it produces very high osmotic pressures (~8 MPa)[90]. The induced osmotic stresses are compared to the cohesive strength of the agglomerated structure[91]. The ceramic system used to model these phenomena is titania. Titania has been studied for many years and its behavior in aqueous systems is well-known[92]. A simple oxide system such as titania allows one to select processing conditions that reduce the solubility of the ceramic and its respective hydroxide(s)[67]. The presence of solid necks within the powder assembly is therefore minimized, which helps to control, as well as understand, the strength of the agglomerate. Additionally, titania is representative of many industrial titanate systems[70] such as barium titanate, lead zirconate titanate and MR2 due to similarities in their respective surface potential characteristics, i.e., zero point of charge. The redispersion principles that are outlined by the titania system are also applied to the silica, alumina and MR2 ceramic systems.

3.4. Procedures and Methods

3.4.1. Ceramic Materials and Slurry Formulation

TiO_2 (99.5 wt.%, Alfa Aesar), SiO_2 (99.5 wt.%, Alfa Aesar), Al_2O_3 (99.7 wt.%, Ceralox) and MR2 ceramic powders were used to form slurries for the S-3DP process[37]. The average particle size and specific surface were measured using light scattering and single BET techniques. The physical properties of the powders are provided in Table 3- 1.

Table 3- 1: Powder Characteristics.

Material	Density (g/cc)	APS (μm)	SSA (m^2/g)
TiO_2	4.26	0.52	3.31
SiO_2	2.49	0.74	5.13
Al_2O_3	3.96	0.48	3.98
MR2	5.9	1.26	1.11

Table 3- 2: S-3DP Slurry Chemistries.

Ceramic	Solids (vol.%)	Solvent	pH	Dispersant	Other
SiO_2	30.0	Water/MeOH = 1	9.0	-	-
	30.0	Water/MeOH = 1	9.0	-	PEG 400
TiO_2	27.5	Water	9.5	-	-
	27.5	Water	9.5	-	PEG 300
	27.5	Water	9.5	-	PEG 400
	27.5	Water	9.5	-	PEG 1000
	27.5	Water	9.5	-	PEG 4000
	27.5	Water	9.5	-	PEG 6000
Al_2O_3	30.0	Water/MeOH = 1	4.0	-	-
	30.0	Water/MeOH = 1	4.0	-	PEG 400
MR2	35	Water/MeOH = 1	9.5	0.4 wt.% Aron	-
MR2	35	Water/MeOH = 1	9.5	0.4 wt.% Aron	PEG 400
MR2	35	Water/MeOH = 1	9.5	0.4 wt.% Aron	PEG 1000

Various slurry formulations were used for sample formation. The slurry chemistries are given in Table 3- 2. All slurries were prepared in polyethylene bottles with ~1/4" zirconia milling media. Materials were added to the slurry in the following sequence: solvent, adjust pH, add dispersant, and add powder. Stock solutions of 1.0 M HNO_3, 1.0 M KOH and 1.0 M NH_4OH were used to adjust the pH in order to optimize the dispersion and chemical stabilities of the slurries[67,69,70]. The dispersant (ammonium polyacrylate, MW = 2400, Aron A-30 SL, Toagosei, Japan) was mixed thoroughly with the solvent followed by the addition of polyethylene glycol (PEG 300, PEG 400, PEG 1000 and PEG 4000 Union Carbide, Danbury, CT; PEG 6000, Fluka, New York, NY). Milling media (~1/3 of the volume) were added to the mixture. One half of the powder was introduced into the solvent and the mixture was ball-milled for approximately 30 minutes. The remainder of the powder was added in quarters and the slurry was milled for ~16 hours.

3.4.2. Sample Preparation

Samples were generated using the S-3DP process[40]. The slurry was delivered through a 127 μm nozzle (Gaiser Tool Company, Ventura, CA) from a pressurized recirculating system[54]. The system pressure was adjusted in order to maintain a constant slurry flow rate. The nozzle was raster-scanned over a porous substrate (boro-silicate filter, Ace Glass, Vineland, NJ) such that single lines of slurry stitch together to form a powder bed layer, as illustrated in Figures Figure 3- 2b and Figure 3- 2c. Once a single layer was complete, the piston lowered the powder bed a predetermined distance, i.e. layer height, and the "wet" slip-cast layer was dried for 30 seconds using an IR heat lamp. Sequential layers were deposited to reach a desired powder bed height (Figure 3- 2d). These multi-layered powder beds were constructed of 37 to 54 layers. TiO_2, SiO_2 and Al_2O_3 powder bed layer heights were 55 μm while the MR2 powder beds were built with 80 μm layers. The geometry of the TiO_2, SiO_2 and Al_2O_3 redispersion samples was 14 mm x 4 mm x 3mm, while the volumes of MR2 samples were in the range of 0.3 to 0.5 cm^3. Powder bed properties are given in Table 3- 3.

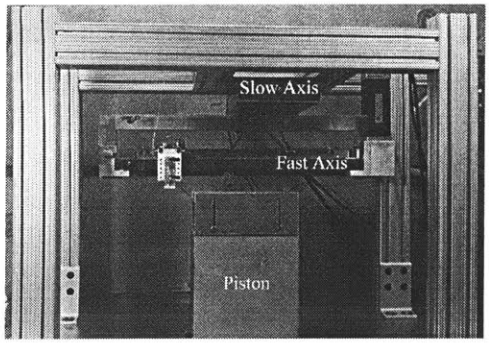

a) S-3DP Machine

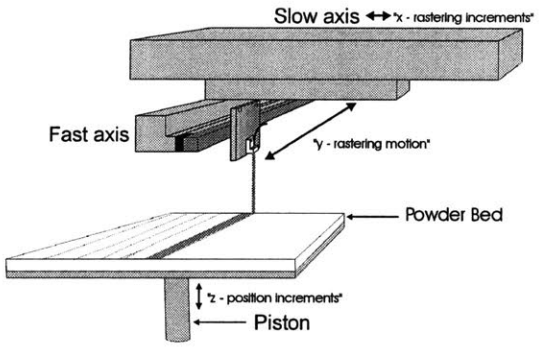

b) S-3DP Rastering Schematic

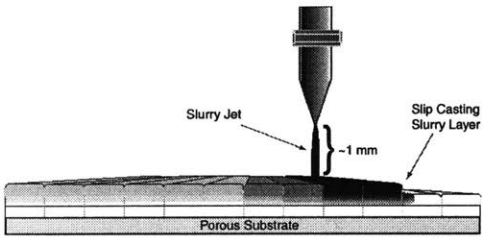

c) Deposition of Initial Layers

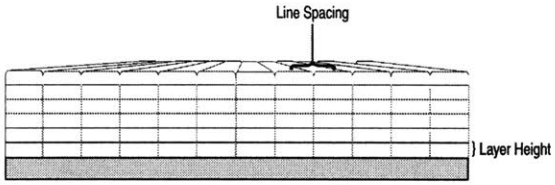

d) Completed Powder Bed

Figure 3- 2: Powder Bed Deposition Process.

Table 3- 3: Powder Bed Average Pore size and Packing Fraction.

Powder Bed	Average Pore Size (μm)	Packing Density
TiO_2	0.4	0.48
SiO_2	0.6	0.52
Al_2O_3	0.3	0.53
MR2	1.0	0.49

3.4.3. *Calculating the Powder Bed PEG Concentration*

Powder beds were formed containing various concentrations of PEG. The concentrations of PEG were formulated based on the ceramic powder's mass. The following calculations were used to determine the volume fraction of PEG with respect to the powder and the powder bed pore space.

$$C_{PEG}^{Ceramic}(vol.^{POWDER}\%) = 100\left[\frac{\rho_{ceramic}x_{PEG}}{(1-x_{PEG})\rho_{PEG}}\right], \tag{3.11}$$

$$C_{PEG}^{Pore}(vol.^{PORE}\%) = 100\left[\frac{\phi}{1-\phi}\left(\frac{\rho_{ceramic}x_{PEG}}{\rho_{PEG}}\right)\right], \tag{3.12}$$

where $\rho_{ceramic}$ and ρ_{PEG} are the densities of the ceramic powder and polyethylene glycol, respectively and x_{PEG} is the solids mass fraction of PEG. The mass concentrations were in the range 0.0 wt.% to 3.0 wt.%. The following discussions refer to PEG concentrations within the pore space for convenience.

3.4.4. *Redispersion Measurements*

The reduction of powder bed mass due to redispersion was measured for all of the ceramic systems. Samples were slowly saturated with redispersing solution prior to being placed in the redispersion bath in order to avoid excess pressure within the powder bed due to rapid infiltration[30,93]. The saturated powder bed was quickly placed into a wire-mesh holder that was suspended in the redispersing medium. The mass loss due to redispersion, i.e. redispersed mass, was electronically recorded over a period of 15 minutes using a computer-interfaced balance. The redispersion instrumentation and setup are shown in Figure 3- 3.

3.4.5. *Dissolution Rate of PEG*

PEG 1000 was pressed into a disk having a mass, volume and surface area of 0.787 g, 0.697 cm^3 and 6.0 cm^2, respectively. The dissolution rate of PEG 1000 was measured by monitoring the dissolved mass loss over time (60 sec). The normalized dissolution rate (cm/sec) was calculated as:

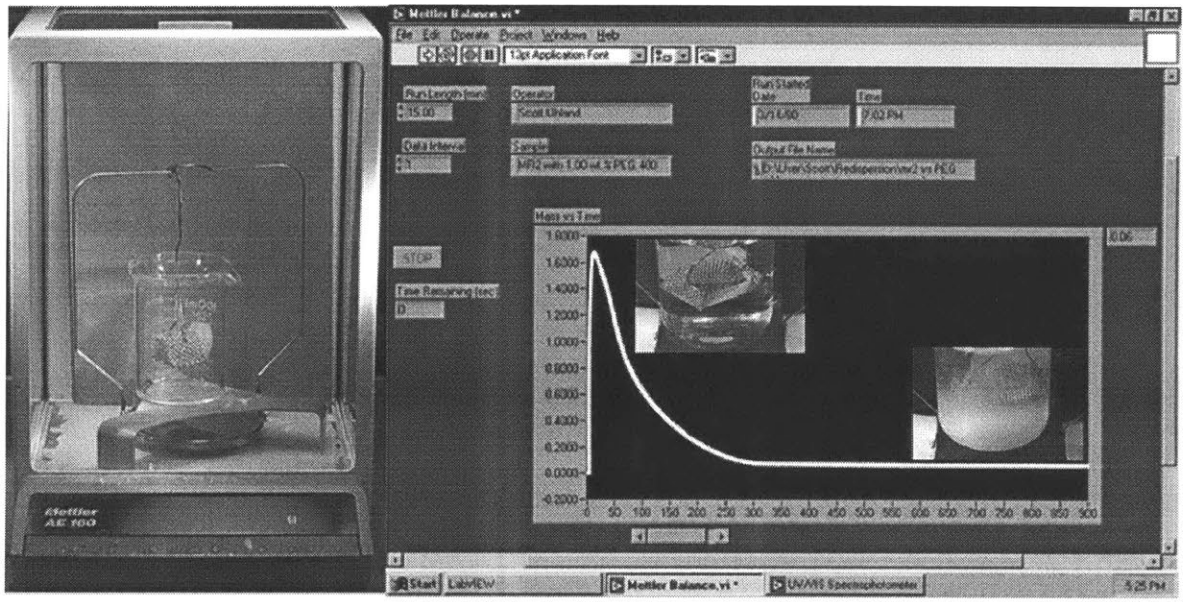

Figure 3- 3: Redispersion Measurement Instrumentation.

$$\dot{r} = \frac{\dot{m}}{\rho S_A}, \tag{3.13}$$

where $\dot{m}$ is the measured rate of mass loss, ρ is the density of PEG and S_A is the measured surface area of the pressed disk.

3.4.6. Carbon Analysis of TiO_2 Powder Beds

Total carbon analyses were performed on TiO_2 powder beds containing 0.0 vol.^{PORE}%, 1.7 vol.^{PORE}%, 3.5 vol.^{PORE}%, 5.2 vol.^{PORE}% and 7.0 vol.^{PORE}% PEG 400. The powder beds were crushed and the total carbon content was determined using the ASTM D5373 standard (LECO CR12, high temperature combustion, infrared detection, Huffman Laboratories, Golden, CO). A TiO_2 powder bed containing 7.0 vol.^{PORE}% PEG 400 was redispersed in de-ionized water and centrifuged. The supernatant was decanted followed by drying and crushing the ceramic cake. The crushed powder was analyzed for total carbon content.

3.4.7. Determination of the Swelling of Redispersing Powder Beds

MR2 S-3DP powder beds constructed of twelve, 80 μm layers were fabricated on boro-silicate substrates (20 mm x 20 mm x 8 mm, Ace Glass, Vineland, NJ). The bed and its substrate were positioned on a support frame and placed into contact with the redispersing medium (see Figure 3- 4). The absolute height of the powder bed was electronically recorded at intervals of 50 milliseconds using a laser point range sensor (Cyber Optics, Minneapolis, MN).

3.5. Results

3.5.1. Effects of PEG on the Redispersion of TiO_2 Powder Beds

TiO_2 powder beds that contained no PEG did not redisperse. Figure 3- 5 illustrates that the redispersed mass for powder beds containing no PEG as a function of redispersing solution pH. The quantity of redispersed mass was very low for all pH conditions and no redispersion was visible. The maximum mass reduction observed is 1.6 wt.% at pH 5 and the minimum is 0.4 wt.% at pH 6. The bulk of mass reduction was observed to result from small pieces of powder bed breaking off upon impact with the

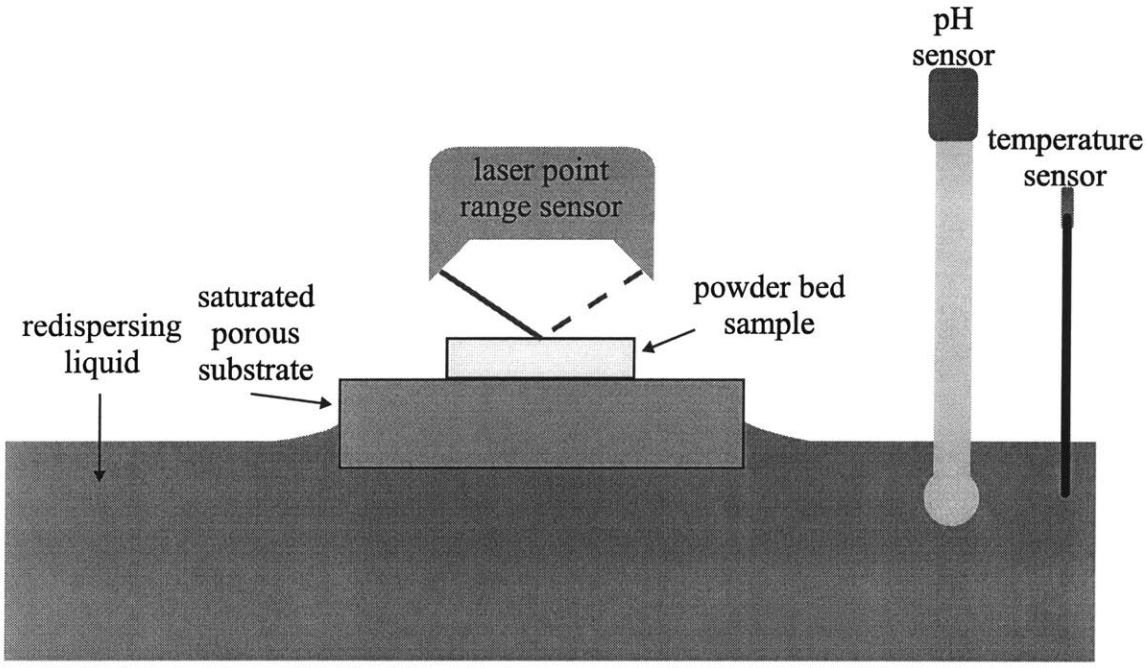

Figure 3- 4: Swelling Observation Instrumentation.

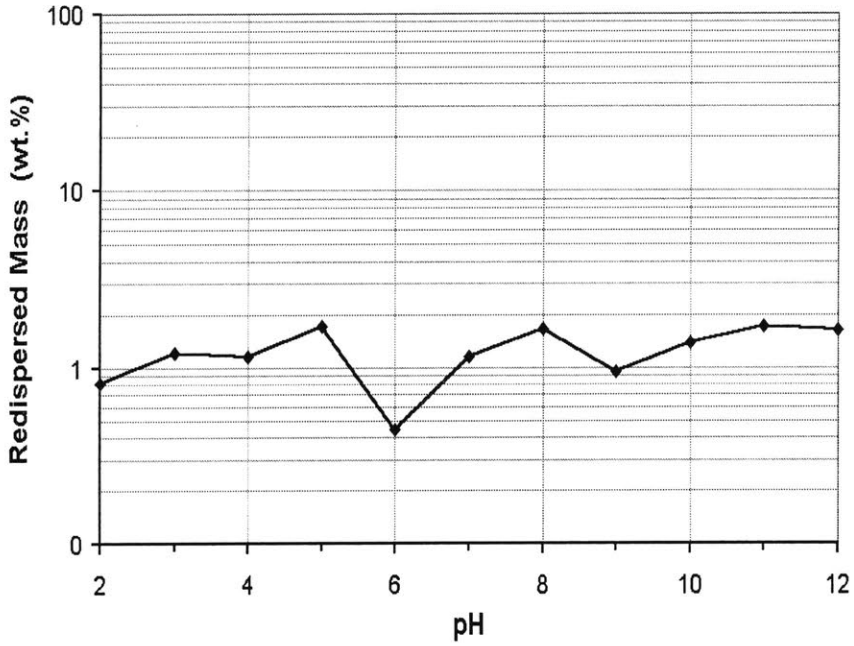

Figure 3- 5: Effects of Solution pH on the Redispersion of Titania Powder Beds.

sample holder. The pH range that was examined represents a total change in zeta potential of 100 mV (Figure 3- 6). This demonstrates that electrostatic repulsive forces are insufficient to redisperse the powder bed, which is in accordance with DLVO theory.

Redispersion dramatically improved for the powder beds that were prepared with PEG 400. The results are shown in Figure 3- 7. The amount of redispersed powder bed increased from < 1 wt.% for polymer-free powder beds to 99 wt.% for powder beds containing 7.0 vol.^{PORE}% PEG 400. The effects of PEG powder bed concentration was investigated and the results are shown in Figure 3- 8. The quantity of redispersed powder bed is essentially constant and very small with values reaching only 2 wt.% for PEG concentrations ranging from 0.0 – 1.5 vol.^{PORE}%. The mass loss due to redispersion increases to 10 wt.% for powder beds containing 2.0 vol.^{PORE}%. A large jump in the redispersed mass is observed upon further increasing the PEG-powder bed content as redispersion escalates rapidly to a value of 68 wt.% at 2.7 vol.^{PORE}%. Compete redispersion is obtained at 7.0 vol.^{PORE}% PEG 400. The maximum rate of redispersion is also shown in Figure 3- 8 for powder beds containing PEG 400. Rates of <0.1 sec^{-1} were measured for powder beds containing 0.0 to 1.5 vol.^{PORE}% PEG 400. The rate drastically increased from 0.6 sec^{-1} to 3.2 sec^{-1} by increasing the PEG concentration from 2.0 – 2.7 vol.^{PORE}%. The maximum measured rate was 5.1 sec^{-1} for a powder concentration of 7.0 vol.^{PORE}% PEG 400.

The effect of PEG molecular weight was examined for TiO_2 powder beds that contained 7.0 vol.^{PORE}% PEG (Figure 3- 9). Powder beds containing PEG 300 and PEG 400 had similar redispersed masses with values of 98 wt.% and 99 wt.%, respectively. The redispersion rate was slightly higher for the powder bed containing PEG 300 (7 sec^{-1}) in comparison to the bed containing PEG 400 (5 sec^{-1}). Increasing the molecular weight of PEG to 1000 g/mole had an adverse effect on redispersion. The total mass loss was reduced to 26 wt.% by increasing PEG's molecular weight to 1000 g/mole while the rate of redispersion decreased to 2.9 sec^{-1}. The redispersion characteristics continued to decrease as the molecular weight increased to 6000 g/mole (Table 3- 5).

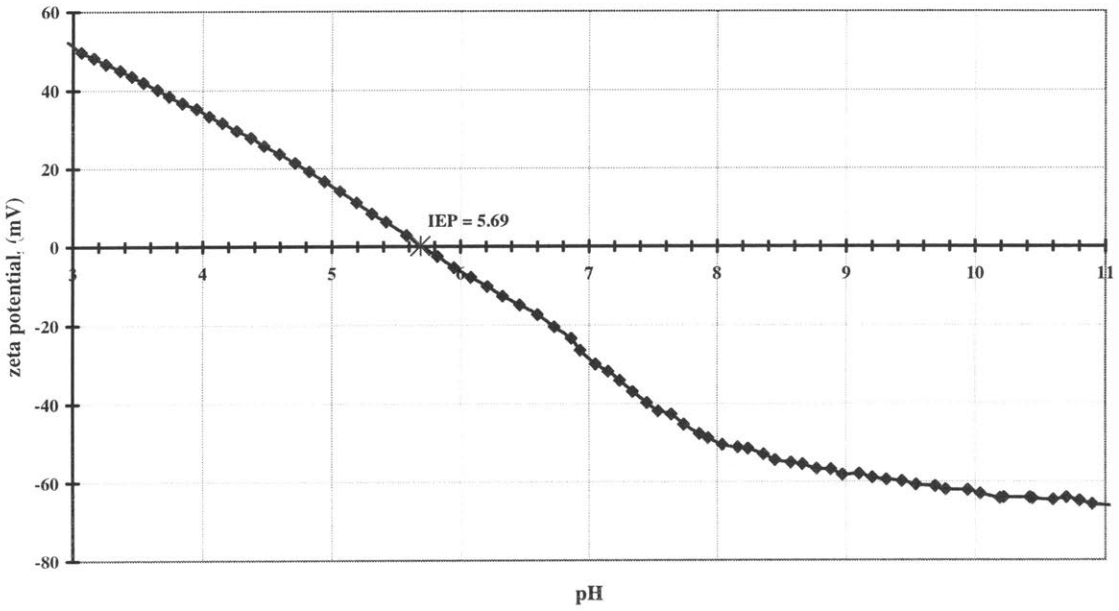

Figure 3- 6: Zeta Potential Characteristics of TiO_2 (Iso-Electric Point = pH 5.69).

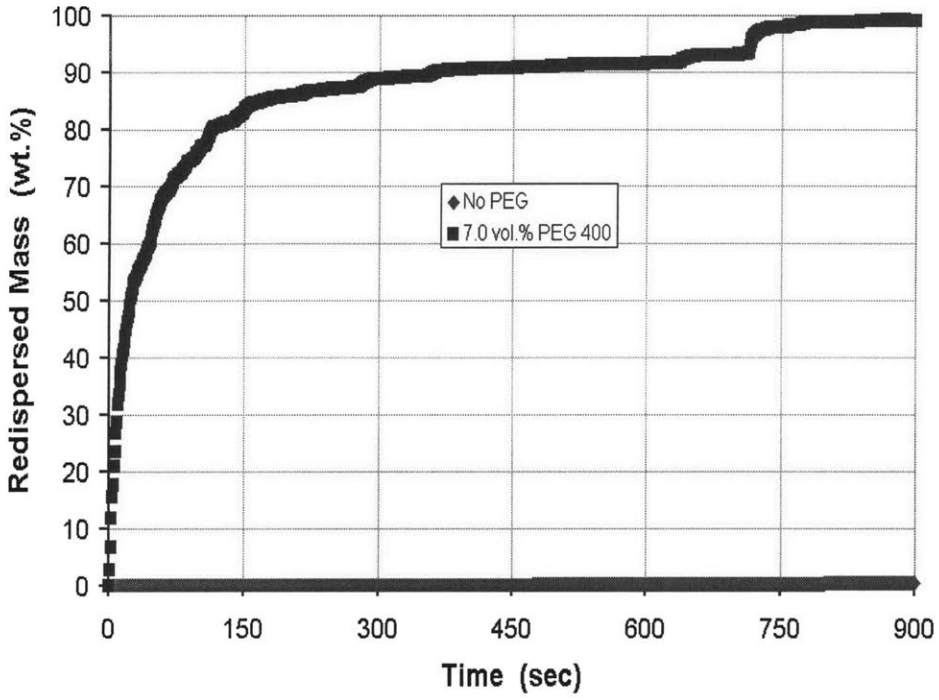

Figure 3- 7: Powder Bed Redispersion vs. Slurry PEG Content.

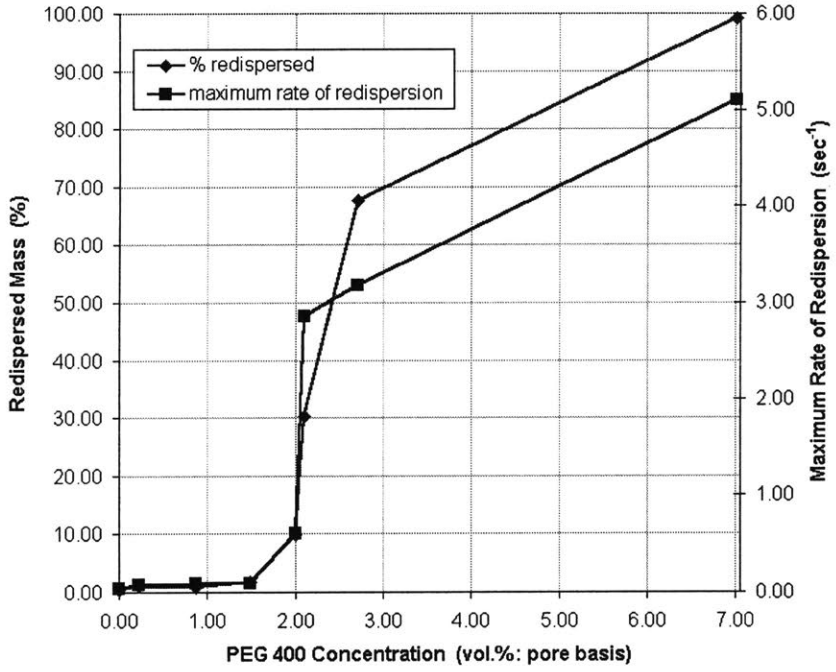

Figure 3- 8: Powder Bed-PEG Concentration and Its Influence on Redispersion.

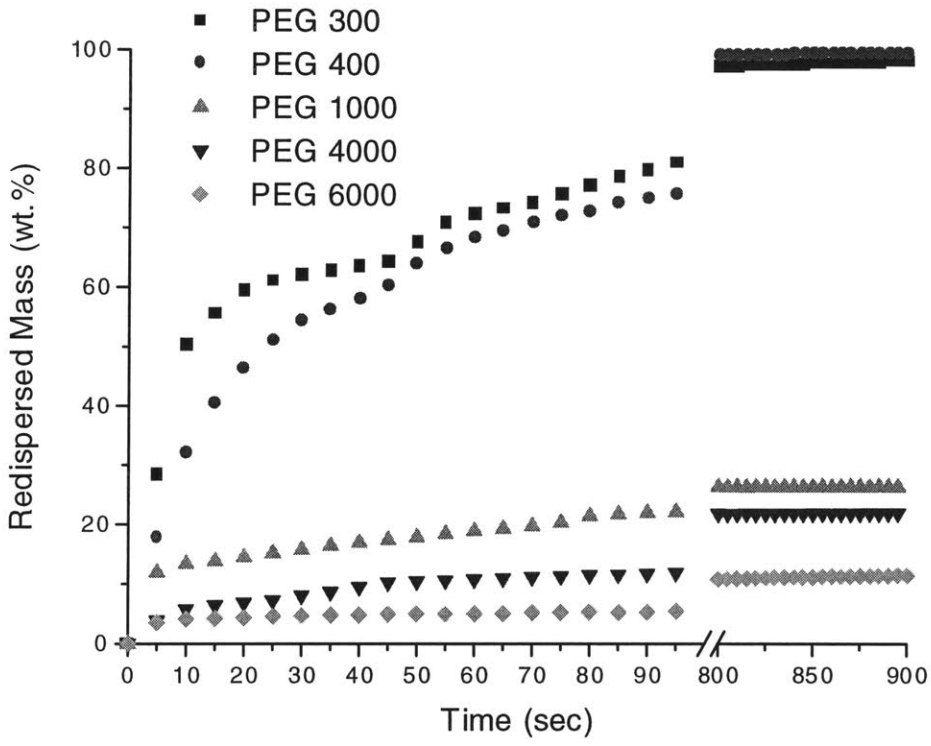

Figure 3- 9: Molecular Weight Effects on TiO_2 Redispersion.

3.5.2. *Carbon Analysis of TiO_2 Powder Beds*

Total carbon content measurements for powder beds containing 0.0 vol.^{PORE}%, 1.7 vol.^{PORE}%, 3.5 vol.^{PORE}%, 5.2 vol.^{PORE}% and 7.0 vol.^{PORE}% PEG 400 are given in Table 3- 4. The table also reports the total carbon content for a redispersed powder bed that previously contained 7.0 vol.%^{PORE} PEG 400. The redispersed powder bed and the powder that contained no PEG have similar carbon concentrations (< 500 ppm). This shows that PEG is not retained on the surface of the TiO_2 during redispersion. This is in good agreement with the work of Walker[94] and Mathur[95], who have shown that PEG adsorbs only to strongly acidic oxide surfaces via an acid-base reaction at the ether linkages. It can be deduced that the PEG contained within the powder bed is completely dissolved within the pores during redispersion. Thus, the PEG concentration in the redispersing solution within the powder bed's pore structure is equal to the initial concentration of PEG in the pores, C_{PEG}^{Pore}.

3.5.3. *Effect of PEG on the Redispersion of SiO_2, Al_2O_3 and MR2 Powder Beds*

Similarly, PEG improved the redispersion of SiO_2 and Al_2O_3 powder beds. The addition of 7.0 vol.^{PORE}% PEG 400 to the composition of the powder bed increased the total redispersed mass by 95 wt.% and 97 wt.%, respectively. The redispersion rates for the silica powder bed increased from 0.2 to 3.6 while the rates for the alumina system increased by a factor of 8 (see Table 3- 5). Aqueous redispersion of MR2 powder beds was also enhanced by the presence of PEG in the powder bed. Little redispersion was observed for powder beds without PEG (~ 1.0 wt.%, Figure 3- 10). The addition of 5.0 vol.^{PORE}% PEG 400 to the powder bed increased the redispersed mass to nearly 100 %.

3.5.4. *Expansion of MR2 Powder Beds During Redispersion*

Saturated powder beds containing PEG were observed to expand or "swell" when placed in contact with water, as shown in Figure 3- 11. This swelling phenomenon was examined during the initial redispersion stages of MR2 powder beds using a laser point range (Figure 3- 4). The relative increase in powder bed height was recorded over time as a function of PEG concentration and molecular weight. The results are presented in

Table 3- 4: Powder Bed Carbon Content.

Sample ID	Total Carbon (wt.%)
TiO_2 Powder Bed	< 0.05
TiO_2 Powder Bed + 0.46 wt.% PEG 400	0.25
TiO_2 Powder Bed + 0.93 wt.% PEG 400	0.48
TiO_2 Powder Bed + 1.39 wt.% PEG 400	0.70
TiO_2 Powder Bed + 1.85 wt.% PEG 400	0.95
Washed - TiO_2 Powder Bed + 1.85 wt.% PEG 400	< 0.05

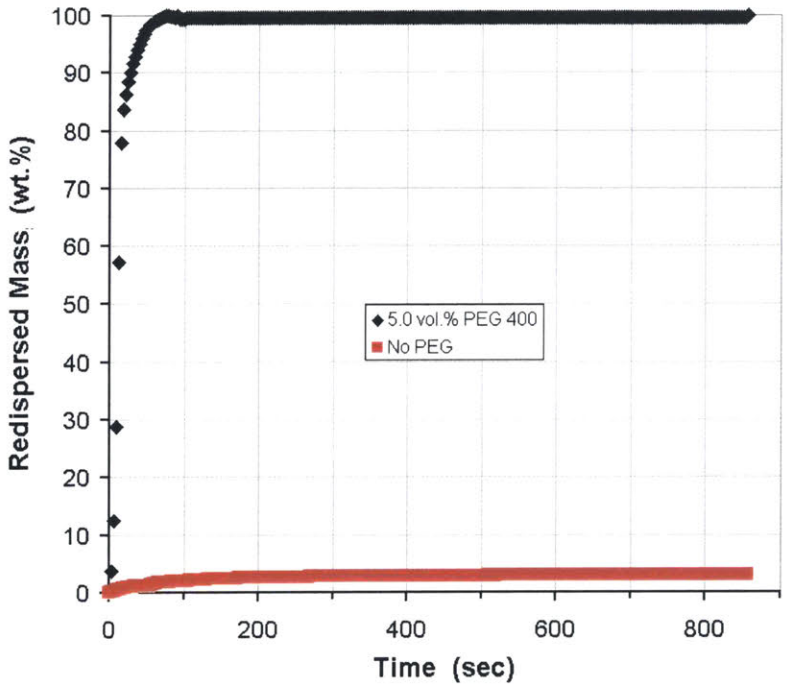

Figure 3- 10: Redispersion Behavior of MR2 Powder Beds.

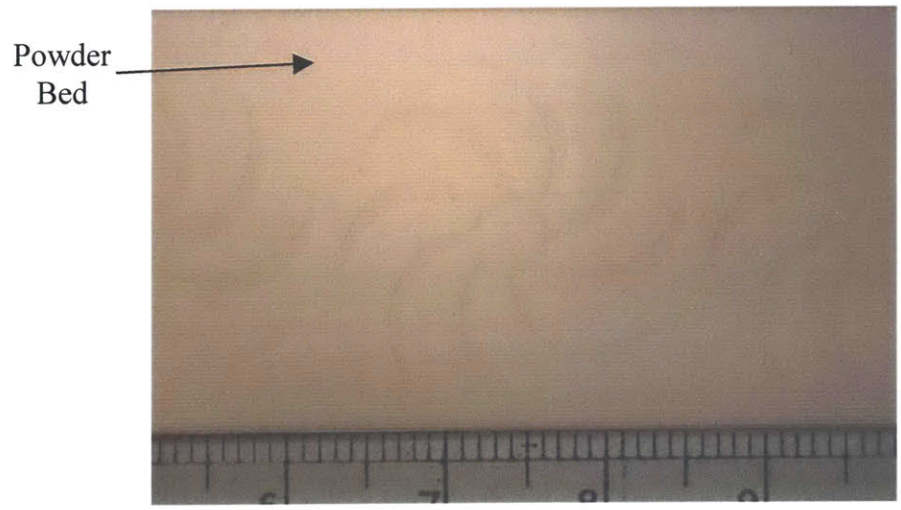

a)

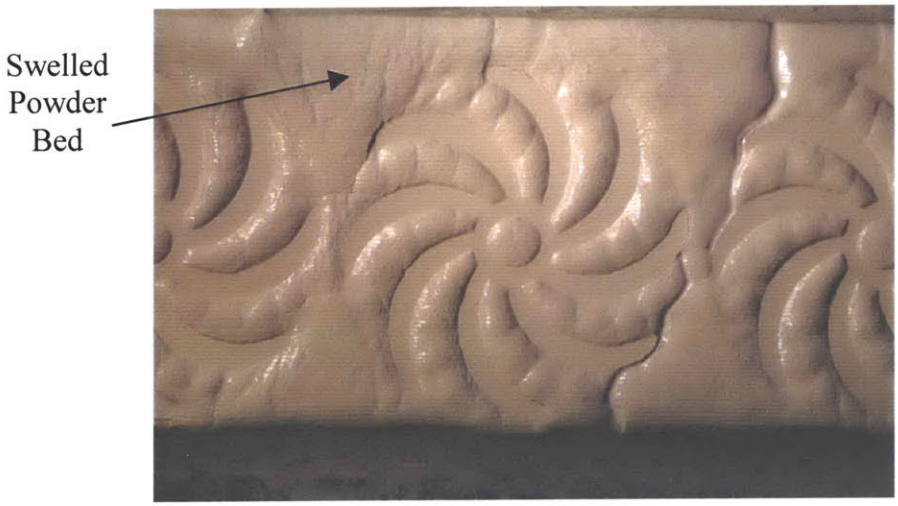

b)

Figure 3- 11: a) MR2 Powder Bed Prior to Redispersion and b) Saturated MR2 Powder Bed "Swelling" During the Initial Stages of Redispersion.

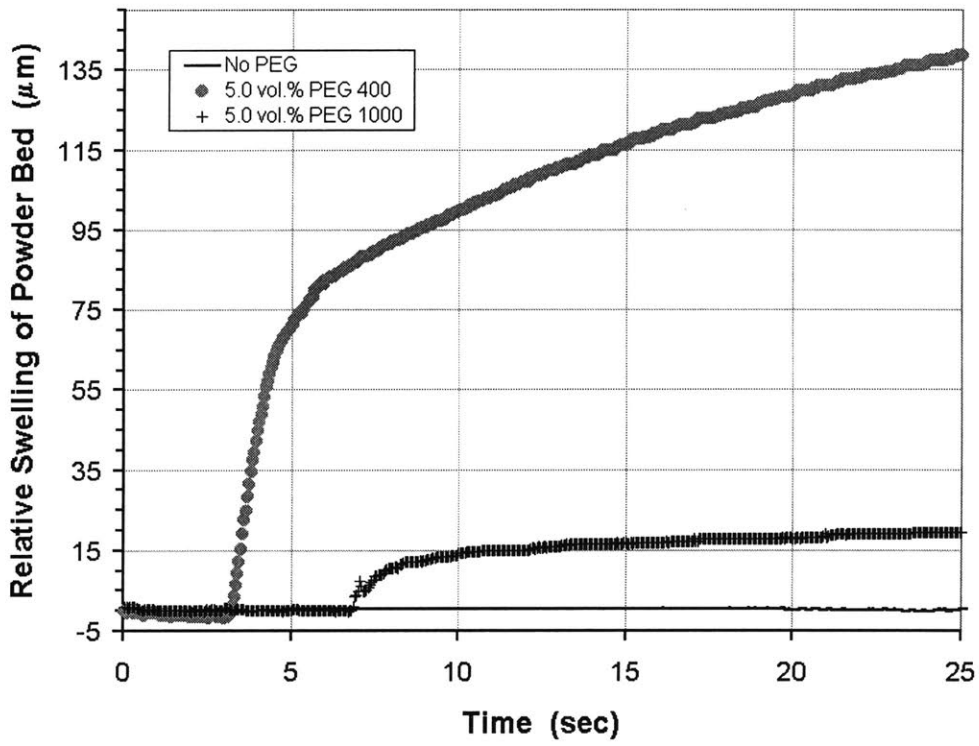

Figure 3- 12: Swelling Characteristics of MR2 Powder Beds.

Table 3- 5: Redispersion Observations (Redispersion Medium: H_2O, pH 5.8).

Ceramic	C_{PEG}^{Pore} (vol.^{PORE}%)	MW	Redispersed Mass (wt.%)	Redispersion Rate (sec^{-1})
TiO_2	0.0	-	< 1	< 0.1
	0.2	400	1.0	< 0.1
	0.9	400	< 1	< 0.1
	1.5	400	1.7	< 0.1
	2.0	400	9.8	0.6
	2.1	400	30.3	2.9
	2.7	400	67.6	3.2
	7.0	400	99.2	5.1
	7.0	300	97.9	6.7
	7.0	1000	26.2	2.9
	7.0	4000	21.6	0.9
	7.0	6000	9.4	0.4
SiO_2	0.0	-	4.2	0.2
	7.0	400	99.0	3.6
Al_2O_3	0.0	-	2.5	< 0.1
	7.0	400	99.5	0.8
MR2	0.0	-	3.0	0.1
	5.0	400	99.9	9.4

Figure 3- 12. No expansion was observed for the powder beds without PEG, while the PEG 400 and PEG 1000 powder bed samples expanded. The initial rates of expansion (0 to 10 secs) for the powder beds containing 5.0 vol.^{PORE}% PEG 400 were measured to be 58 μm/sec ± 13%. Powder bed containing 5.0 vol.^{PORE}% PEG 1000 yielded expansion rates of 14 μm/sec ± 17%. It was also observed that upon complete saturation, both powder beds that contained PEG contracted just prior to swelling while the powder bed contain no PEG remained at the same height. The slight shrinkage is likely the result of particle rearrangement due to dissolution of PEG. The total absolute swelling values widely varied from 10% to 35% of the initial powder bed height (1 mm) for the PEG 400 samples. This resulted from the powder beds breaking away from the borosilicate substrate, which is illustrated by the cracks present in Figure 3- 11b. It is important to note that all PEG 400 samples expanded to a greater extent than powder beds containing PEG 1000.

3.6. Discussion

The presence of PEG in the powder bed pore structure has a powerful effect on the aqueous redispersion of TiO_2 powder compacts. It is clear that PEG within the powder bed dissolves quickly and completely during redispersion. The normalized dissolution rate of PEG 1000 is ~$1.9*10^{-4}$ cm/sec. The time for complete PEG dissolution for a powder bed containing 7.0 vol.^{PORE}% polymer (note that this is the maximum concentration studied) is calculated by considering two possible conditions with respect to the wetting characteristics of PEG on the ceramic powder: perfectly wetting and perfectly non-wetting. The former case results in a PEG thickness equal to the volume of PEG in the powder bed divided by surface area of the powder ($5*10^{-7}$ cm). The latter yields an effective thickness that is equal to the ratio of the non-wetting PEG volume within a pore to its surface area ($8*10^{-5}$ cm). The dissolution times corresponding to these cases are ~3 msec and ~100 msec for the case of titania. Both of these time scales are at least two orders of magnitude less than the time scale of initial experimental observations.

The concentration of PEG in the solution with the pore structure of the powder bed during redispersion is equal to the initial concentration of PEG within the pores of the powder bed. The absolute quantity of PEG within the redispersing powder bed is assumed constant during the redispersion tests. This is supported by the studies of Waggoner[96], who has found the diffusivity of PEG in water to range from $3*10^{-6}$ cm^2/sec to $6*10^{-7}$ cm^2/sec for molecular weights varying from 400 to 6000 g/mole, respectively. The majority of the redispersion observations occurred during the initial stages (~10 seconds) of the experiments. The diffusion length of PEG 400 with respect to this time scale is approximately:

$$l \approx \sqrt{Dt} = 50\mu m . \tag{3.14}$$

This length is negligible with respect to the dimensions of the redispersion samples (12.5 mm x 4 mm x 3 mm). Moreover, this diffusion scale is largely over–estimated since diffusion must occur through the tortuous pore structure of the powder bed.

The osmotic pressure, π, of aqueous PEG solutions has been studied for many years in the biological sciences[97-99] and has been measured by various techniques[100,101]. More recently, Eliassi[102] has determined the activity of water in aqueous PEG solutions to behave as a third–order polynomial:

$$a_S = c_1 x_S^3 + c_2 x_S^2 + c_3 x_S + c_4 , \tag{3.15}$$

where x_S is the weight fraction of water in solution. The osmotic pressure of the PEG 300, PEG 400, PEG 4000 PEG and 6000 solutions is calculated by using Eliassi's activities in Eqs. 3.7 and 3.8. The corresponding osmotic pressures are given in Figure 3- 13. These osmotic pressures represent the stresses that exist between the PEG solutions within the pore structure of the powder bed and the pure water redispersing solvent that surrounds the redispersing powder bed.

The cohesive strength of S-3DP titania powder beds has been previously determined to be 177 kPa[91] ± 0.012 kPa for PEG–free specimens and 185 kPa[91] ± 0.015 kPa for specimens containing 7.0 vol.^{PORE}% PEG 400. Figure 3- 14 compares the total redispersed mass and the respective osmotic driving force as a function of C_{PEG}^{Pore} with the cohesive strength of the powder bed. Substantial redispersion is attained when

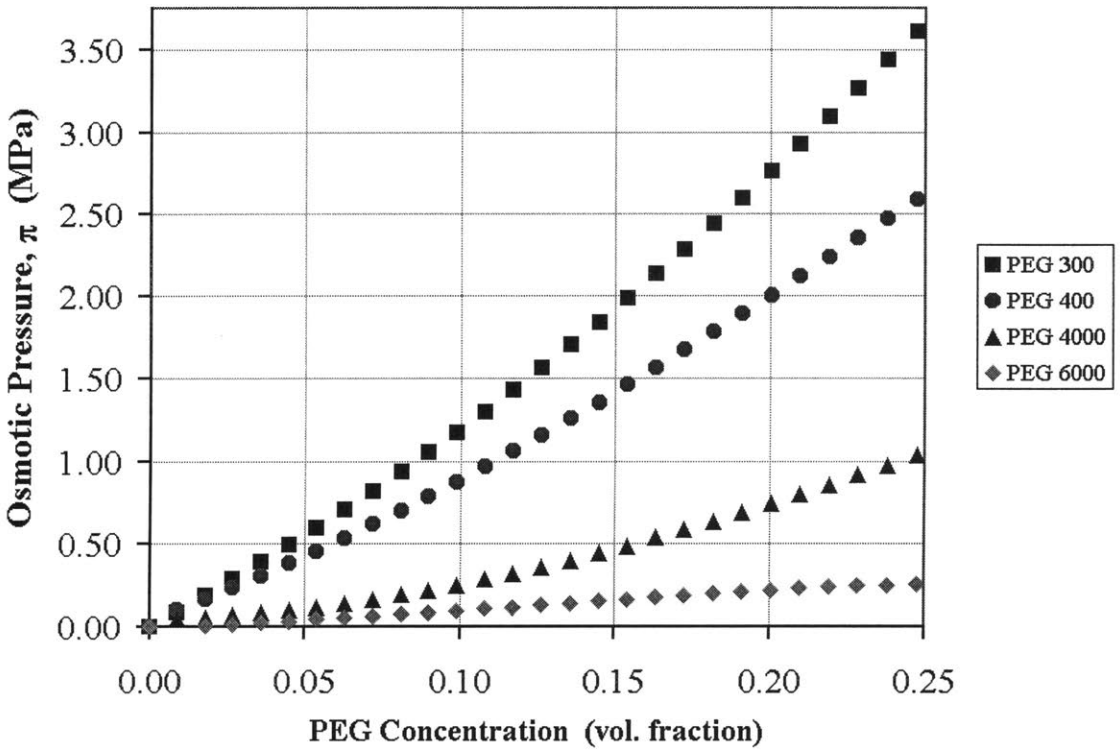

Figure 3- 13: Osmotic Pressure for PEG Solutions (PEG 300, PEG 400, PEG 4000 and PEG 6000) as a Function of Polymer Concentration.

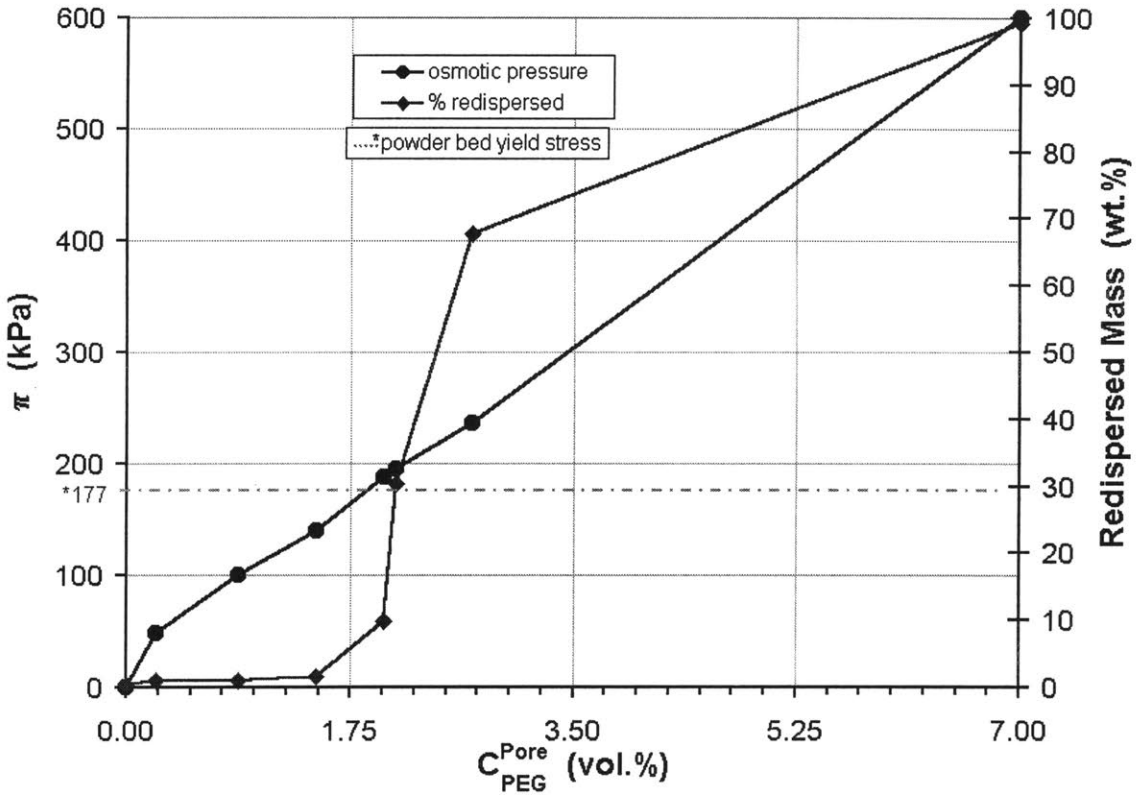

Figure 3- 14: Osmotic Redispersive Forces as a Function of PEG Solution Concentration in TiO_2 Powder Beds. Cohesive Strength of TiO_2 Powder Bed = 177 kPA ± 11%.

the osmotic stresses exceed the fracture stress of the powder bed. A significant increase in redispersion occurs when the osmotic pressure is equal to the cohesive strength of the powder bed. The PEG concentration at which the osmotic pressure is equal to the cohesive strength of the powder bed represents a lower limit that is required to achieve significant redispersion. This critical value is calculated as:

$$\sigma_{PowderBed}^{yield} \equiv \pi(C^*). \tag{3.16}$$

The minimum concentration corresponding to this specific study is $C_{PEG}^{Pore} = 2.0$ vol.% for PEG 400.

Redispersion is also influenced appreciably by the molecular weight of the polymer. The osmotic driving force of the powder bed containing PEG 300 is larger than that of the PEG 400 (Figure 3- 13), which produces a higher redispersion rate (Table 3- 5); however, complete redispersion is obtained for both PEG 300 and PEG 400 (Figure 3- 9) samples since their osmotic pressures are greater than the strength of the titania bed. Increasing the molecular weight from 400 g/mole to 6000 g/mole reduces the osmotic pressure by an order of magnitude, from 600 kPa to 63 kPa. This value is below the fracture stress of the powder bed and a large decrease in the powder bed redispersion behavior results.

Figure 3- 15 calculates the observed relationship between the maximum rate of redispersion and the molecular weight of PEG to be:

$$R_{\mathrm{Re}dispersion}^{Max} \propto M_W^{-0.89}. \tag{3.17}$$

The redispersion rate is determined by the flow rate of water into the redispersing powder bed. The flow rate of water into the redispersing powder bed is related to the osmotic pressure according to D'Arcy's law:

$$Q = \frac{Ak_p\pi}{\eta_l L}, \tag{3.18}$$

where A is the cross-sectional area, k_P is the specific permeability, η_l is the viscosity of the infiltrating liquid, and L is the infiltrating distance. Van't Hoff's law states that the osmotic pressure varies inversely with the molecular weight of the dissolved polymer:

$$\pi \propto M_W^{-1}. \tag{3.19}$$

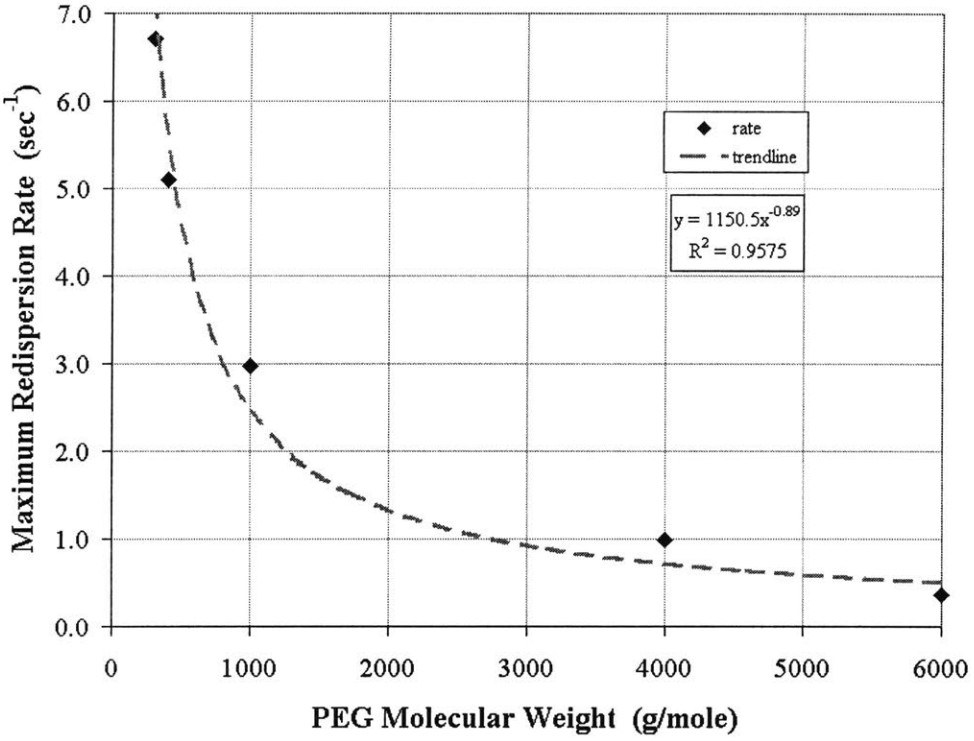

Figure 3- 15: Maximum Rate of Redispersion Behavior as a Function of PEG's Molecular Weight.

Combining Eqs. 3.18 and 3.19, the volumetric flow rate varies with the molecular weight of the polymer as:

$$Q \propto M_W^{-1}. \tag{3.20}$$

The experimental and calculated rates are in very good agreement with respect to the effect of molecular weight. Equation 3.20 is a simplified relationship. The osmotic pressure is a function of the polymer solvent interaction parameter, χ, as expressed in Eq. 3.10. The interaction parameter has been proven to vary with the molecular weight and concentration of the PEG solution, as shown in Figure 3- 16. Therefore, the effect of molecular weight is more complex than the expression given in Eq. 3.20, however these effects are negligible at low concentrations (Eq. 3.10).

Silica and alumina powder beds support the osmotic redispersion theory. The fracture stresses of the silica powder beds have been determined to be 157[91] ± 0.017 kPa for PEG–free specimens and 149 kPa ± 0.016 kPa for specimens containing 7.0 vol.^{PORE}% PEG 400, while the fracture strength of alumina powder beds was observed to be 340 kPa[91]. The silica and alumina powder beds contained 7.0 vol.^{PORE}% PEG 400, which corresponds to an induced osmotic stress of 600 kPa. This pressure exceeds the fracture stress of both the silica and alumina powder beds; hence redispersion results. Examination of the redispersion rates (Table 3- 5) shows that the maximum rate of redispersion for alumina (0.8 sec^{-1}) was much lower than the rates for TiO_2 and SiO_2 (3.6 and 5.1 sec^{-1}). The rate of redispersion is dependent on the flux of water into the redispersing body. According to D'Arcy's law (Eq. 3.18), the flux of liquid is a function of the permeability of the powder bed. The Carmen-Kozeny equation defines the specific permeability to be:

$$k_P = \frac{(1-\phi)R^2}{k_o}, \tag{3.21}$$

where ϕ is the packing fraction, k_o is a constant (typically ~5) and R is hydraulic radius representative of the pore structure, which is calculated as:

$$R = \frac{1-\phi}{S\phi}, \tag{3.22}$$

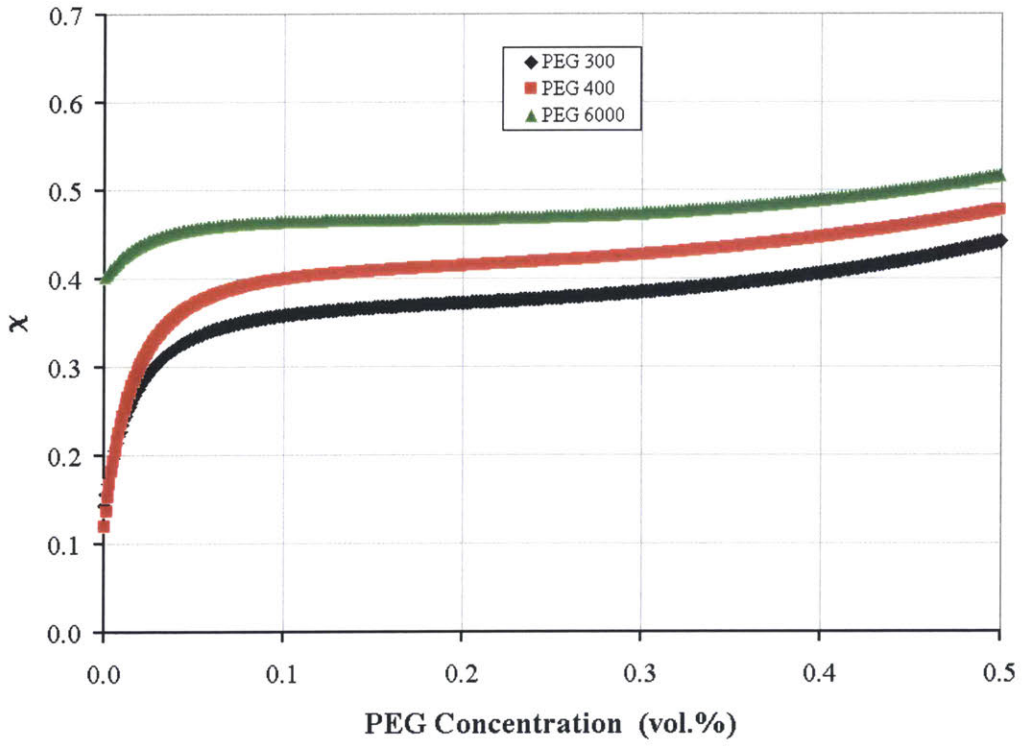

Figure 3- 16: Polymer Solvent Interaction Parameter for Aqueous PEG Solutions as a Function of Molecular Weight and Concentration.[102]

where S is the specific surface area per unit volume of the particle. Table 3- 6 shows the calculated permeabilities for the TiO_2, SiO_2 and Al_2O_3 powder beds based on the data given in Table 3- 1 and Table 3- 3. The permeability of the alumina powder beds is the lowest of the three powder beds (since it has the highest packing density and surface area) and therefore, is expected to have the slowest redispersion rate. The permeability also suggests that the rate of redispersion for SiO_2 should be less than that of TiO_2, which is the case.

The influence of osmotic pressure on the redispersion of MR2 is realized by examining the uniaxial expansion rates of the powder beds during the initial stages of redispersion (Figure 3- 12). The measured expansion rates for the 5.0 vol.^{PORE}% PEG 400 and 5.0 vol.^{PORE}% PEG 1000 powder beds are 58 μm/sec and 14 μm/sec, respectively. This swelling is caused by the flow of water into the powder bed. The osmotic potential that exists between the PEG solution in the pore structure and the pure solvent outside of the redispersing bed forces water into the powder bed, as shown in Figure 3- 17. The liquid flux, q, is calculated as:

$$q = \frac{Q}{A} = \frac{k_p \pi}{\eta_l L}, \tag{3.23}$$

where q has units of μm/sec. The MR2 powder beds containing 5.0 vol.^{PORE}% PEG 400 develop osmotic stresses of approximately 430 kPa during redispersion. The corresponding calculated liquid flux is 72 μm/sec based on the powder bed properties given in Table 3- 1 and Table 3- 3. The osmotic pressure for the powder bed containing 5.0 vol.^{PORE}% PEG 1000 is 89 kPa[97], and the respective flux is computed to be 15 μm/sec.

The redispersion process of MR2 powder beds is more complex that the previous simple oxide systems. The osmotic potential that is developed during redispersion for MR2 powder beds containing 5.0 vol.%^{PORE} PEG 400 is equal to 430 kPa. The fracture strength of MR2 powder beds has been measured to be 1.43 MPa[91]. Straightforward comparison of the fracture strength with the osmotic potential is very difficult in this case. The dry fracture strength of MR2 powder beds is very high due to the presence of a water–soluble dispersant (ammonium polyacrylate), which acts as a binder at the particle

necks. The strength is drastically decreased by the removing the dispersant from the particle necks. Flexure tests show that the dry strength of MR2 powder beds are reduced to 610 kPa ± 9% [91] after thermally removing the dispersant. This value remains 40% larger than the osmotic forces due to PEG 400. This is likely a result of residual carbon bridges remaining at the particle necks. Another possible phenomenon that increases the dry strength is the crystallization of dissolved species at the particle necks. Oxides containing barium, such as MR2, are known to be soluble in aqueous environments[69,70], and this solubility can be appreciable if pH is not carefully monitored. Secondly, the water–soluble dispersant is hydrated during redispersion. The polymeric dispersant provides some osmotic pressure of its own; however, the exact potential developed is difficult to determine since a fraction of the dispersant is adsorbed to the surface of the particles.

The comparison of the dry flexural strength and the osmotic stresses is not completely accurate and is extremely complex. The strength of an agglomerate is a function of many different variables such as packing density[46], critical flaw size[53] and inter–particle forces. Therefore, the strength of a completely saturated powder bed during redispersion varies dramatically with respect to the dry strength.

The strength of an agglomerate is expected to decrease when placed in a dielectric medium such as water. Eqs. 3.1 and 3.2 state the cohesive strength of an agglomerate to be:

$$\sigma \propto F_A^{vdW} . \tag{3.24}$$

The van der Waals force, F_A^{vdW}, is given by Hamaker's expression:

$$F_A^{vdW} = \frac{Ar}{6h^2}, \tag{3.25}$$

where r is the particle radius, h is the separation distance between particles and A is the Hamaker constant. Lifshitz[75] has shown that the van der Waals force for ceramic particles decreases in the presence of an intervening medium:

$$A = c\left(\frac{\varepsilon_s - \varepsilon_l}{\varepsilon_s + \varepsilon_l}\right)^2, \tag{3.26}$$

Table 3- 6: Powder Bed Permeabilities.

Powder Bed	Permeability ($*10^{12}$ cm^2)
TiO_2	6.1
SiO_2	5.5
Al_2O_3	3.5

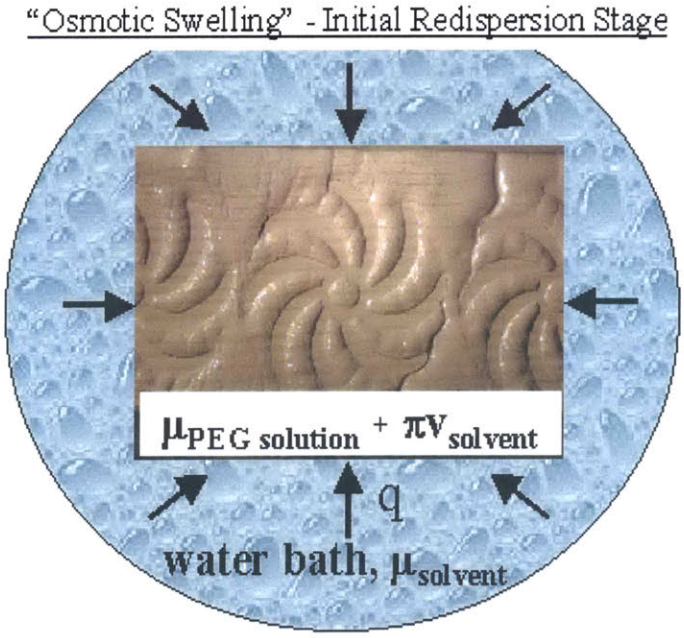

Figure 3- 17: Swelling of Powder Bed Due to Osmotic Pressure.

Table 3- 7: Hamaker Constants for TiO_2, Al_2O_3 and SiO_2[55].

Ceramic	Hamaker Constant in Air, A (J)	Hamaker Constant in Water, A (J)
TiO_2	$43*10^{-20}$	$26*10^{-20}$
Al_2O_3	$14*10^{-20}$	$4.6*10^{-20}$
SiO_2	$6.3*10^{-20}$	$0.6*10^{-20}$

where ε_s is the dielectric constant of the particles and ε_l is the dielectric constant of the medium. Table 3- 7 shows the effect of water on the Hamaker constant for the TiO_2, Al_2O_3 and SiO_2 ceramic systems. According to equations 3.25 and 3.26, the van der Waals forces for TiO_2, Al_2O_3 and SiO_2 are reduced by 42%, 67% and 90%, respectively, due to the presence of water. These theoretical decreases represent a relative increase in the osmotic potentials involved during the redispersion process; hence osmotic stresses become more significant for enhancing the redispersion of agglomerated ceramic bodies. The results from the titania system support this theory. The reduced strength of titania in water is ~100 kPa. This value is close to the osmotic stress of ~90 kPa corresponding to the titania powder bed that contained 7.0 vol.^{PORE}% PEG 6000. Hence, some redispersion occurs at this osmotic pressure.

3.7. Conclusions

Osmotically–enhanced redispersion has been proven for the titania, silica, alumina and MR2 agglomerate systems. The key to achieving redispersion is the development of osmotic pressures that exceed the cohesive strength of the agglomerated structure. PEG is a very effective polymer since it yields high osmotic potentials when dissolved in water. A critical PEG concentration has been determined below which redispersion is minimal while the molecular weight must be minimized in order to maximize the osmotic pressure. It is important to recognize that all of the studies were conducted using the PEG-water system; however many other polymer-solvent systems exist that can produce appreciable osmotic potentials. The use of Flory-Huggins theory for the thermodynamics of polymer solutions is an essential tool that helps to select and evaluate viable polymer-solvent systems.

Chapter Four

The Mechanical Properties of Green Ceramics with Low Binder Content

4.1. Introduction

Strength at low binder concentrations may be determined by chemical bonding at the ceramic–polymer interface. Generally, studies that focus on this theme vary the binder chemistry and content while fixing the ceramic material[103,104]. This study examines the binding mechanisms as a function of ceramic surface chemistry using a cross-linkable polyacrylic acid (PAA). PAA is an excellent candidate because it is representative of a class of acrylic based polymers that are commonly used as binder systems for many different ceramic forming processes[105-108]. PAA has therefore been studied for many years and the surface adsorption mechanisms are well defined[109-112]. Additionally, PAA can be crosslinked using a variety of techniques[113,114], which allows for excellent control over the mechanical and chemical properties of the binder phase[115,116]. The ceramic systems investigated are SiO_2, TiO_2, Al_2O_3 and MR2, which represent a wide range of surface chemistries. These materials systems are integrated into the S-3DP process in order to fabricate green bend bars for mechanical evaluation. ASTM standards 1161-94 and 1421-99 are used to measure the impact of the crosslinked PAA binder on the strength and fracture toughness of the bars. The mechanical properties are compared and contrasted with the surface adsorption characteristics of PAA for each ceramic system.

4.2. The Strength of Green Ceramic Bodies

The purpose of binder is to impart sufficient strength to the green body so that it maintains its shape through pre-sintering processing steps. An important requirement of the binder is that it can be removed completely prior to sintering without deforming the green body. This necessitates that the binder concentration is minimized. Failures often occur during the machining, inspection and storage of the green components due to

inadequate green strength. Therefore, knowledge of the factors that control the strength of green bodies with low binder content is essential in order to improve the yield of post–consolidation steps.

A model for the strength of particulate bodies consisting of randomly–packed spheres of uniform size has been developed by Rumpf[41] to be:

$$\sigma = \frac{27\phi}{32(1-\phi)\pi r^2} F \,, \tag{4.1}$$

where ϕ is the packing fraction of the particles, r is the particle radius and F is the inter-particle bond strength. Onoda[117] has used Rumpf's theory to determine the theoretical dry strengths of green ceramics containing binders. The force required to break the inter-particle bonds depends on how much binder is concentrated at the particle necks. It is assumed that the binder forms pendular bridges (Figure 4- 1a) due to capillarity in which case the cross-sectional area of the binder at the neck is:

$$A = \frac{4\pi r^2 (1-\phi)^{\frac{1}{2}}}{3} (v_B)^{\frac{1}{2}} \,, \tag{4.2}$$

where v_B is the volume fraction of binder relative to the ceramic. The force required to rupture the binder bridge is simply:

$$F = \sigma_B A \,, \tag{4.3}$$

where σ_B is the strength of the binder. The theoretical strength of the green body is obtained by combining Eqs. 4.1 through 4.3:

$$\sigma = \frac{9\phi}{8(1-\phi)^{\frac{1}{2}}} (v_B)^{\frac{1}{2}} \sigma_B \,. \tag{4.4}$$

The strength of the binder is represented by either the polymer's cohesive strength or by the adhesion forces at the polymer-ceramic interface. The former is the case when fracture occurs through the polymer phase (Figure 4- 1b), whereas the latter pertains to fracture along the binder–ceramic interface (Figure 4- 1c). Therefore, the mechanical properties of the polymer and its affinity for the ceramic surface are two critical factors that determine the strength of the ceramic body at low binder concentrations.[48]

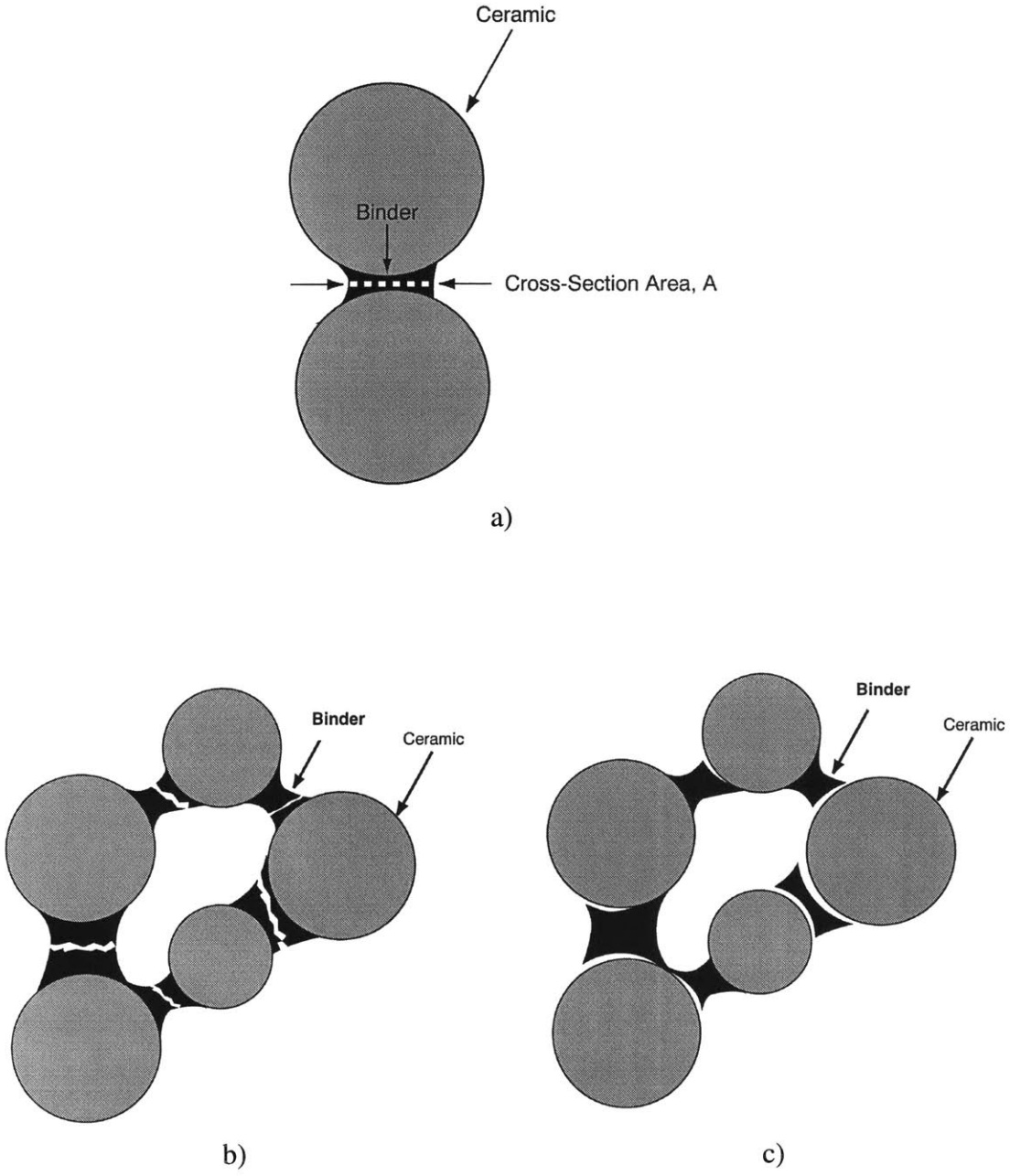

Figure 4- 1: a) Pendular State of Binder at the Particle Necks, b) Fracture through Binder Phase and c) Fracture along the Binder-Ceramic Interface.

4.3. Procedures and Methods

4.3.1. Materials

Commercially–available polyacrylic acid, PAA, (Acumer 1510, MW = 60,000 g/mole, 20 vol.% solution, Rohm and Haas, Philadelphia, PA) and glycerol (99.5%, Mallinckrodt, Paris, KT) were utilized in this study. The effectiveness of the PAA binder system was examined using four ceramic systems: SiO_2 (99.5 wt.%, Quartz, Alfa Aesar), TiO_2 (99.5 wt.%, Rutile, Alfa Aesar), Al_2O_3 (99.7 wt.%, Ceralox) and MR2. The physical properties of the powders are presented in Table 4- 1.

4.3.2. DSC and T_g Analysis

Polyacrylic acid films were formed using 10 vol.% PAA solutions containing glycerol concentrations of 0.0 wt.%, 0.1 wt.%, 1.0 wt.%, 5.0 wt.% and 10 wt.% (PAA solids basis), which were dried at 60 °C. Dry films were cured at 150 °C for one hour under flowing argon. Differential scanning calorimetry (DSC 7, Perkin Elmer, Norkalk, CT) was used to determine the glass transition temperature of the cured polymer films. The films were heated from 100 °C to 160 °C at a rate of 10 °C per minute followed by cooling to 100 °C at a rate of 20 °C per minute. This heating and cooling cycle was used to fix the thermal history of all polymer films. A second temperature scan starting from 100 °C to 160 °C at a rate of 10 °C per minute was used to characterize the polymer films. The change in the specific heat was determined for all detectable endothermic processes. The glass transition temperature was determined by extrapolation to the temperature at one half the change in specific heat. The influence of the ceramic on crosslinking was determined using cured polyacrylic acid films containing 1 wt.% glycerol. Two solutions containing 0.26 g of alumina (surface area = 1 m^2) and 0.20 g of silica (surface area = 1 m^2) were used to form films, which were subsequently dried, cured and characterized using DSC.

4.3.3. Iso-Electric Point Measurements

The potentiometric behavior and the iso-electric points of SiO_2, TiO_2 and Al_2O_3 were determined using an electro-acoustic analyzer (ESA 8000, Matec Applied Science,

Table 4- 1: Powder Characteristics.

Material	Density (g/cm^3)	APS (μm)	SSA (m^2/g)
SiO_2	2.49	0.74	5.13
TiO_2	4.26	0.52	3.31
Al_2O_3	3.96	0.48	3.98
MR2	5.9	1.26	1.11

Table 4- 2: S-3DP Slurry Chemistries.

Ceramic	Solids (vol.%)	Solvent	pH	Dispersant	Polymer Additive (wt.%)
SiO_2	30.0	Water/MeOH = 1	9.0	-	-
	30.0	Water/MeOH = 1	9.0	-	PEG 400 (3.0)
TiO_2	27.5	Water	9.5	-	-
	27.5	Water	9.5	-	PEG 400 (1.9)
Al_2O_3	30.0	Water/MeOH = 1	4.0	-	-
	30.0	Water/MeOH = 1	4.0	-	PEG 400 (2.0)
MR2	35	Water/MeOH = 1	9.5	0.4 wt.% Aron	-
	35	Water/MeOH = 1	9.5	0.4 wt.% Aron	PEG 400 (1.0)

Hopkinton, MA). Measurements were performed on 1.0 vol.% suspensions, which were ultra-sonicated for 1 minute prior to analysis. The zeta potential was measured as a function of pH by titration with 0.1 M HNO_3 and 0.1 M KOH solutions.

4.3.4. PAA Surface Adsorption

The adsorption of PAA onto SiO_2, TiO_2, and Al_2O_3 has been studied[39] at various polymer concentrations using UV absorbance analysis (DU 640 Spectrometer, Beckman Instruments Inc., Columbia, MD). The characteristic peak for Acumer 1510 PAA was identified at 211 nm and a linear relation between UV absorbance and concentration was confirmed. Samples were prepared containing 5.0 vol.%, 2.4 vol.%, 1.0 vol.%, 0.5 vol.%, 0.3 vol.%, 0.2 vol.%, 0.1 vol.%, and 0.05 vol.% PAA (liquids basis). The solutions were titrated to pH 2.05 with 1.0 M phosphoric acid, after which 20 vol.% ceramic powder was added. The slurries were ultra-sonicated for 30 seconds and tumbled for 20 hours followed by centrifugation for 1.5 hours at 7000 rpm. The supernatant was withdrawn and again centrifuged for 1.5 hours at 7000 rpm. Three UV absorbance scans were run and the results averaged for each supernatant solution. The absorbance at 211 nm was used to determine the amount of PAA remaining in solution. The difference represented the PAA adsorbed onto the ceramic surface, which was normalized by the ceramic powder's surface area.

4.3.5. Slurry Formulation

Fracture specimens were formed using various slurry formulations, which are given in Table 4- 2. All slurries were prepared in polyethylene bottles with ~1/4" zirconia milling media. Materials were added to the slurry in the following sequence: solvent, pH adjustment, dispersant and powder. Stock solutions of 1.0 M HNO_3, 1.0 M KOH and 1.0 M NH_4OH were used to adjust the pH. The dispersant (ammonium polyacrylate, MW = 2400, Aron A-30 SL, Toagosei, Japan) was mixed thoroughly with the solvent followed by the addition of PEG and milling media (~1/3 of the volume of the mixing bottle). One half of the powder was introduced into the solvent and the mixture was ball-milled for approximately 30 minutes. The remainder of the powder was added in quarters and the slurry was milled for ~16 hours.

4.3.6. Fracture Sample Formation and Preparation

Binder-free bend bars and green bars containing 2.5 vol.% PAA were generated using the S-3DP[40] process. The slurry was delivered through a 127 μm nozzle (Gaiser Tool Company, Ventura, CA) from a pressurized re-circulating system[54]. The system's pressure was adjusted in order to maintain a constant slurry flow rate. The nozzle was raster-scanned over a porous substrate (borosilicate filter, Ace Glass, Vineland, NJ) such that single lines of slurry stitch together to form a powder bed layer, as illustrated in Figure 4- 2a. Once a single layer was complete, the piston lowered the powder bed a predetermined distance, i.e. the layer height, and the "wet" slip-cast layer was dried for 30 seconds using an IR heat lamp. Binder-free bars were formed by sequentially depositing the slurry to form powder beds with a height of 3 mm and a width of 4 mm.

Green bars containing 2.5 vol.% PAA (ceramic solids basis) were fabricated using an aqueous binder solution containing 2.4 vol.% polyacrylic acid and 10 wt.% glycerol (PAA solids basis). The PAA binder solution was selectively printed into each powder bed layer to define the component's shape (Figure 4- 2b) using the standard 3DP charge and deflection continuous jet printhead technology[27-29]. The binder-printed layer was heated using an IR heat lamp for 25 seconds to remove excess water. Sequential slurry and binder deposition processes were repeated to build parts with the desired height. The completed parts were cured in an inert environment at 150 °C for 1 hour (Figure 4- 2c). The binder-free regions were redispersed[118] in an aqueous water bath (Figure 4- 2d) and the final parts were removed (Figure 4- 2e).

All samples consisted of 55 layers, each having a thickness of ~55 μm. Binder-free powder beds were cut to length using a 3" x 0.006" wafering blade (Buehler, Lake Bluff, IL). Notched samples were prepared using a using a 2" x 0.002" carbide saw (Robb Jack, Lincoln, CA). All samples were dried at 110°C for 1 hour and stored in a desiccator.

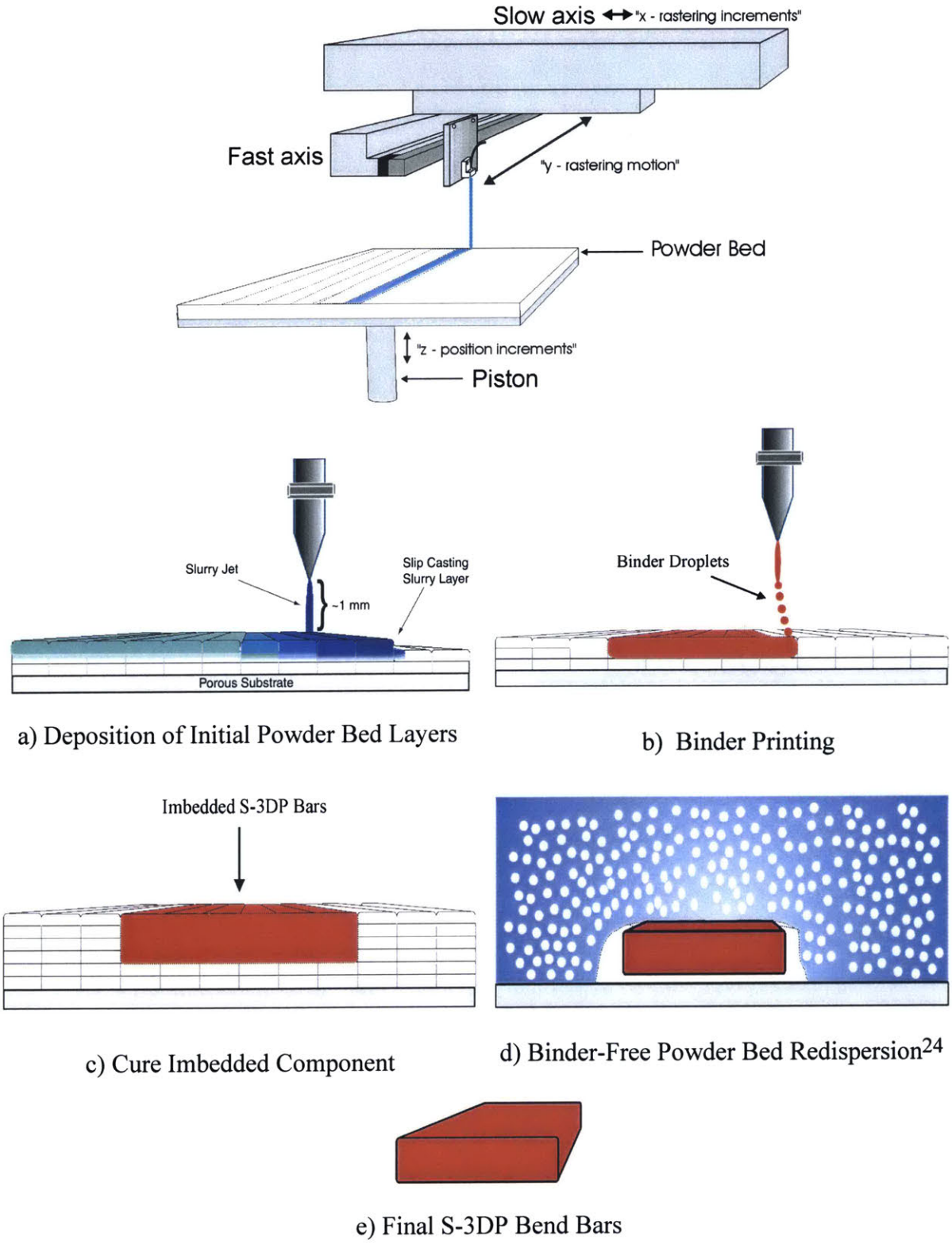

a) Deposition of Initial Powder Bed Layers

b) Binder Printing

c) Cure Imbedded Component

d) Binder-Free Powder Bed Redispersion[24]

e) Final S-3DP Bend Bars

Figure 4- 2: S-3DP Part Formation Process (*not to scale*).

4.3.7. Mechanical Characterization

ASTM Standard C 1161-94[57] was used in order to determine the flexural strength for 8 – 10 samples of each ceramic. Sample dimensions were l = 25 mm, w = 4 mm and h = 3 mm (Figure 4- 3b). The tests were performed using a 4-point bend configuration (Instron 4204, Canton, MA) with a 10 N or 20 N load cell. The specifications of the sample fixture are given in Figure 4- 3. The fracture toughness was measured according to ASTM Standard C 1421-99[58] using bend specimens with the previously outlined dimensions. Pre-crack notches (Figure 4- 3b and Figure 4- 3c) were placed across the 4 mm face of the powder bed samples. The notched faces were placed in tension during the measurement. Notch widths were 40 to 50 μm wide and lengths, c_n, were in the range of $0.12 \leq c_n/w \leq 0.30$. The fracture toughness, K_{IC}, was calculated according to Griffith's brittle fracture theory[50]:

$$K_{IC} = \sigma\sqrt{\pi c_n}\,, \tag{4.5}$$

where is σ the measured fracture strength.

4.4. Results

4.4.1. Glass Transition Characteristics of the PAA - Glycerol Polymer System

The normalized heat flow (W/g) is given in Figure 4- 4 as a function of sample temperature for the cured PAA films and the corresponding thermal properties are given in Table 4- 3. A significant endothermic event (ΔC_p = 0.45 $J*g^{-1}*C^{-1}$), characteristic of a glass transition, occurs between 113 °C and 124 °C for the PAA sample without glycerol. The glass transition is measured to be 118.3 °C, which is within the range of reported values of 106 °C[119] to 127 °C[120]. The change in the specific heat decreased from 0.43 $J*g^{-1}*C^{-1}$ down to 0.29 $J*g^{-1}*C^{-1}$ as the glycerol concentration increased from 0.1 wt.% to 5.0 wt.%. The glass transition of the PAA films increased with increasing

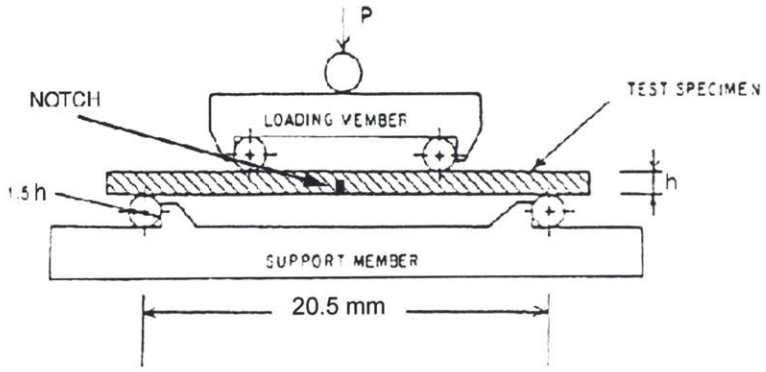

a)

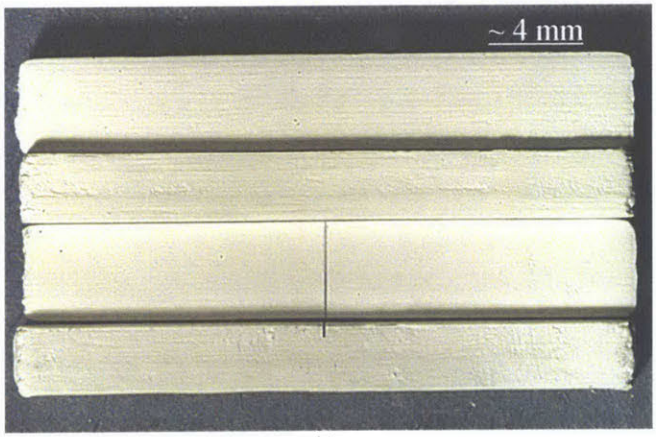

b)

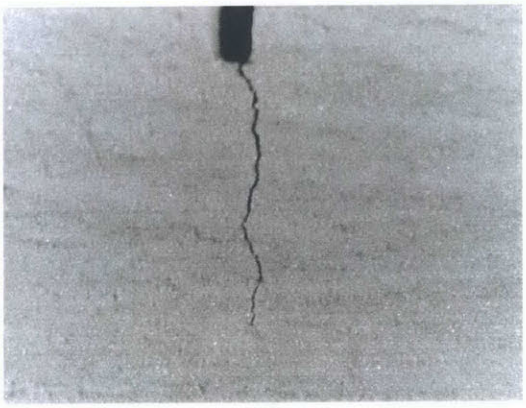

c)

Figure 4- 3: a) 4-Point Loading Fixture[25], b) Notched and Un-notched Al_2O_3 + 2.5 vol.% Bend Bars and c) Notch (~50 mm wide) and Sharp Crack Tip.

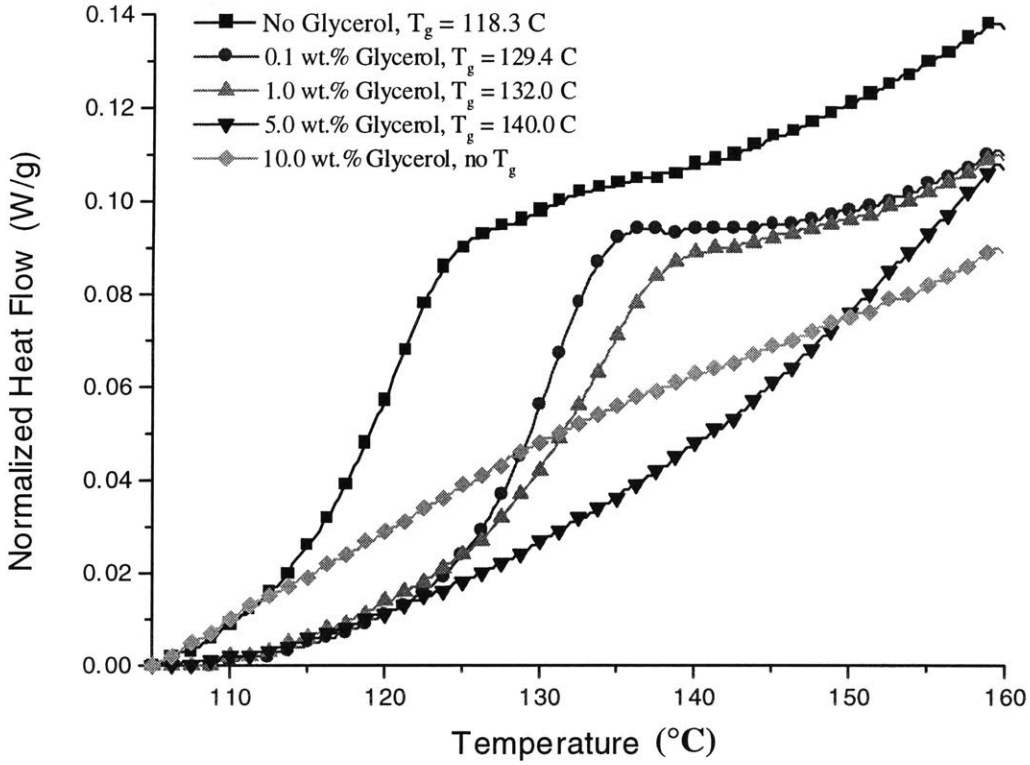

Figure 4- 4: Change in the Glass Transition Temperature (T_g) of PAA as a Function of Glycerol Concentration.

Table 4- 3: Differential Thermal Characteristics of PAA + Glycerol Samples after Heating at 150°C for 1 Hour.

Sample ID	ΔC_P ($J*g^{-1}*C^{-1}$)	T_g (°C)
PAA	0.45	118.3
PAA + 0.1 wt.% Glycerol	0.43	129.4
PAA + 1.0 wt.% Glycerol	0.38	132.0
PAA + 5.0 wt.% Glycerol	0.29	140.0
PAA + 10.0 wt.% Glycerol	Not Detected	Not Detected

glycerol concentration reaching a maximum value of 140.0 °C for the films containing 5.0 wt.% glycerol. No endothermic reactions were observed for the PAA samples containing 10.0 wt.% glycerol. The presence of a ceramic powder had little effect on the glass transition temperature of PAA containing 1.0 wt.% glycerol. Figure 4- 5 shows that the sample containing alumina powder had a lower T_g (131.1 °C) than the pure polymer sample (T_g = 132.0 °C) while silica powder increased the T_g to 132.5 °C.

4.4.2. The Iso-Electric Points of SiO_2, TiO_2, MR2 and Al_2O_3

The potentiometric characteristics of the silica, titania and alumina systems are given in Figure 4- 6. The zeta potential for the 1.0 vol.% silica slurry is slightly positive at pH 1.5 and decreases until reaching a minimum measured value of -43 mV at pH 9.0. The iso-electric point is observed at pH 2.3 and is in good agreement to the values reported by Flaningham[121] (pH 2.2 to 2.8). . The minimum potential for titania was -61 mV at pH 11.0 and a maximum zeta potential of 50 mV was measured at pH 2.9. An IEP of 5.6 was measured for the titania system, which is characteristic of a near-neutral or slightly-acidic oxide surface. This IEP is within the range of reported values of 4.7[122] and 6.2[123]. Similar zeta potential characteristics were observed for the MR2 system. The alumina system showed potentiometric behavior characteristic of a basic ceramic with an IEP of 10.4. The zeta potential ranged from 53 mV at pH 4 to –28 mV at pH 12.

4.4.3. The Adsorption of PAA onto SiO_2, TiO_2 and Al_2O_3

The surface adsorption of PAA onto alumina, titania and silica is given in Figure 4- 7. PAA adsorption onto Al_2O_3 was characteristic of a high affinity, type I adsorption isotherm with monolayer coverage at ~ 1.0 mg/m^2. The adsorption onto TiO_2 indicates a much weaker affinity, with adsorbed concentration rising much more slowly. There does not appear to be any appreciable adsorption of PAA onto SiO_2.

4.4.4. The Fracture Properties of SiO_2, TiO_2, Al_2O_3 and MR2 Binder-Free Bars

The fracture characteristics of binder-free SiO_2, TiO_2, Al_2O_3 and MR2 bend bars are summarized in Table 4- 4. The MR2 system had the highest strength at 1.44 MPa with a modulus of 311 MPa. The binder-free alumina samples proved to have the highest

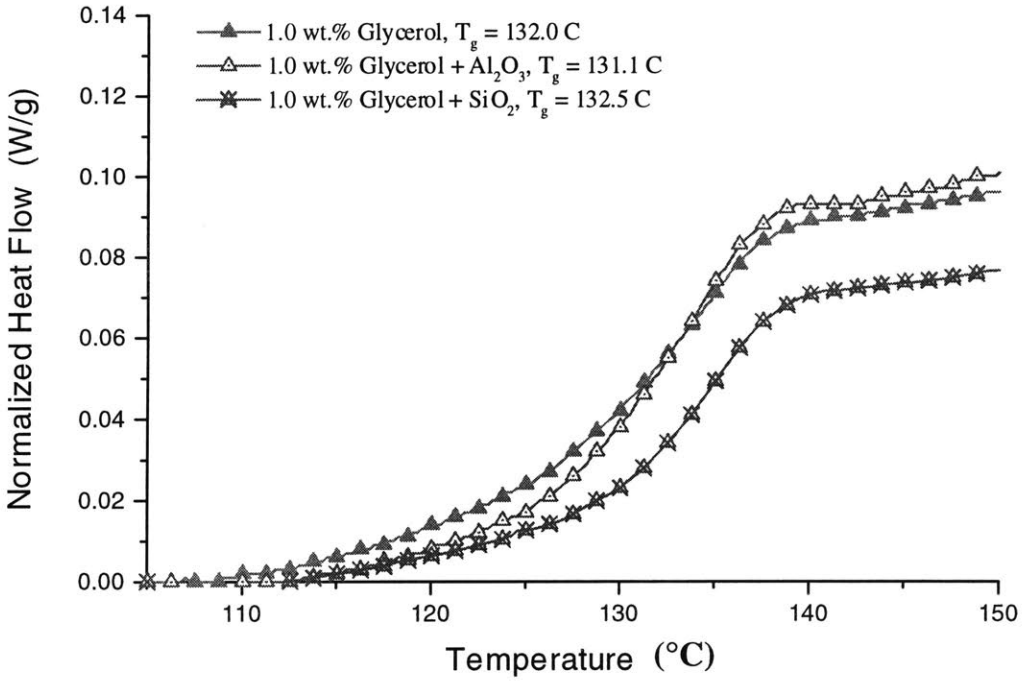

Figure 4- 5: The Effect of the Ceramic on the Glass Transition Temperature of PAA + 1.0 wt.% Glycerol.

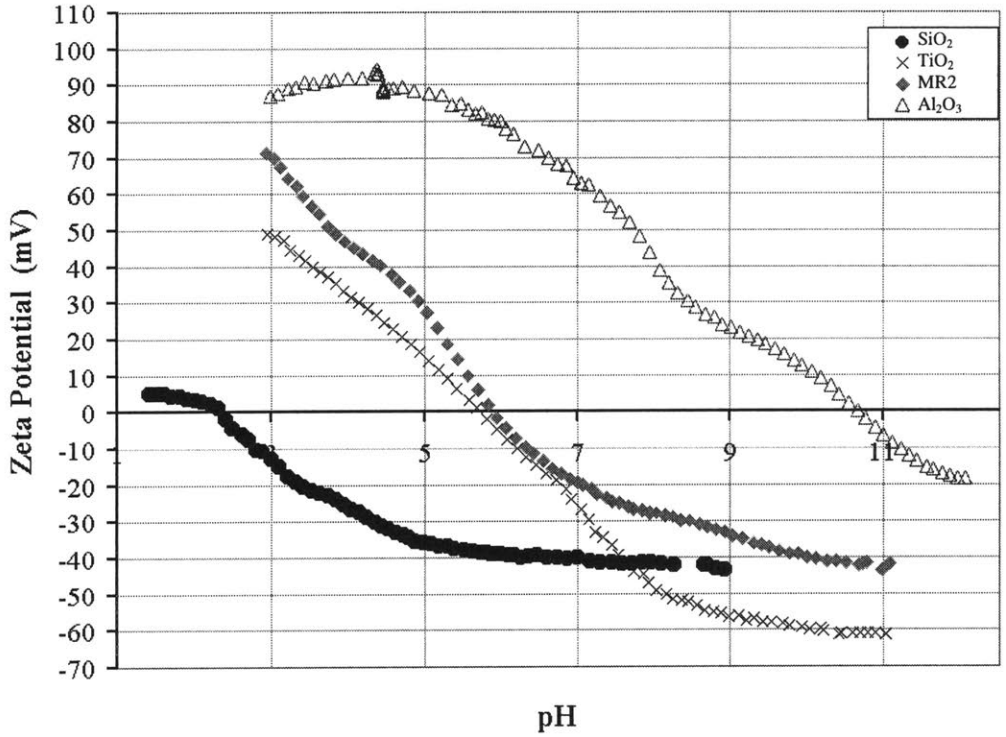

Figure 4- 6: Potentiometric Behavior of SiO_2 (IEP = 2.3), TiO_2 (IEP = 5.6), MR2 (IEP = 6.0) and Al_2O_3 (IEP = 10.4).

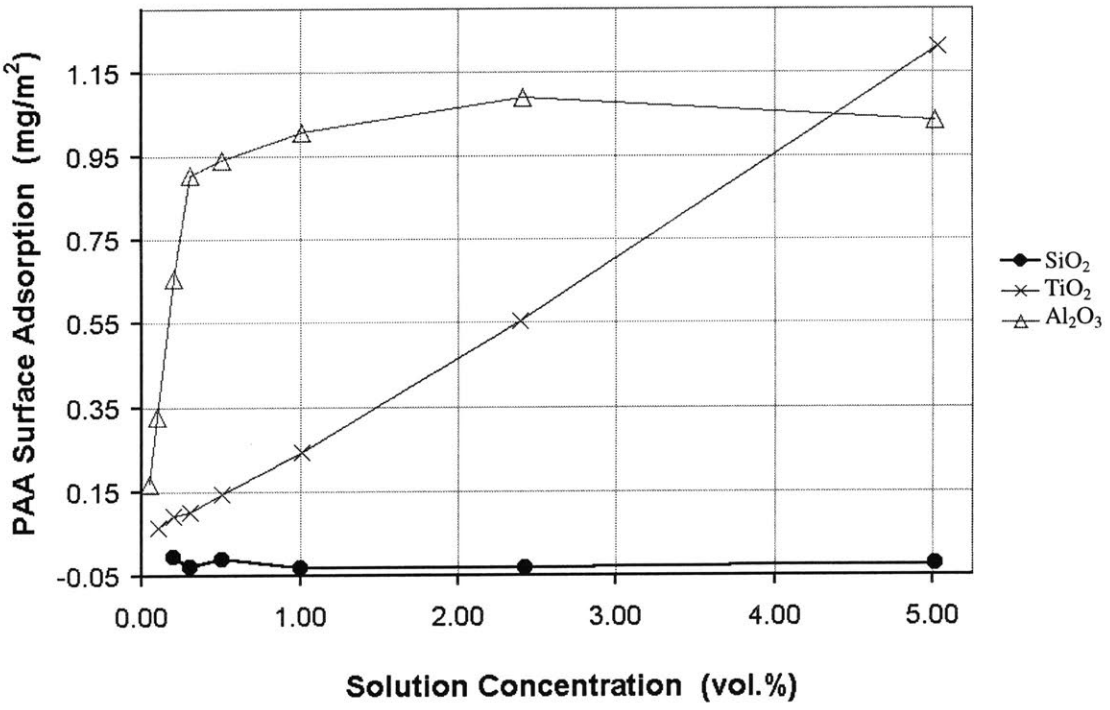

Figure 4- 7: Surface Adsorption of PAA onto SiO_2, TiO_2 and Al_2O_3.[18]

fracture stress and modulus for the simple oxide systems with values of 0.34 MPa and 186 MPa, respectively. The silica and titania samples demonstrated similar fracture stresses, 0.16 MPa and 0.18 MPa, while the elastic modulus of the titania system was approximately twice that of the binder-free silica bars (177 MPa vs. 82 MPa). Binder-free fracture toughnesses obtained from the notched fracture tests (Eq. 5.5) are also summarized in Table 4- 4. Similar to the fracture stress measurements, the alumina compacts proved to have the highest fracture resistance ($7.2*10^{-3}$ MPa*$m^{1/2}$) with respect to the simple oxide systems, while the lowest values were calculated for silica ($2.8*10^{-3}$ MPa*$m^{1/2}$). The calculated fracture toughness for MR2 samples was the highest, with an average value of $2.18*10^{-2}$ MPa*$m^{1/2}$. A more detailed description on the mechanical properties of binder-free "agglomerates" is given in Chapter 3.

4.4.5. Characteristics of Redispersed-Saturated Green Parts

All of the imbedded green bars (2.5 vol.% PAA + 10 wt.% glycerol) were successfully removed from binder-free powder bed using the redispersion technique outlined in Chapter Three. The ability to retrieve the parts containing the PAA-glycerol system in an aqueous bath verifies that the polymer forms an insoluble, bonded network after curing at 150 °C for 1 hour. The mechanical integrity was also tested during the redispersion process. It has been shown that positive osmotic pressures of approximately 0.4 to 0.6 MPa are applied to the green components, as well as the binder-free powder bed, during the redispersion process[118]. The fact that all of the green samples remained intact during the redispersion process suggests that their cohesive strength is greater than the redispersive forces. This was confirmed by measuring the fracture strengths (4-pt bend) of the green SiO_2, TiO_2, Al_2O_3 and MR2 bend bars in a "wet" state. All of the wet strengths are greater than 0.6 MPa. The lowest value of 0.7 MPa was measured for the silica samples, which is a factor of 5 larger than the binder-free SiO_2 samples. The wet strength for the titania and MR2 samples were 1.4 MPa and 3.6 MPa, respectively, while the saturated alumina bars were the strongest with a strength of 5.6 MPa.

Table 4- 4: Fracture Properties for Binder-Free SiO_2, TiO_2, Al_2O_3 and MR2.

Ceramic	Green Density (%)	Stress (MPa)	Modulus (MPa)	K_{IC} ($MPa*m^{1/2}$)
SiO_2	52	0.157 ± 0.017	81.6 ± 13.8	$2.8*10^{-3} \pm 0.3*10^{-3}$
TiO_2	48	0.177 ± 0.012	177 ± 20.0	$3.5*10^{-3} \pm 0.9*10^{-3}$
Al_2O_3	53	0.340 ± 0.022	186 ± 29.6	$7.2*10^{-3} \pm 1.1*10^{-3}$
MR2	49	1.44 ± 0.054	311 ± 32.3	$2.18*10^{-2} \pm 2.2*10^{-3}$

Table 4- 5: Fracture Properties for SiO_2, TiO_2, Al_2O_3 and MR2 Samples Containing 2.5 vol.% PAA (Ceramics Solids Basis).

Ceramic	Packing Density (%)	Fracture Stress (MPa)	Modulus (GPa)	K_{IC} ($MPa*m^{1/2}$)
SiO_2	52	1.15 ± 0.12	0.15 ± 0.03	$4.4*10^{-2} \pm 0.5*10^{-2}$
TiO_2	48	2.08 ± 0.06	0.50 ± 0.08	$4.3*10^{-2} \pm 0.3*10^{-2}$
Al_2O_3	53	7.65 ± 0.62	1.94 ± 0.24	$1.0*10^{-1} \pm 3.1*10^{-2}$
MR2	49	9.03 ± 0.88	1.07 ± 0.19	$2.2*10^{-1} \pm 0.3*10^{-2}$

4.4.6. Mechanical Properties of Dry Green Bodies Containing 2.5 vol.% PAA

The mechanical properties of dry green bars were significantly enhanced by the presence of 2.5 vol.% PAA and are summarized in Table 4- 5. The PAA binder increased the strength of the alumina samples by a factor of 25, while the elastic modulus increased from 0.18 GPa to 1.9 GPa. The MR2 system proved to have the highest strength at 9.03 MPa with a modulus of 1.07 GPa. The PAA was less effective for titania green bodies, which had an average fracture stress of 2.08 MPa and modulus of 0.50 GPa. The silica bars proved to have the weakest mechanical properties; however, the PAA binder increased the fracture strength of the SiO_2 bodies by a factor of eight. The green fracture toughnesses (Table 4- 5) were also dramatically improved by PAA. The fracture toughness of the alumina bars increased by a factor of 14 to 0.1 $MPa*m^{1/2}$, while the fracture resistances for the titania and silica samples were determined to be $4.3*10^{-2}$ $MPa*m^{1/2}$ and $4.3*10^{-2}$ $MPa*m^{1/2}$, respectively. The average calculated fracture toughness for the MR2 samples was the highest with an average value of $2.2*10^{-1}$ $MPa*m^{1/2}$, which is an order of magnitude larger than the binder-free value.

4.5. Discussion

The fracture characteristics of the ceramic green bodies are influenced by the mechanical properties of the acrylic–based binder. The nature of these properties, i.e., brittle versus plastic, is dependent on the glass transition temperature of the polymer. Figure 4- 4 shows that the T_g of PAA is above room temperature and that increasing the glycerol concentration in the cured PAA films increases the glass transition temperature of the polymer. The T_g increases due to the formation of a crosslinked network that is created by an esterification reaction between the polyacrylic acid and glycerol under acidic conditions (pH < 7) at 150 °C[113,124,125] (Figure 4- 8). Increasing the concentration of the glycerol forces the esterification reaction forward and yields an increase in the ester crosslink density.[126] An increasing crosslink density reduces the degree of mobility that is associated with each unreacted side group, which results in an increase in the glass transition temperature[115,127,128].

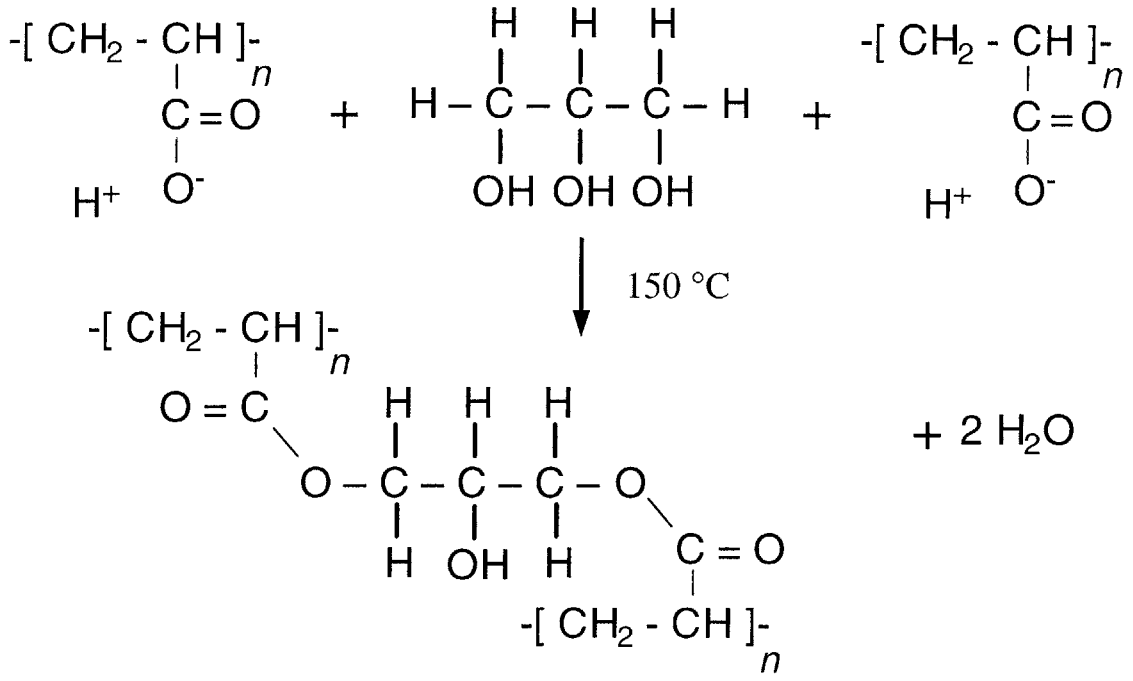

Figure 4- 8: Formation of Ester Crosslinks in the PAA-Glycerol System.[36]

The crosslink density of polymer networks can be described by the number-average molecular weight between crosslinks, M_C^N, which has been empirically estimated by Nielson to be:

$$M_C^N = 3.9*10^4 \frac{g \cdot {}^\circ C}{mol} * (T_g - T_g^o)^{-1}, \qquad (4.6)$$

where T_g is the glass transition of the crosslinked polymer and T_g^o is the glass transition of the uncrosslinked polymer. This relationship has been used to describe crosslinked polymer systems, including crosslinked polyacrylic acid[129]. According to Neilson's relationship, the molecular weight of the crosslinked units in the PAA films containing 0.1 wt.%, 1.0 wt.% and 5.0 wt.% glycerol are 3500 g/mole, 2800 g/mole and 1700 g/mole, respectively. The presence of a high crosslink density is essential in order to "de-sensitize" the mechanical properties of the PAA binder to humid environments since water plasticizes acrylic-based polymers that are not crosslinked. Rualt et al.[127] have studied the effects of the crosslink density of PAA on the glass transition at various moisture contents. The change in the glass transition of ester-crosslinked PAA polymers (M_C^N = 3000 g/mole) with low moisture content (~ 1 wt.%) is only ~8°C.

The presence of the ceramic has little effect on the glass transition of crosslinked PAA polymers. A slight increased in the glass transition (Figure 4- 5) was observed due to the presence of silica, which indicates that the crosslink density increases. Silica is shown to have an acidic surface with an IEP of 2.3 (Figure 4- 6). An increase in the crosslink density is reasonable since the esterification reaction is catalyzed in acid. The glass transition temperature is slightly depressed by the presence of alumina. Alumina has a basic surface and the esterification reaction is expected to slow down. The surface-active groups are not freely distributed; hence, the ceramic surface effects are negligible with respect to the formation process of the continuous polymer network. Therefore, it is concluded that the crosslinked PAA + 10 wt.% glycerol binder is a brittle material under ambient conditions regardless of the ceramic system.

The PAA-glycerol binder system improves the fracture properties for all of the ceramic materials studied. The strengths of the SiO_2, TiO_2, MR2 and Al_2O_3 green bodies

increase by factors of 8, 11, 15 and 23, respectively, due to 2.5 vol.% crosslinked PAA. Undoubtedly, the efficacy of crosslinked PAA as a binder is dependent upon the ceramic system. The adsorption of PAA onto various oxide surfaces has been well documented[109,112]. Strong adsorption occurs for positively charged surfaces and the surface affinity reduces as the positive surface charge decreases[111], and desorption has been observed for negatively charged surfaces[110]. The adsorption process is described using acid-base base phenomena that charge the oxide surface and the polymer. Charged oxides surfaces are controlled by the $(M)OH_2^+$, (M)OH and $(M)O^-$ species depending on the pH. Adsorption occurs due to electrostatic interactions between positively–charged surfaces, i.e., $(M)OH_2^+$, and deprotonated PAA molecules. Adsorption is also enhanced due to the formation of hydrogen bonds between the carboxyl groups of PAA and $(M)OH_2^+$ groups present at the oxide surface.[130]

Adsorption of the PAA polymer is shown to vary dramatically with respect to the ceramic powders used for S-3DP processing.[18] The 2.4 vol.% PAA solution used for part fabrication had a pH value of 2.1. This processing condition yields PAA surface adsorptions of ~0.0 $mg*m^{-2}$, 0.6 $mg*m^{-2}$ and 1.1 $mg*m^{-2}$ for the SiO_2, TiO_2 and Al_2O_3 powders. Figure 4- 6 shows that Al_2O_3, MR2 and TiO_2 are positively charged at pH values less than 10.4, 6.0 and 5.6, respectively, while the surface of SiO_2 is negatively charged down to pH 2.3. Therefore, it is expected that the adsorption is highest for Al_2O_3 and very low for SiO_2. Moreover, the interaction should be strongest for Al_2O_3 since it has the highest IEP, i.e., largest positive surface charge, at S-3DP processing conditions. This is confirmed in Figure 4- 9, which shows a positive correlation between the relative increase in green strength due to PAA and the iso-electric point of the ceramic systems. Nevertheless, it is important to emphasize that the presence of the binder increased the strength of the SiO_2 body by nearly an order of magnitude, even though no adsorption occurred. The increase in strength is likely the result of some physisorption of PAA onto the SiO_2 surface.

The PAA binder also had a dramatic effect on the fracture resistance of the green body. The fracture toughnesses of the porous ceramic bars increased by at least an

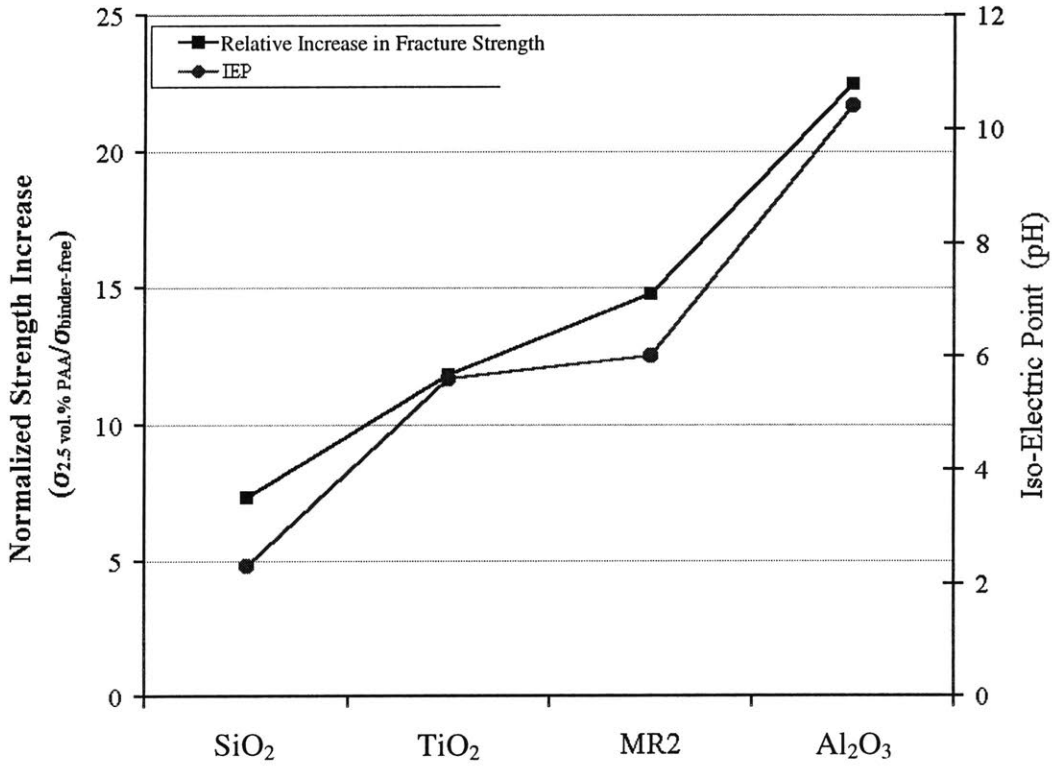

Figure 4- 9: Relative Increase in the Strength of the Green Bodies and the Iso-Electric Points of the Ceramic Materials.

order of magnitude (Table 4- 4 and Table 4- 5) due to presence of the PAA binder. Griffith's theory of brittle fracture was used to determine the toughnesses of the ceramic bodies. Brittle fracture was confirmed for the Al_2O_3 + PAA system by examining the fracture strength as a function of notch size, c_n, (Figure 4- 10). The empirical relationship is:

$$\sigma = 0.07 * c_n^{-0.48}, \tag{4.7}$$

with a power law that is close to the theoretical relationship proposed by Griffith (Eq. 4.5). The empirical constant in Eq. 4.7 suggests that the fracture toughness is ~0.12 MPa*$m^{-1/2}$, which is in good agreement with the toughness value calculated using Griffith's theory.

Figure 4- 11 shows representative loading profiles for each ceramic system. The stress-strain behavior of the Al_2O_3 samples is characteristic of a linear elastic body (Figure 4- 11a). The MR2 and TiO_2 samples have very similar characteristics and are nearly elastic with some plastic deformation present (Figure 4- 11b and Figure 4- 11c). The SiO_2 bend bars show a relatively larger positive deviation from ideal brittle behavior (Figure 4- 11d), which suggests that an energy absorption mechanism is occurring during deformation.

The transition from brittle fracture in the case of Al_2O_3 + PAA to a more "ductile" failure mechanism for SiO_2 + PAA must result from different fracture mechanisms since the binder is brittle in both cases. Two possible failure mechanisms are shown in Figure 4- 1b and Figure 4- 1c. The contrasting behaviors can be realized by considering the differences in PAA's affinity for the respective ceramics surfaces, i.e., Al_2O_3's basic surface (IEP = 10.4) vs. SiO_2's acid surface (IEP = 2.3). The crosslinked PAA binder is intimately bonded with the surface of Al_2O_3 and according to Eq. 4.4 the cohesive strength of the binder phase is 54 MPa. Ruckenstein and Liang[131] have reported the tensile strength of ester-crosslinked PAA polymers to be on the order of 50 MPa. Therefore, brittle fracture likely occurs through the polymer phase, as shown in Figure 4- 1b. Essentially no surface chemisorption occurs in the case of SiO_2, and the calculated strength of the binder in the SiO_2 samples is 7 MPa. This is far

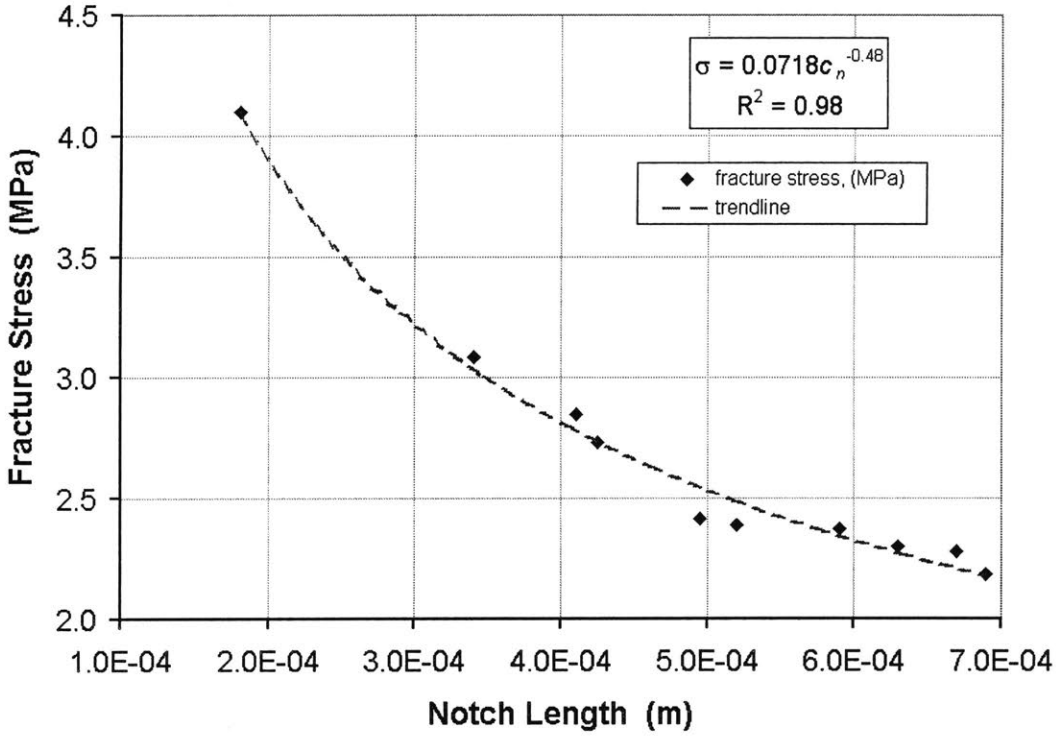

Figure 4- 10: Fracture Strength for Al_2O_3 + PAA as a Function of Notch Size.

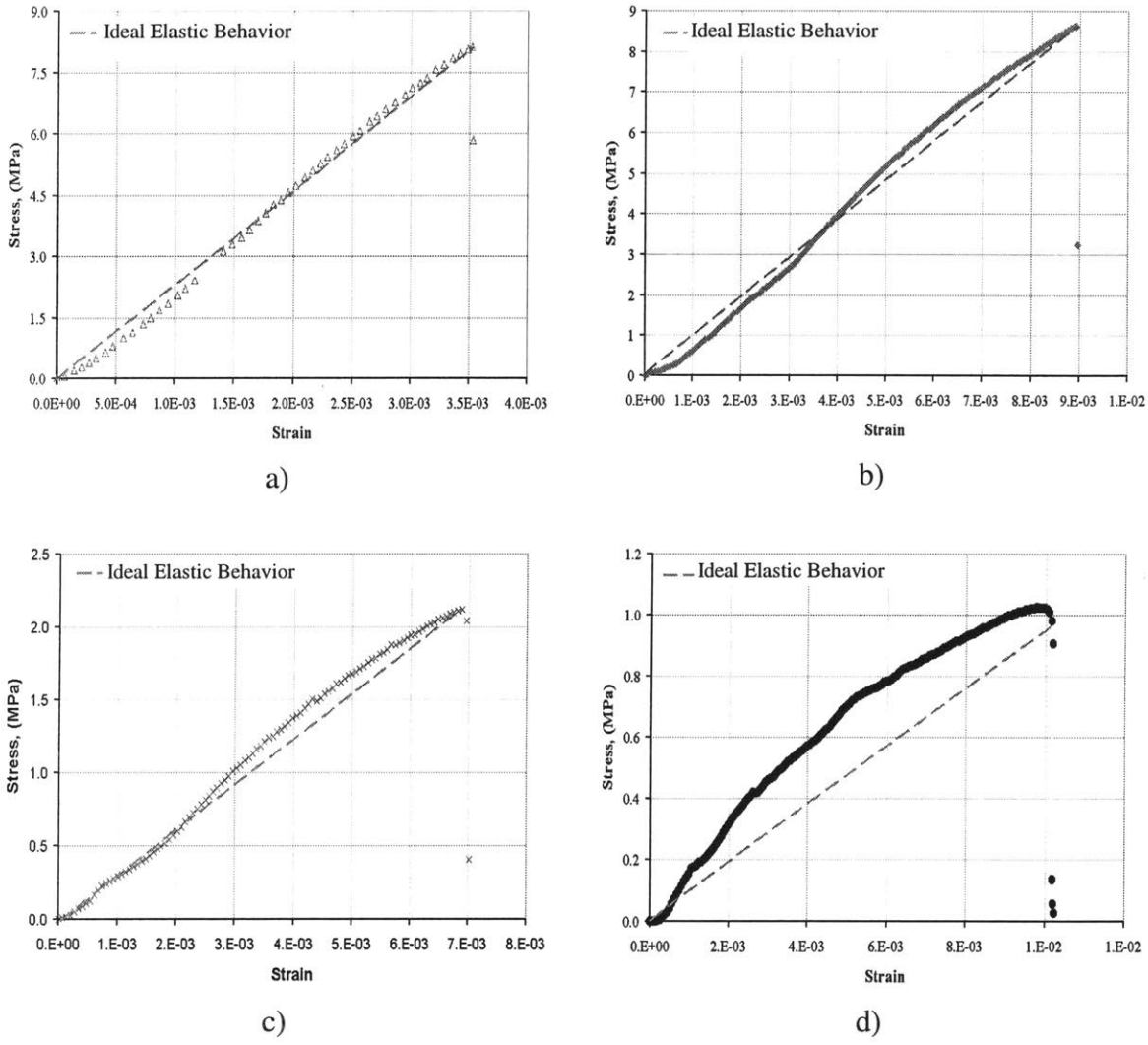

Figure 4- 11: Stress-Strain Behavior for a) Al_2O_3, b) MR2, c) TiO_2 and d) SiO_2.

below the tensile strength of crosslinked PAA. Failure is expected to occur at the ceramic-polymer interface since this offers a path of lower resistance (Figure 4- 1c). The particles "detach" from the continuous polymer phase, allowing particles to rearrange and slide against the polymer interface. This mechanical interaction toughens the green body by producing heat and absorbing energy. This theory is analogous to fracture mechanisms acting within fiber re-enforced composites in which the resistance to fracture is dictated by the bond strength at the fiber-composite interface.[132]

The calculated strength (Eq. 4.4) of the PAA binder in the SiO_2 system is likely a result of physisorption of the polymer onto the surface of SiO_2. The physical attraction due to van der Waals interactions is computed using Hamaker's calculations[49] for the attractive force per unit area between two semi-infinite bodies:

$$\frac{F}{A} = \sigma = \frac{A}{4\pi h^3}, \tag{4.8}$$

where h is the separation distance between the polymer and the ceramic and A is the Hamaker constant for the polymer-ceramic system (~$9*10^{-20}$ J). The calculated binder strength due to van der Waals interaction as a function of separation distance is given in Figure 4- 12. The cohesive strength of the binder-SiO_2 due to van der Waals interactions (Eq. 4.8) intersects the calculated binder strength according to Onoda's strength model (Eq. 4.4) at approximately 1 nm. This suggests that the binder strength in the SiO_2 may result from physisorption.

4.6. Conclusions

Various green ceramics (SiO_2, TiO_2, Al_2O_3 and MR2) with low binder concentrations have been studied in order to determine the binding mechanisms as a function of ceramic surface chemistry. Fracture specimens were formed using a solid freeform fabrication technique which provides a means for the formation of green bodies with uniform density and composition. Green bodies were formed using a soluble polyacrylic acid (MW = 60,000) and glycerol, which were crosslinked forming a brittle polymer phase. Adsorption and potentiometric studies show that the affinity of

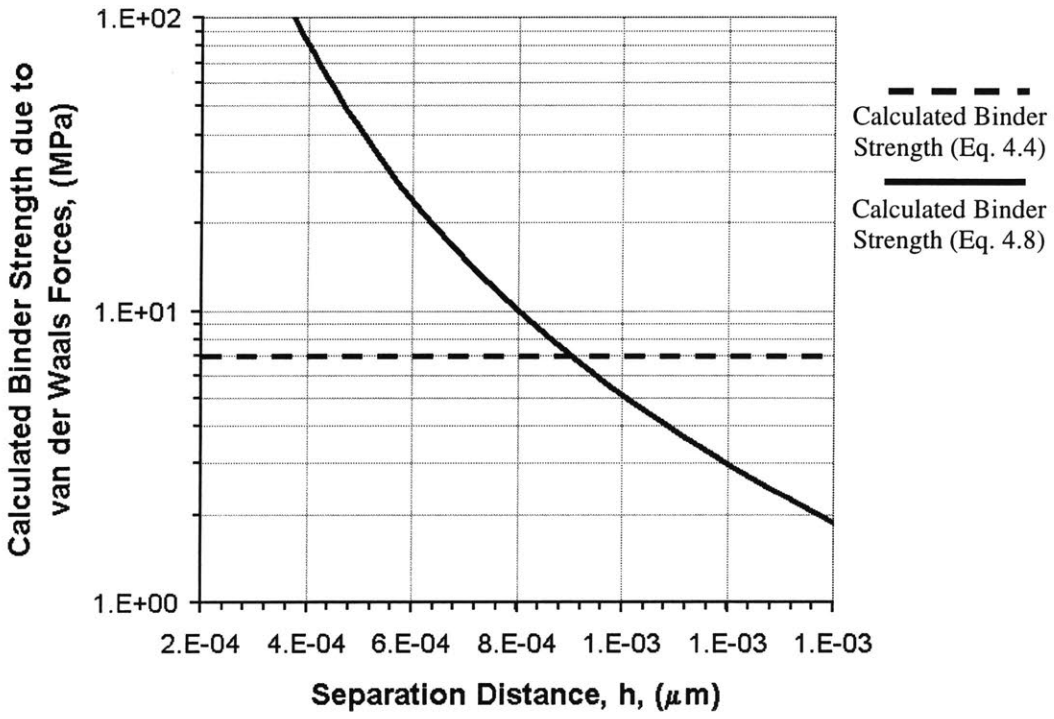

Figure 4- 12: Calculated "Binder Strength" for the PAA-SiO_2 System as a Function of Separation Distance vs. Calculated Binder Strength According to Onoda's Theory (Eq. 4.4).

PAA-based binder for the ceramic surface decreases as the iso-electric point of the ceramic decreases. Higher relative green strengths resulted from the adhesion of the binder to the surface of the ceramic particles. The addition of 2.5 vol.% binder increased the strength of silica (IEP = 2.3) by a factor of 8 while the strength of alumina (IEP = 10.4) increased by a factor of 25. The binder also improved the toughness of the ceramic bodies by an order of magnitude, with silica representing the largest relative increase. Silica bodies are shown to have some plastic deformation, which is likely a result of cracks forming at the particle-polymer interface.

Chapter Five

The Formation of S-3DP Advanced Ceramic Components

5.1. Introduction

The previous three chapters have described in detail the cohesive strength of binder-free S-3DP powder beds, the chemically–enhanced redispersion of the binder-free powder bed and the strength of S-3DP green components. Incorporation of these principles serves as the fundamental theory for part retrieval. The newly developed part retrieval process is an essential tool that improves the shape capabilities as well as the reliability of the S-3DP process. A variety complex–shaped MR2 components containing 2.5 vol.% crosslinked PAA (Chapter Four) have been formed. The S-3DP fabrication process is outlined using the MR2 system and their resulting properties are presented in the following sections.

5.2. Part Retrieval

S-3DP components are removed from the powder bed by redispersing the surrounding binder-free powder bed regions. Chapter Three has proven that powder bed redispersion is achieved by developing osmotic pressures that exceed the fracture strength of the powder bed by forming a polymer solution within its pore structure. The osmotic pressure gradient forces water into the porous structure and creates a tensile stress on the particle network with magnitudes as high as 0.6 MPa. The cohesive strength of the printed component must be greater than these osmotically induced stresses in order that the printed components retain their geometries during the redispersion process. Chapter Four has demonstrated that the fracture strength of saturated printed components containing 2.5 vol.% crosslinked PAA exceed the induced osmotic stresses. Therefore, the fundamental requirements to achieving part retrieval is:

$$\sigma_{\text{Powder Bed}}^{Binder-Free} < \pi_{\text{Osmotic Pressure}} < \sigma_{\text{S-3DP "wet" Part}}^{2.5vol.\%PAA}, \qquad (5.1)$$

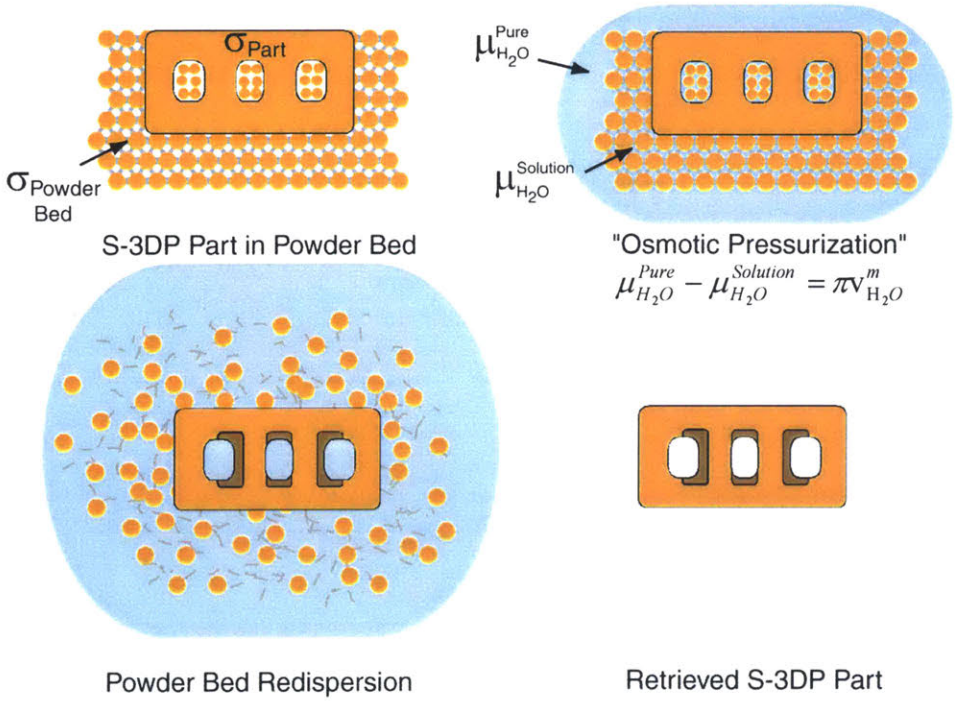

Figure 5- 1: Part Retrieval due to Osmotic Redispersion.

Table 5- 1: Part Retrieval Principle Properties (Eq. 5.1).

Ceramic	$\sigma_{\text{Powder Bed}}$ (MPa)	π (MPa)	σ_{Part} (MPa)
TiO_2	0.2	0.6	1.4
SiO_2	0.2	0.6	0.7
Al_2O_3	0.3	0.6	5.6
MR2	0.6*	0.5	3.6

*see Sections 2.7 and 3.6

which is represented by the part retrieval scheme shown in Figure 5-1. These three principles for part retrieval have been proven for a wide range of model oxide systems (see Table 5- 1) and have been successfully applied to the MR2 system to form components with complex geometries.

5.3. The Fabrication of S-3DP MR2 Having Complex Geometries

5.3.1. Printing Process

The S-3DP printing procedure has been previously outlined in Chapter One and is described in detail by Grau[37]. MR2 parts were formed using the Alpha 3DP machine, which is equipped with printhead diagnostics that improve the accuracy of the printed binder droplets. Components containing 2.5 vol.% crosslinked PAA were printed using a solution of 2.4 vol.% PAA + 10 wt.% glycerol (PAA basis) as the binder, which was readily integrated into the current printhead technology. Figure 5- 2 shows a schematic layout of the printed components imbedded within the powder bed. Upon completion, the parts were cured at 150°C for 1 hour in argon to crosslink the PAA + glycerol system (Section 4.5) such that the binder does not dissolve during the water-based part retrieval process.

5.3.2. Elimination of Differential Slip Casting

The differential slip casting effects of the binder system on part formation in the S-3DP process has been outlined in Section 1.4.1. The crosslinked PAA binder system has essentially eliminated defects due to differential slip casting. The high strength of the PAA binder has made it possible to decrease the binder concentration by a factor of 4 (10 vol.% Joncryl to 2.5 vol.% crosslinked PAA). Grau[37] has defined the ideal ratio of the cosines of the contact angles of the slurry solvent on the binder and on the ceramic powder that will give equal slip casting rates on the two regions as a function of binder content (see Figure 5- 3). Figure 5- 4 shows the wetting properties as a function of alcohol content in the slurry solvent, with the ideal value for 2.5 vol.% binder represented by the horizontal line. Differential slip casting is minimized by choosing a slurry solvent composition on or near this line (see Appendix A). S-3DP components were produced using slurries with solvents composed of 50 vol.% water and

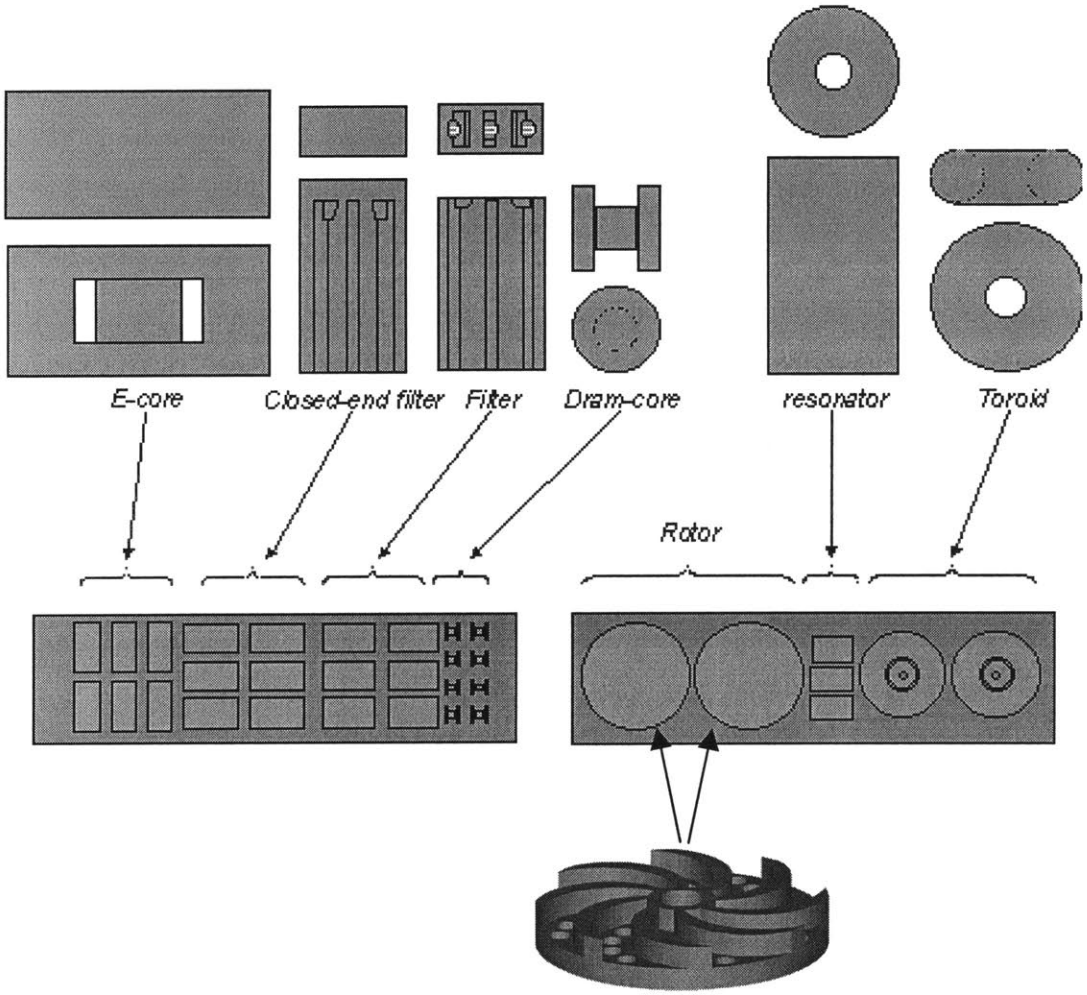

Figure 5- 2: Layout of S-3DP Components Imbedded within the Powder Bed.

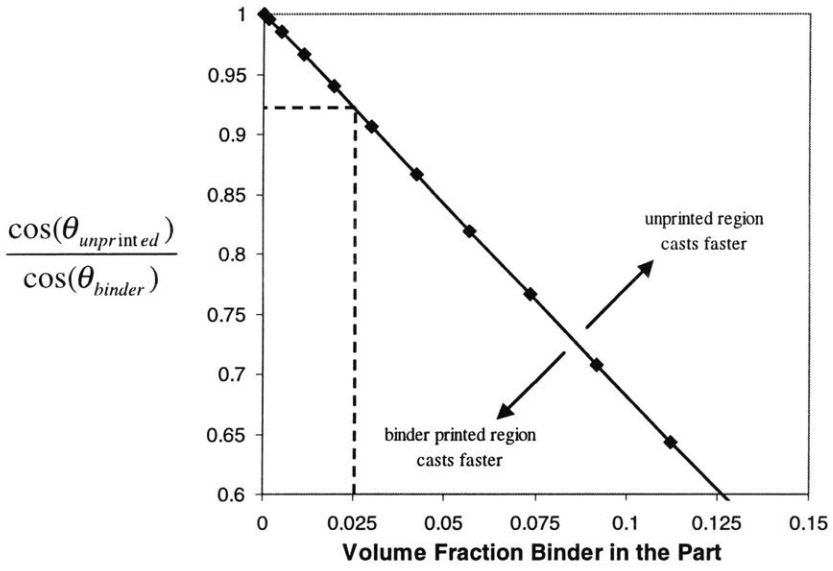

Figure 5- 3: Model of Differential Slip Casting Rates.[37]

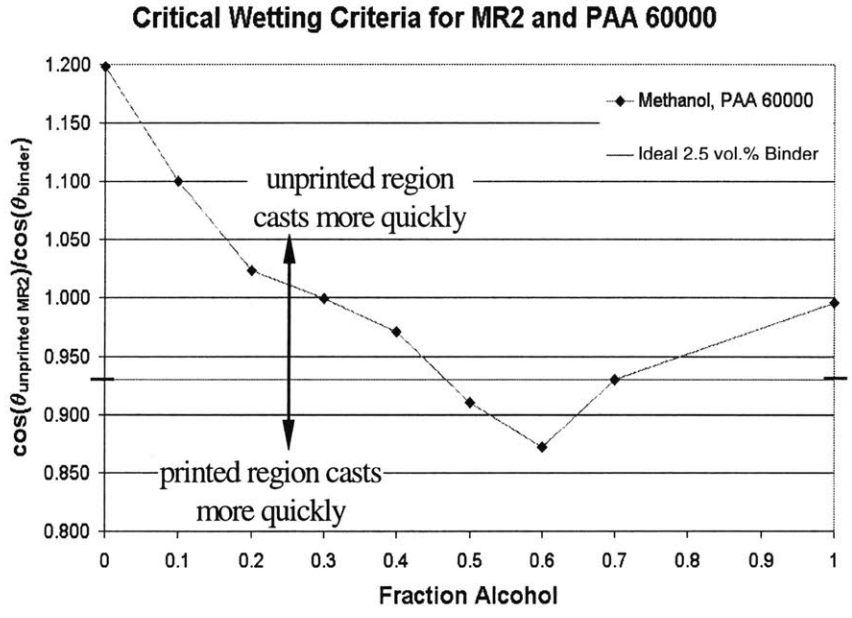

Figure 5- 4: Effect of Slurry Solvent Chemistry on Wetting Behavior.[39]

50 vol.% methanol. The resulting powder beds show a dramatic improvement (Figure 5- 9a vs. Figure 1- 11) with essentially no differential casting defects present, which allows components of essentially any height to be manufactured.

5.3.3. Effects of Binder Curing on Redispersion

It is has been established that the presence of 5.0 vol.^{PORE}% PEG 400 within MR2 powder beds is necessary in order to redisperse binder-free MR2 powder beds. A challenging aspect of slurry-based 3DP is designing the process such that redispersion is achieved after thermally curing the binder. It is well known that PEG degrades in the presence of oxygen[133,134]. One possible degradation mechanism is shown in Figure 5- 5a in which heat can act as an initiator producing free radicals that degrade PEG to carbonyl containing species.

Thermogravimetric analysis (TGA) (Figure 5- 5a) shows that PEG 400 losses 18 % of its mass when heated in air at 150 °C, i.e., the binder curing temperature. Therefore, powder bed redispersion is adversely affected by thermally curing the PAA binder in air (Figure 5- 5b) since osmotic forces are reduced due to the decrease in PEG concentration (Section 3.6). Two approaches were used to minimize the degradation of PEG during the binder-curing process. Butylated hydroxy toluene (BHT, Aldrich), a common anti-oxidant, was added (1000 ppm)[135] to PEG 400. A second step was to cure the binder in an inert atmosphere. TGA studies were performed at 150°C for one hour in order to determine the stability of PEG and PEG + BHT in air and in argon. The results are given in Figure 5- 6a. The addition of BHT slightly decreased the thermal degradation of PEG by reducing the mass loss by 4 wt.%. The PEG samples that were heated in argon show a drastic improvement in thermal stability with a corresponding mass loss of 3 wt.% while PEG + BHT in argon was the most stable. These conditions have restored the redispersibility of the powder bed after curing. Figure 5- 6b shows that MR2 powder beds (containing 5.0 vol.^{PORE}% PEG 400) cured in argon completely redisperse (redispersed mass loss = 100 wt.%) in comparison to those cured in air (redispersed mass loss = 5 wt.%).

The atmosphere is not the only parameter that must be controlled during the curing process. Redispersion is also very sensitive to the binder curing temperature since the PEG

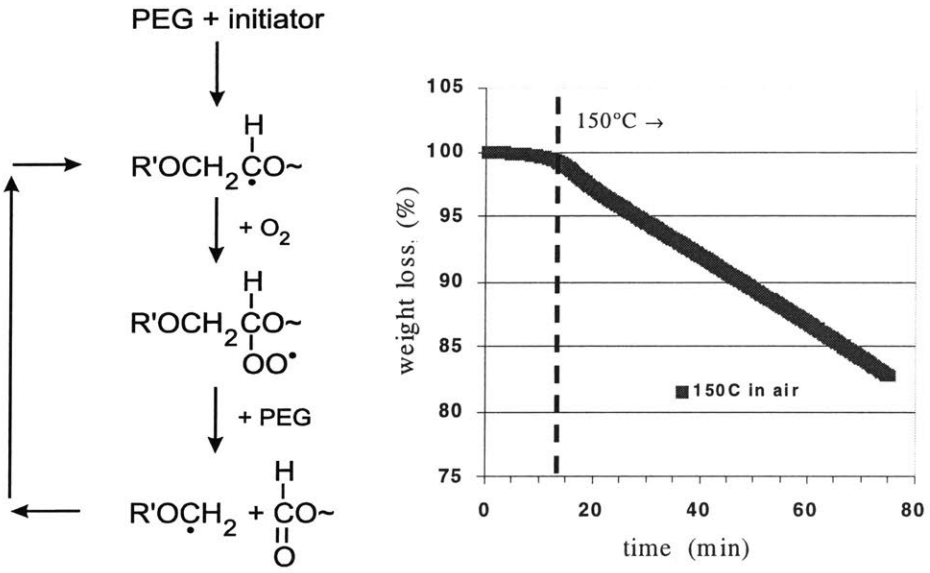

a)

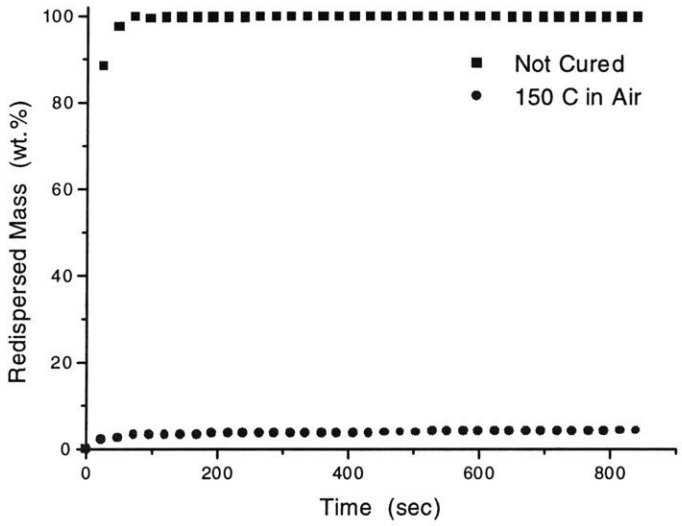

Powder Beds Containing 5.0 vol.^{PORE}% PEG 400

b)

Figure 5- 5: a) Oxidative Degradation of Polyethylene Glycol and b) Poor MR2 Redispersion due to PEG Degradation during the Binder Curing Procedure.

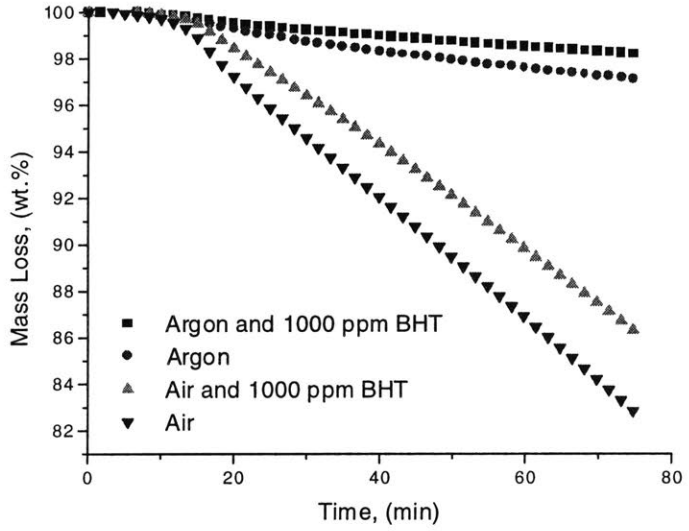

a)

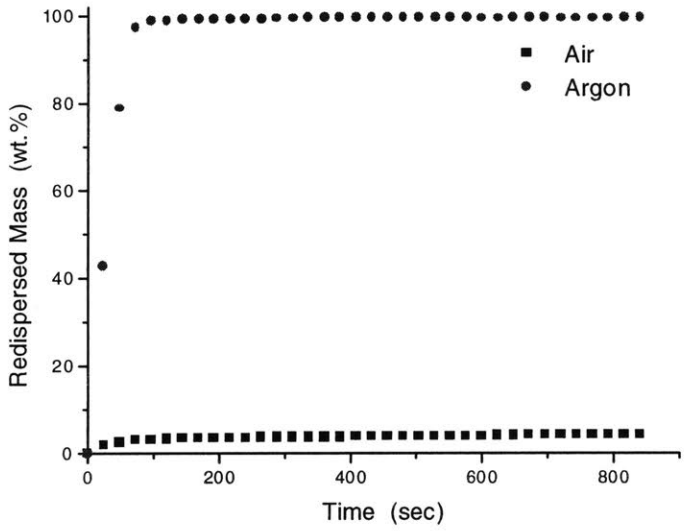

Powder Beds Containing 5.0 vol.^{PORE}% PEG 400

b)

Figure 5- 6: a) Thermogravimetric Analysis of PEG 400 and the Effects of BHT and Curing Atmosphere and the b) Influence of Atmosphere on the Redispersion of MR2 Powder Beds.

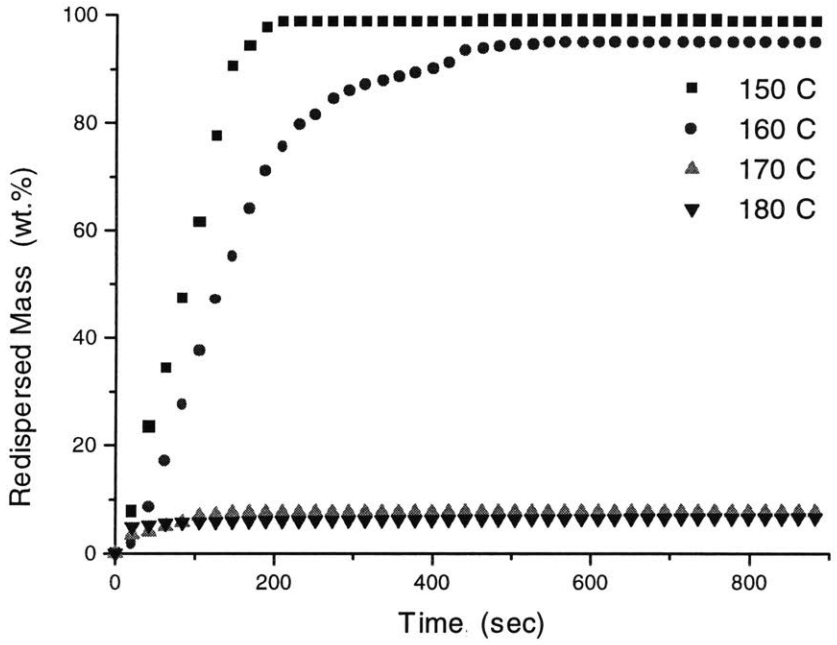

Powder Beds Containing 5.0 vol.^{PORE}% PEG 400

Figure 5- 7: Effect of the Curing Temperature on the Redispersion of MR2 Powder Beds.

degradation process is thermally activated. The redispersed mass of MR2 powder beds (containing 5.0 vol.^{PORE}% PEG 400) decreases by 6 wt.% when the curing temperature increases by 10 °C, while minimal redispersion (93 wt.%) results for powder beds cured at 170 °C (Figure 5- 7). Thus, the curing temperature must be maintained at 150 °C in an argon atmosphere in order that the powder bed maintains its redispersibility.

5.3.4. The Part Retrieval Process

Parts are removed from the powder bed by redispersing the binder-free powder bed regions in de-ionized water. Water is introduced at one side of the powder bed substrate (Figure 5- 8a). The initial infiltration process is carried out slowly (Figure 5- 8b) to allow air to escape and avoid possible part damage due to the buildup of excess air pressure within the powder bed[30,93]. The entire powder bed is immersed in water upon complete saturation, and the binder-free regions expand and begin to redisperse due to osmotic driving forces (Figure 5- 8c). The once imbedded parts are now easily removed (Figure 5- 8d) and residual "slurry" is simply washed away. Small, partially–enclosed features (< 750 μm) are formed by submerging the open face into water allowing the binder-free powder to flow down and out of the printed structure. This step is shown in Figure 5- 8e and Figure 5- 8f. The final part is rinsed thoroughly and dried (Figure 5- 8g). The part retrieval process is also shown for complex shaped MR2 rotors in Figure 5- 9.

5.4. S-3DP MR2 Parts

The S-3DP process has been used to fabricate many different MR2 ceramic parts (ρ_{green} = 2.95 g/cc, ~50%), which are shown in Figure 5- 10. The shape capabilities of the process have been dramatically improved and are realized by comparing the S-3DP RF resonators shown in Figure 5- 10a with those shown in Figure 1-10c. The geometries of the components were very reproducible with a dimensional accuracy of ~± 20 μm.

Figure 5- 11 shows external and internal features for MR2 parts that were removed from the powder bed using the redispersion technique. Open channels (Figure 5- 11a) with

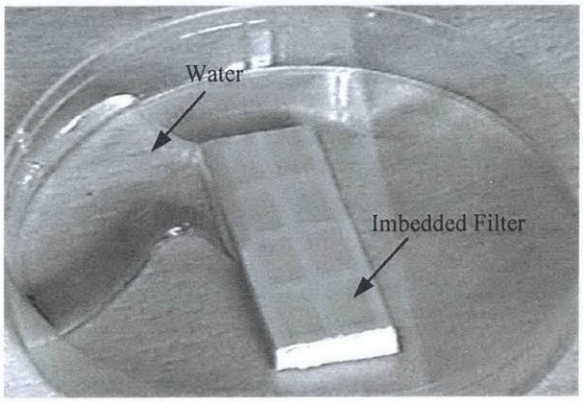

a) t = 0 seconds

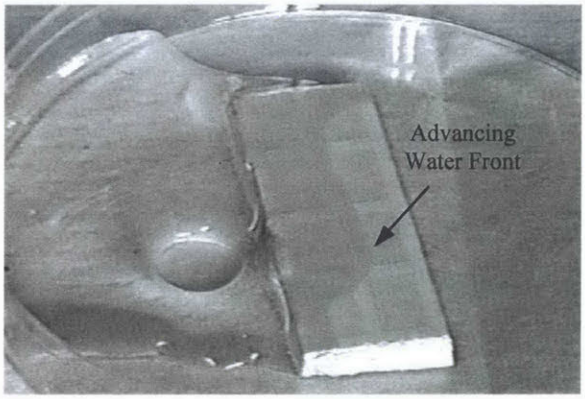

b) t = ~1 to 2 minutes

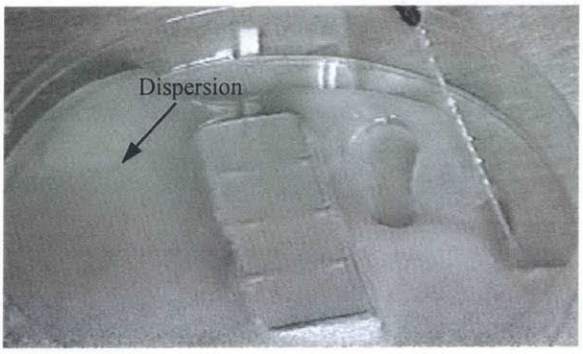

c) t = ~5 minutes

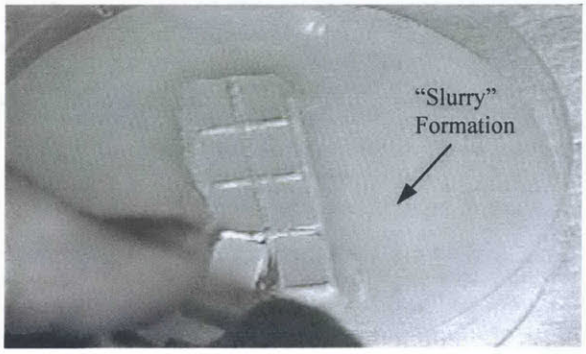

d) t = ~10 minutes

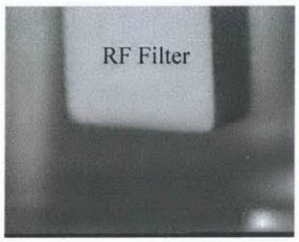

e)

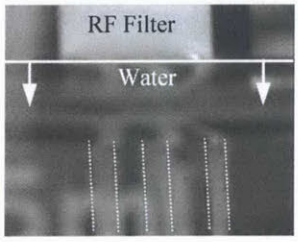

f)

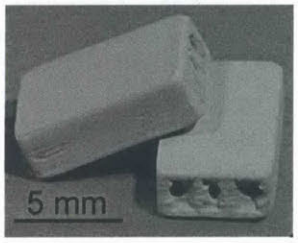

g)

Figure 5- 8: Part Retrieval Process for MR2 RF Filters.

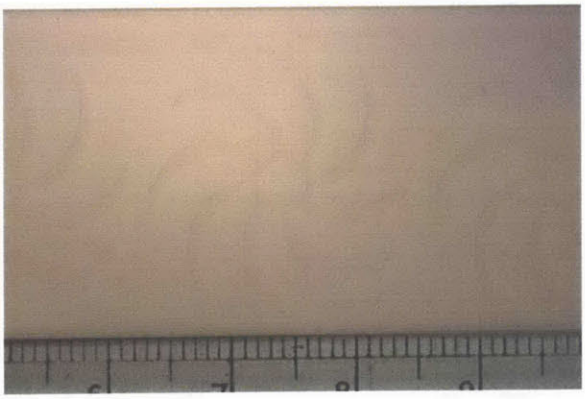

a)

b)

c)

Figure 5- 9: Part Retrieval of MR2 Rotors.

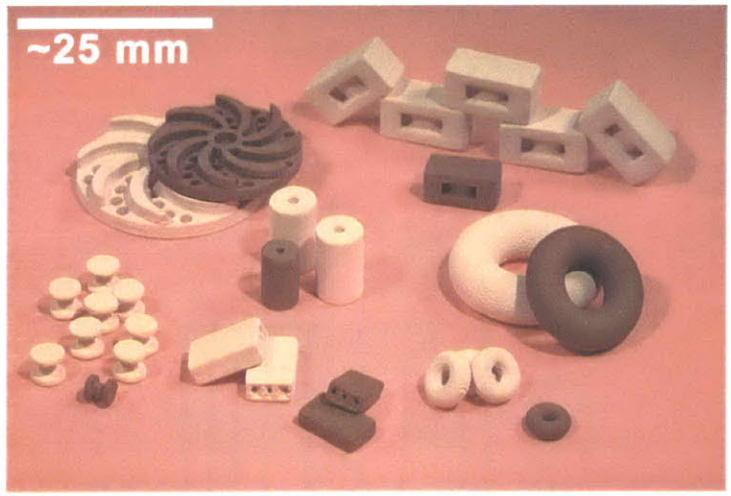

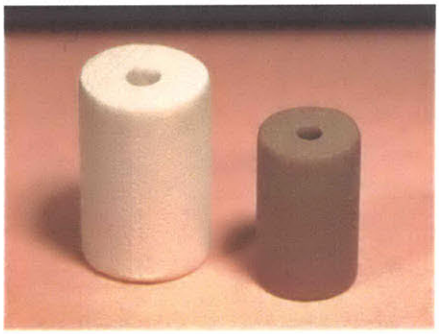

a) RF RESONATOR

b) E-CORE

c) TOROID

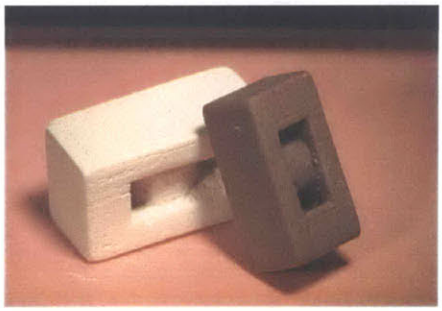

d) DRAM CORE

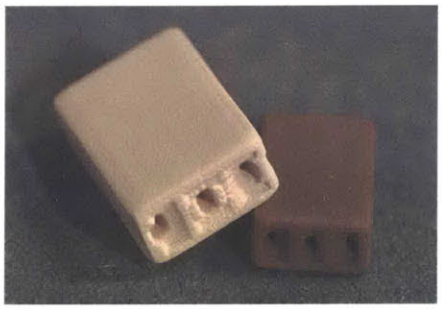

e) RF FILTER

f) ROTOR

Figure 5- 10: MR2 S-3DP Parts.

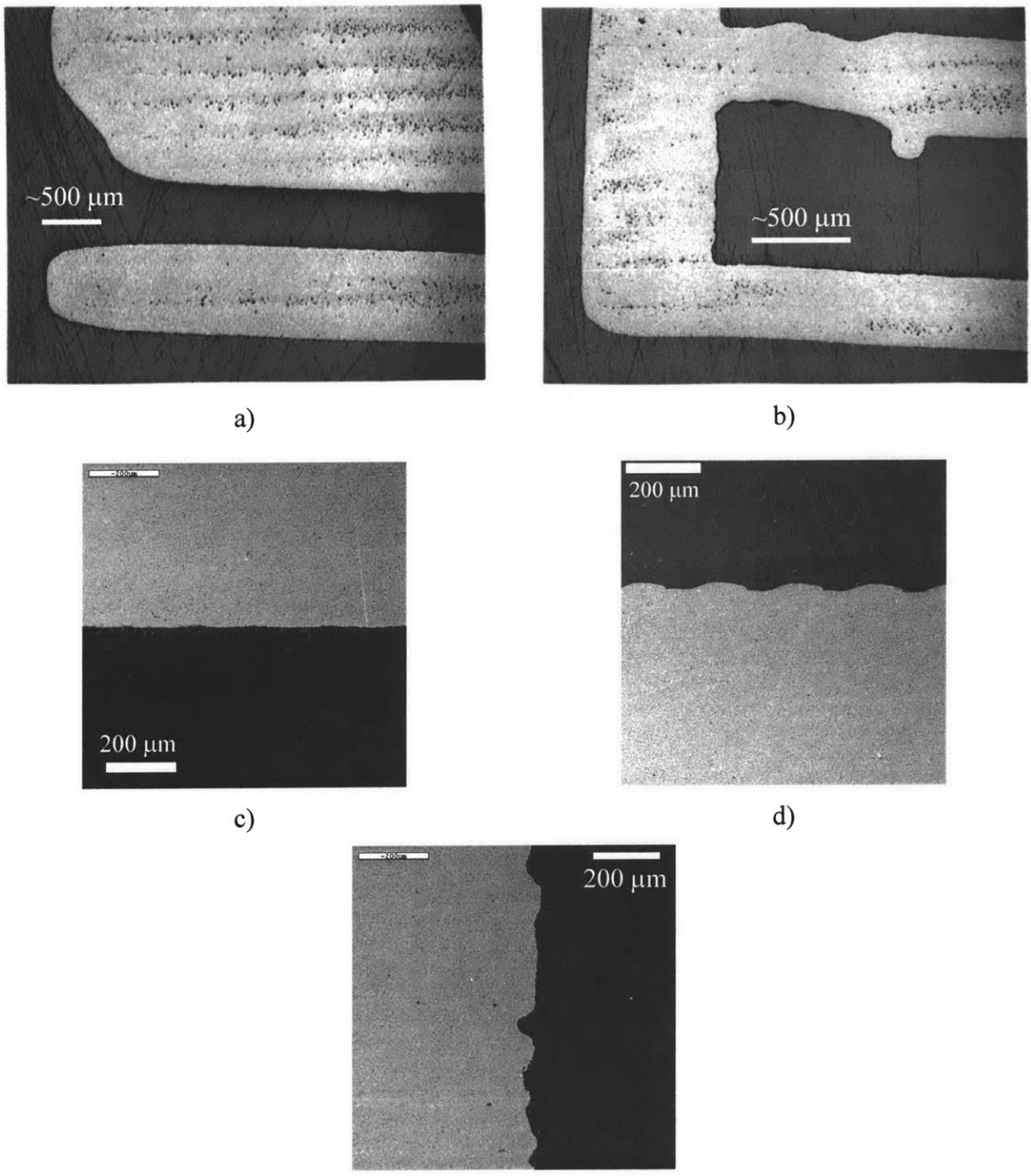

Figure 5- 11: SEM Cross-Sections Showing the External and Internal Features of S-3DP MR2 Components: a) Open Structures, b) Partially-Enclosed Structures, c) Bottom Surface Finish, d) Top Surface Finish and e) Surface Finish of a Side Wall.

dimensions on the order of 750 μm were easily formed by simply washing out the binder-free powder bed. Partially–enclosed features with dimensions of ~ 1 mm were readily formed using the technique described in Section 5.3.4. and are shown in Figure 5- 11b. Both pictures show that the powder bed is redispersed completely and uniformly producing smooth internal surfaces along the channels revealing surface protrusions that result from misplaced binder droplets.

Cross-sections of the top, bottom and side exterior surfaces are shown in Figure 5- 11c, Figure 5- 11d and Figure 5- 11e, respectively. The bottom surface of the parts are very smooth with a maximum peak to valley roughness of ~5 μm. The top surface shows a surface roughness (Δ(peak to valley) = ~20 μm) that is characteristic of the powder bed formation process, which has been described in detail by Saxton[136] and DeBear[137]. Side walls have the highest roughness with a value of ~80 μm.

Most importantly, the part retrieval process has enabled the removal of single binder printed lines from the powder bed. The single binder line, i.e., the binder primitive, is the building block of the printed component, and is shown in cross-section in Figure 5- 12. The MR2 primitive is ~500 μm wide and ~120 μm thick. The surface roughness of vertical walls is greatly influenced by the shape and size of the primitive. The significance of the geometry of the primitive has been demonstrated by reducing the thickness of the printed layers. Decreasing the layer height from 80 μm (Figure 5- 13a) to 55 μm (Figure 5- 13b) clearly improves the surface finish of the component. The enhanced surface finish results from the layer thickness reducing from 67 % to 44 % of the primitive's thickness. This increases the overlap of each primitive in the vertical direction producing a more uniform binder distribution at the surface of the component.

The MR2 radio frequency filters represent the first functioning products produced using the S-3DP process. Filters were fired and metallized according to standard processing operating procedures[138] and are shown in Figure 5- 14a and Figure 5- 14b. Their properties are compared to those of similar die-pressed filters as shown in Figure 5- 14c. It is clear that the S-3DP components functioned as filters having both accurate center frequencies with a respective transmission band; however, the die-pressed proved to have less insertion loss and a wider transmission band. RF-filters with highly complex geometries have been fabricated, which

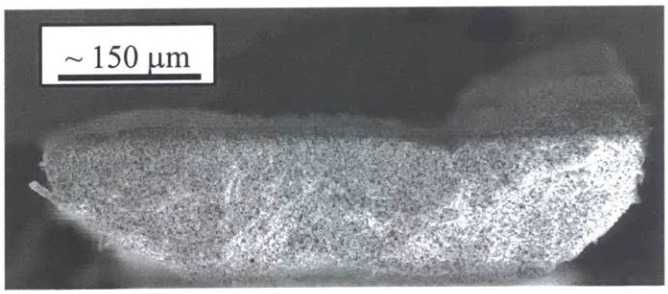

Figure 5- 12: The MR2 "Primitive".

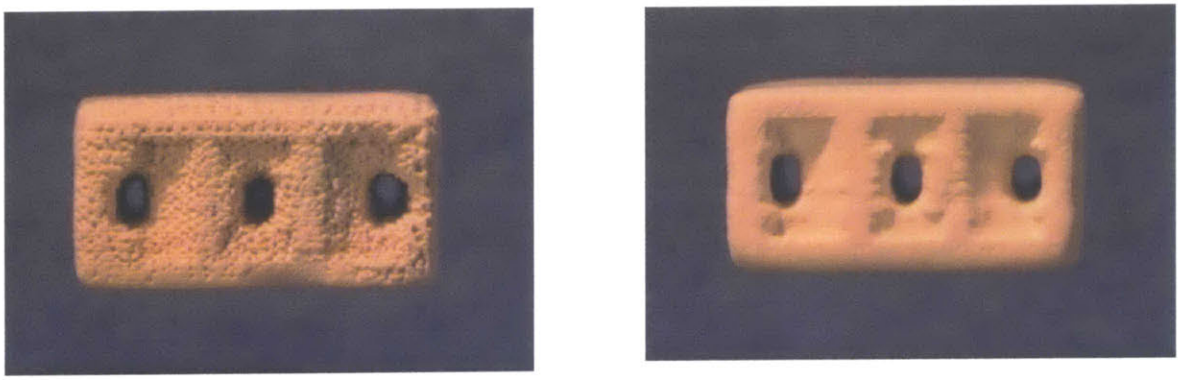

a) b)

Figure 5- 13: The Effect of Layer Height on the Surface Finish of an MR2 RF Filter: a) Layer Height = 80 μm and b) Layer Height = 55 μm.

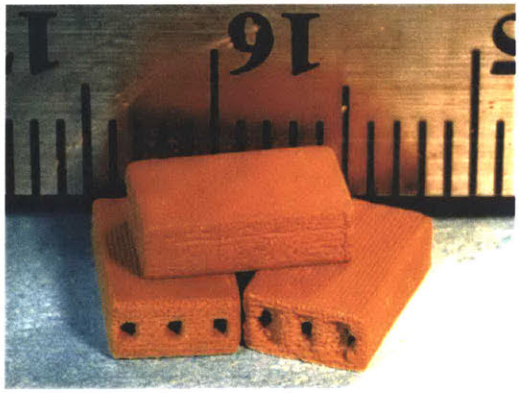

a)

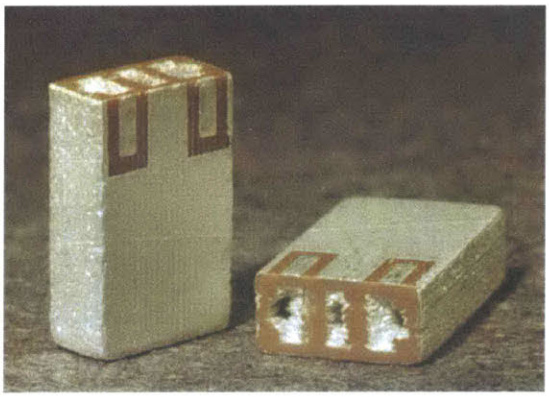

b)

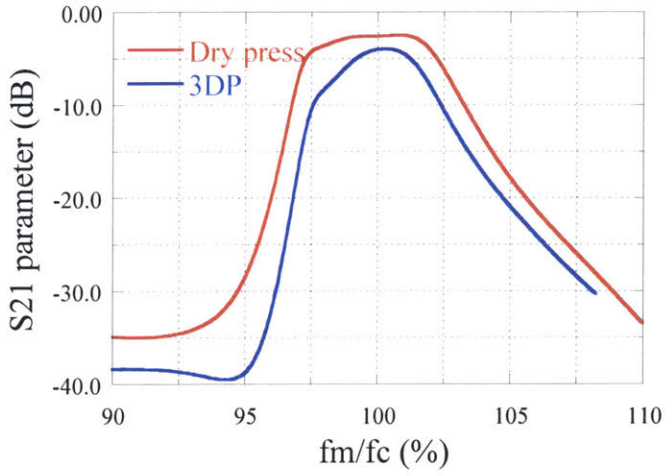

Figure 5- 14: a) Fired MR2 RF Filters, b) Metallized RF Filters and c) Dielectric Properties of S-3DP RF Filter vs. Die-Pressed RF Filter.

emphasizes the advantage of the S-3DP process. These new geometries cannot be formed using conventional fabrication techniques and are expected to reduce attenuation; however, the filters have yet to be characterized due to the need to develop new metallization techniques for complex geometries.

5.4. Conclusions

The fundamental requirements to successful part retrieval has been established as:

$$\sigma_{\text{Powder Bed}}^{Binder-Free} < \pi_{\text{Osmotic Pressure}} < \sigma_{\text{S-3DP "wet" Part}}^{2.5vol.\%PAA}.$$

These three principles to part retrieval have been proven for a wide range of model oxide systems (TiO_2, SiO_2 and Al_2O_3) and, therefore, can be used as guidelines for determining the processing conditions that will promote part removal. The part retrieval process has been successfully applied to the MR2 system to form components with complex geometries. The establishment of a well–defined redispersion process and the development of an effective binder system has yielded components with small feature sizes ranging down to the dimensions of a single printed binder line, i.e., the binder primitive. RF filters have been successfully produced that represent the first functioning ceramic produced using this process.

Chapter Six

Conclusions

Advanced ceramics manufactured using the Slurry-Based 3DP (S-3DP) process represent some of the finest components produced by any solid freeform fabrication process. This achievement is attributed to advancements in the part retrieval process. The development of the part retrieval process has been accomplished by studying the cohesive strength of binder-free agglomerates, the counteracting redispersive forces and the cohesive strength of the printed component.

Flexural strength measurements were used as an effective method for evaluating the cohesive strength of binder-free agglomerates. The average cohesive strength of SiO_2, TiO_2 and Al_2O_3 agglomerates were determined to be 0.157 MPa, 0.177 MPa and 0.340 MPa. The fracture model proposed by Rumpf (Eq. 2.3) was used to determine the dominant inter-particle forces that control the cohesive strength of the agglomerate. The strength of dry, binder-free agglomerates was attributed to van der Waals attraction and to solid bridges that form at the particle necks. The presence of a small amount of an ammonium polycarboxylate dispersant increased the strength of MR2 powder compacts considerably. It is likely that the increased strength resulted from the dispersant acting as a binder at the particle necks.

The fracture toughness of binder-free powder beds was measured with moderate accuracy using standard ASTM techniques. These fracture toughnesses were used to determine the intrinsic flaw sizes within the agglomerates by applying Griffith's energy criterion (Eq. 2.8). The dimensions of the flaws are found to be characteristic of the S-3DP fabrication process. This suggests that the strength of the agglomerated powder bed is influenced by the processing technique and that the flaw size is not necessarily determined by the primary microstructural dimensions.

Deagglomeration was facilitated by the presence of polyethylene glycol (PEG) within the pore structure of the agglomerate. Dissolution of the water–soluble polymer within the pores of the powder bed during the redispersion process reduces the chemical potential of the solvent in the polymer solution relative to that of the pure solvent outside

of the powder bed (Eq. 3.7). This produces an osmotic pressure gradient that forces water into the porous structure and creates a tensile stress on the particle network with magnitudes as high as 0.6 MPa. Thus, the principle to achieving redispersion was to tailor the materials system such that the osmotic pressure exceedes the cohesive strength of the agglomerated structure. This redispersion principle has been successfully applied to the TiO_2, SiO_2 and Al_2O_3 systems using 7.0 vol.^{PORE}% PEG 400 to generate an osmotic pressure of 0.6 MPa, which is greater than the cohesive strength of the binder-free powder beds. A critical PEG concentration of 2.0 vol.^{PORE}% PEG 400 with respect to TiO_2 has been determined, below which redispersion was minimal since the corresponding osmotic pressure of 0.19 MPa was very close to the strength of the powder bed.

The theory of Flory and Huggins also predicts that osmotic pressure decreases as the molecular weight of the polymer increases. Consequently, the redispersion of TiO_2 powder beds decreased dramatically upon increasing molecular weight of PEG from 400 to 6000 g/mole. This reduced the osmotic pressure by an order of magnitude, 600 kPa to 63 kPa, which is below the fracture stress of the powder bed.

The influence of osmotic pressure on the redispersion of MR2 was determined by examining the uniaxial expansion rates of the powder beds during the initial stages of redispersion. The measured expansion rates for the 5.0 vol.^{PORE}% PEG 400 and 5.0 vol.^{PORE}% PEG 1000 powder beds were 58 μm/s and 14 μm/sec. The corresponding osmotic pressures were approximately 0.5 MPa and 0.1 MPa. According to D'Arcy's law (3.23), the resulting liquid fluxes due to these pressure gradients were calculated to be 72 μm/sec and 15 μm/sec. Thus, the expansion is caused by the flow of water into the powder bed due to the osmotic pressure gradient. The osmotic potential forces water into the powder bed during which the initial rate of infiltration is governed by the permeability of the powder bed.

A cross-linkable binder (2.5 vol.% : solids basis), based on polyacrylic acid and glycerol, was used to form components with high dry green strength. The strength and fracture characteristics of the ceramic green bodies are influenced by the mechanical properties of the polyacrylic acid based binder. The nature of these properties, i.e., brittle versus plastic, is dependent on the glass transition of the polymer. The T_g of PAA has

been determined to increase with increasing glycerol concentration in the cured PAA films. The T_g increases due to the formation of a crosslinked network that is created by an esterification reaction between the polyacrylic acid and glycerol under acidic conditions (pH < 7) at 150 °C. Increasing the concentration of the glycerol forced the esterification reaction forward yielding an increase in the ester crosslink density. An increasing crosslink density reduces the degree of mobility that is associated with each unreacted side group, thus causing the glass transition temperature to increase.

All of the imbedded green bars were successfully removed from the binder-free powder bed using the redispersion technique. The ability to retrieve the parts containing the PAA-glycerol system in an aqueous bath verifies that the polymer forms a cross-linked, insoluble binder after curing. The mechanical integrity of the wet green components is tested during the redispersion process. It has been shown that positive osmotic pressures of approximately 0.4 to 0.6 MPa are applied to the green components, as well as the binder-free powder bed, during the redispersion process. The fact that all of the green samples endured the redispersion process suggests that their cohesive strength is greater than the redispersive forces. This was confirmed by measuring the fracture strengths (4-pt bend) of the green SiO_2, TiO_2, Al_2O_3 and MR2 bend bars in a "wet" state. All of the wet strengths were greater than 0.6 MPa. The lowest value of 0.7 MPa was observed for the SiO_2 samples. The wet strength for the TiO_2 and MR2 samples were 1.4 MPa and 3.6 MPa, respectively, while the saturated Al_2O_3 bars were shown to be the strongest with a strength of 5.6 MPa.

The PAA-glycerol binder system improved the dry strength of all of the ceramic materials studied. The strengths of the SiO_2, TiO_2, MR2 and Al_2O_3 green bodies increased by a factor of 8, 11, 15 and 23, respectively, due to 2.5 vol.% crosslinked PAA. The efficacy of crosslinked PAA as a binder is dictated by the adsorption of PAA onto the surface of the ceramic powder. The adsorption of the PAA polymer was shown to vary dramatically with respect to the ceramic powders under constant S-3DP processing conditions. These processing conditions yielded PAA surface adsorptions of ~0.0 $mg*m^{-2}$, 0.6 $mg*m^{-2}$ and 1.1 $mg*m^{-2}$ for the SiO_2, TiO_2 and Al_2O_3 powders. Thus, in the case of Al_2O_3, strong chemical adsorption gave rise to the largest relative strength increase. Nevertheless, it is important to emphasize that the binder increased the strength

of the SiO_2 body by nearly an order of magnitude, even though no adsorption occurred. The increase in strength was likely the result of some physical absorption of PAA onto the SiO2 surface in the dry state.

The PAA binder also had a dramatic effect on the fracture resistance of the green body. The fracture toughnesses of the porous ceramic bars increased by at least an order of magnitude due to presence of the PAA binder. Griffith's theory of brittle fracture (Eq. 4.5) was used to determine the toughnesses of the ceramic bodies. Brittle fracture was confirmed for the Al_2O_3 + PAA system by examining the fracture strength as a function of notch size, which yielded an empirical relationship nearly identical to Eq. 4.5.

Green body fracture was analyzed using stress-strain profiles. The stress-strain behavior of the Al_2O_3 samples was characteristic of a linear elastic body. The SiO_2 bend fracture specimens illustrated a large positive deviation from ideal brittle behavior. This transition from brittle fracture to a more "ductile" failure mechanism may have resulted from different fracture mechanisms since the binder was brittle in both cases. The crosslinked PAA binder intimately bonded with the surface of Al2O3 and, according to Eq. 4.4, the cohesive strength of the binder phase is calculated to be 54 MPa. This value is close to the tensile strength of ester-crosslinked PAA polymers and, therefore, it is concluded that brittle fracture likely occurred through the polymer phase. Essentially no chemical adsorption occurred in the case of SiO_2 and the calculated strength of the binder in the SiO_2 samples was 7 MPa, which is far below the tensile strength of crosslinked PAA. This suggests that fracture occurred along the ceramic-polymer interface since it represented a path of lower resistance. In this case, the particles "detach" from the polymer phase, allowing particles to rearrange and slide against the polymer interface. This mechanical interaction toughened the green body by producing heat and absorbing energy.

The fundamental requirements to successful part retrieval has been established as:

$$\sigma_{\text{Powder Bed}}^{Binder-Free} < \pi_{\text{Osmotic Pressure}} < \sigma_{\text{S-3DP"wet" Part}}^{2.5vol.\%PAA}.$$

These three principles to part retrieval have been proven for a wide range of model oxide systems (TiO_2, SiO_2 and Al_2O_3) and, therefore, can be used as guidelines for determining the processing conditions that will promote part removal. A minimum osmotic pressure

is defined as the cohesive strength of the binder-free powder bed, while a maximum osmotic pressure is represented by the wet green strength of a printed component. The Flory-Huggins theory for the thermodynamics of polymer solutions serves as an essential tool that defines these minimum and maximum osmotic pressures as a function of polymer concentration and molecular weight. The result of these terms provides a processing region for successful part retrieval, which is schematically shown in Figure 6-1. The upper concentration boundary to the processing window is limited to a polymer concentration of 20 vol.^{PORE}% since a primary goal of all ceramic processing techniques is to minimize organic content. Additionally, higher concentrations of polymer will adversely affect the powder bed manufacture process due to high slurry viscosities and uncontrolled casting rates. The lower molecular weight boundary is represented by the minimum molecular weight of the polymeric additive. Figure 6- 2 illustrates that TiO2 and poly(ethylene glycol) aqueous based systems (Table 3- 5) agree very well with the outline criteria.

The part retrieval process has been successfully applied to the MR2 system to form components with complex geometries. The establishment of a well–defined redispersion process and the development of an effective binder system has yielded components with small feature sizes ranging down to the dimensions of a single printed binder line, i.e., the binder primitive.

Clearly, the newly–defined part retrieval process has "uncovered" the printing resolution of the S-3DP process. Future research goals are currently focused on improving part resolution. Holman[39] has initiated primitive studies that focus on the chemical and physical interactions between the binder and the ceramic and their effects on the size and shape of the binder primitive. These studies will help to understand the S-3DP building process on a finer scale and ultimately to improve the overall shape capabilities of the S-3DP process. Secondly, Tsuchiya[139] is developing a "Drop on Demand" printing technique that will provide higher accuracy in the placement of binder droplets during the printing process.

Many manufacturing applications exist for the S-3DP process in the field of ceramics. It has been demonstrated that the process is currently capable of

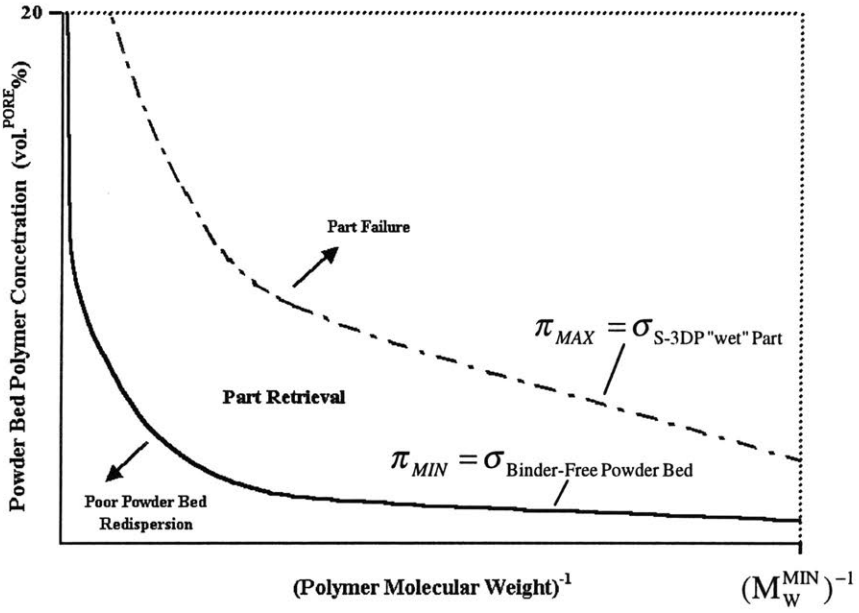

Figure 6- 1: Part Retrieval Process Map.

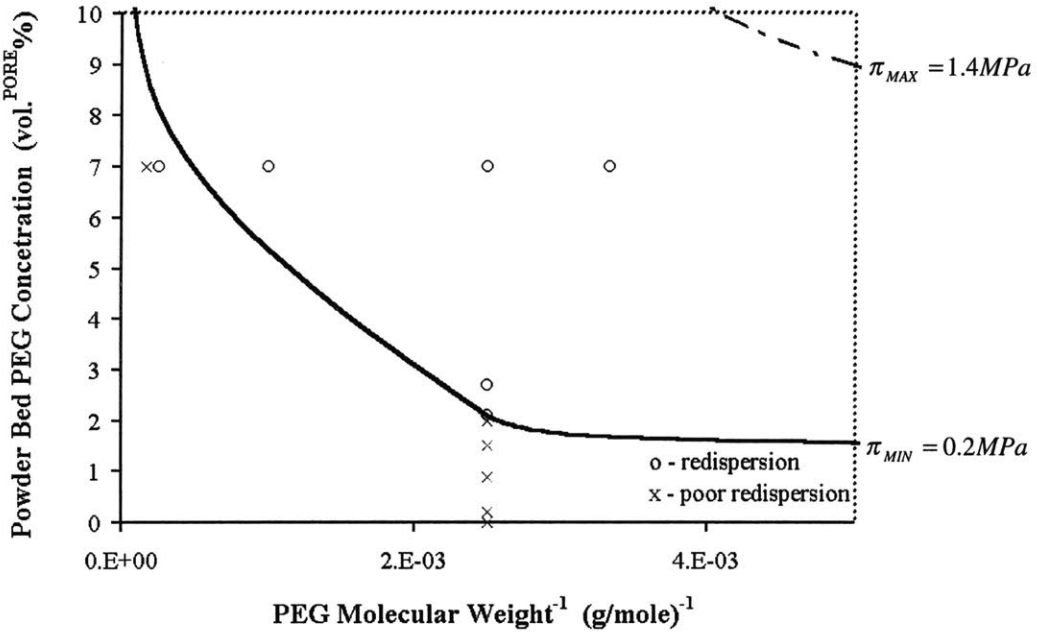

Figure 6- 2: TiO_2 Process Diagram.

fabricating a broad range of electronic ceramics components using the MR2 system. Recently, Holman has successfully fabricated complex shaped Al_2O_3 parts using the outlined part retrieval process.[39] One application is in the area of information display panels that represents a newly–developing technology in which S-3DP may offer reliable fabrication method. Functionally–graded materials are another possible application for S-3DP. Dopants and second phase materials can be printed selectively within the component to change the material properties. Potential products include components with a graded refractive index, such as GRIN lenses or fiber optic pre-forms.

Appendix A
Colloidal Stabilization Theory and MR2 Slurry Formulation

This appendix outlines colloidal stabilization theory and the characterization and formulation of the MR2 slurries used for S-3DP powder bed fabrication.

A.1. Slurry Stabilization Theory

A.1.1. Attractive Forces

Attractive forces exist between all colloidal particles due to omnipresent van der Waals forces. Van der Waals force arises from the interaction of atomic and molecular electric dipoles. These dipoles always attract because of their correlated orientations. There are three different types of van der Waals interactions: permanent dipole – permanent dipole (Keesom), permanent dipole – induced dipole (Debye) and induced dipole – induced dipole (London). Generally, London forces provide the largest contribution to the van der Waals force for colloidal ceramic surfaces. All of the van der Waals forces, F_A, vary as x^{-7}, where x is the separation distance between two bodies. These forces are therefore significant at short separation distances. One exception is the London force. The London component of the van der Waals force is proportional to x^{-8} when separation distances become relatively large (≥ particle radius). The force is retarded because of unsynchronized dipoles due to the delayed propagation of interacting electric fields.

The attractive force due to van der Waals interactions has been determined by Hamaker[49] for two macroscopic bodies in a vacuum (or air). Hamaker's models calculated the attractive potential based on the geometric summation of all molecular interactions in uniformly dense bodies. The physical model most useful for colloidal processing is that of two interacting spheres:

$$V_A = -\frac{A}{6}\left[\frac{2r^2}{H^2-4r^2}+\frac{2r^2}{H^2}+\ln\left(\frac{H^2-4r^2}{H^2}\right)\right], \qquad \text{(A.1)}$$

where r is the radius of the particles, h is the separation distance and H is the distance between the centers of the spheres. At small separations (h << r) Eq A.1 becomes:

$$V_A = -\frac{Ar}{12h}. \qquad \text{(A.2)}$$

Hamaker's calculation of the van der Waals attractive potential between macroscopic bodies assumes that the intervening medium is a vacuum. The computation(s) is not completely accurate since retardation effects of the dispersion medium are neglected. Modern colloidal theory is based on Lifshitz's[75] theory, which defines the attractive forces between particles as a function of their dielectric properties and that of the intervening medium. The modern theory states that van der Waals forces are reduced due to the interaction of the electric field with the dielectric medium. The resulting corrected Hamaker constant is:

$$A = c\left(\frac{\varepsilon_p - \varepsilon_m}{\varepsilon_p + \varepsilon_m}\right)^2, \qquad \text{(A.3)}$$

where ε_m and ε_p are the dielectric constants of the medium and particles, respectively, and c is a proportionality constant. Hamaker constants for common ceramic materials are typically in the range of 10^{-19} J to 10^{-20} J.

Particles in a suspension collide due to gravity and to thermal effects. The thermal energy of a particle is ~ kT = $4.1*10^{-21}$ J at room temperature. Solely in the presence of van der Waals and thermal forces, colliding particles remain attached and flocculation results due to the overwhelming strength of the van der Waals force. An additional repulsive force is required to counteract the attractive force and to avoid flocculation. Two types of stabilization are generally used to offset the attractive potential: electrostatic and steric. The following sections provide the basic theory behind these stabilizing mechanisms. The theory of electrostatic stabilization has been derived by Derjaguin - Landau[74] and by Verwey - Overbeek[78], while Sato[84] and Napper[85] provide additional detail with respect to the stabilization of colloidal dispersions by polymer adsorption.

A.1.2. Repulsive Forces

Electrostatic stabilization occurs due to the electrostatic repulsion produced by the interaction of two diffuse layers of charge. These layers surround the particle because of its non-zero surface charge.

Most oxide ceramics acquire an electric charge on their surface when dispersed in a polar liquid such as water. Many mechanisms are possible for surface charge development. The most common for ceramic particles is adsorption of ions from solution. Hydroxyl groups are typically present on the surfaces of oxides prior to being dispersed in a liquid medium. These OH groups react to form charged surfaces when the particles are introduced into the dispersing solutions. For the case of aqueous suspensions, oxide surfaces become charged by the reactions illustrated in Figure A- 1. The reactions imply that oxide surfaces are positively charged at low pH and negatively charged at high pH. The intermediary pH at which the adsorption of H^+ ions is equal to the concentration of OH^- ions is termed the point of zero charge, PZC. Ions, such as H^+ and OH^-, are referred to as potential–determining ions since they directly develop the effective charge on the particles surface. Ceramics have a wide range of PZC's. Oxides with a low PZC are labeled acid, e.g., SiO_2 at pH 2, while high PZC materials are designated as basic, e.g., MgO at pH 12.

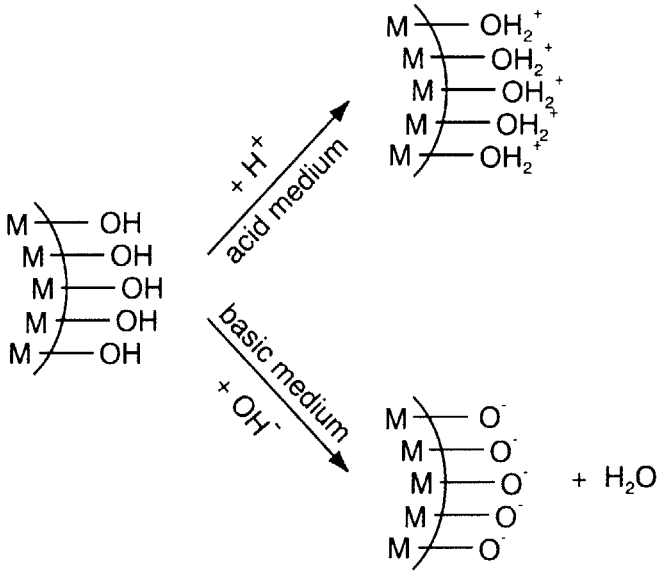

Figure A- 1: Generation of Surface Charge on a Metal Oxide Surface in Acid and Basic Conditions.

The surfaces of the charged particles are surrounded by dissolved species, i.e., ions (or polymer molecules), which form an equal and opposite counter-charge. These species are generally referred to as *counter-ions.* The ions closest to the charged particle are adsorbed to the surface due to strong electrostatic interactions. The adsorbed ions are surrounded by a diffuse layer of charge, which forms due to the thermal motion of the ions. These two simplified regions of charged species represent the electrical double layer, which is illustrated in Figure A- 2 for a positively–charged surface. Figure A- 2 also indicates the presence of *co-ions* in the solution, which have similar charges with respect to the surface. There is a clear difference in the distribution of counter and

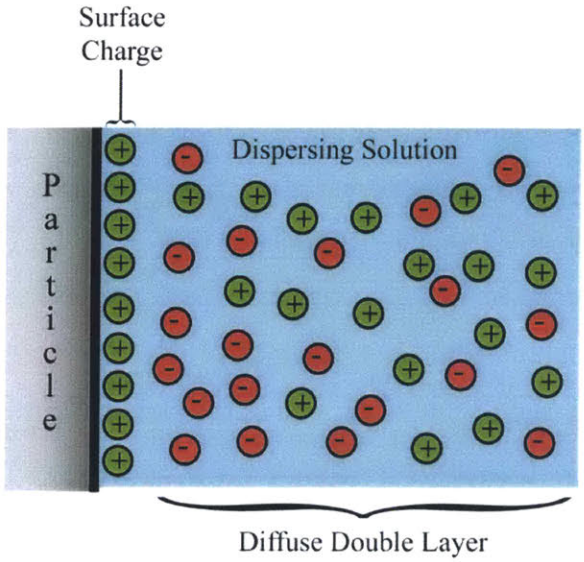

Figure A- 2: The Origin of the Electrical Double Layer.

co-ions in the double layer, and thus the electric potential within the double layer depends on the distance from the surface of the particle, the concentration of ions and the charge of the ions.

The behavior of the electric potential as a function of distance within the double layer can be described using Poisson's equation:

$$\nabla^2\psi(x) = -\frac{4\pi\rho(x)}{\varepsilon}, \qquad \text{(A.4)}$$

where ρ is the charge density and ε is the dielectric constant of the medium. The charge density is determined by summing the contributions of the both the counter– and co–ions:

$$\rho(x)=\sum_i ez_i c_i\,, \tag{A.5}$$

where e is the charge of an electron, z_i is the valence of the *i* ions and c_i is the ion concentration. The Boltzmann distribution is used to describe the concentration profile of each ionic species as a function of thermal and electrostatic energy:

$$c_i = c_i^{\infty}\exp\left(\frac{-ez_i\psi(x)}{kT}\right), \tag{A.6}$$

where c_i^{∞} is the bulk concentration of the ions, k is Boltzmann's constant and T is absolute temperature. Combining Eqs. A.4 through A.6 yields:

$$\nabla^2\psi(x)=-\frac{4\pi e}{\varepsilon}\sum_i z_i c_i^{\infty}\exp\left(\frac{-ez_i\psi(x)}{kT}\right), \tag{A.7}$$

which is known as the Poisson-Boltzmann equation. Eq. A.7 can be reduced to:

$$\nabla^2\psi(x)=\frac{-4\pi e^2\psi(x)}{\varepsilon kT}\sum_i z_i^2 c_i^{\infty}\,, \tag{A.8}$$

using the Debye-Huckel approximation of $\left|\frac{ez_i\psi(x)}{kT}\right|<<1$. Applying the boundary conditions $\psi(x)=0, \nabla^2\psi(x)=0$ at $x=\infty$ and $\psi(x)=\psi_o$ at $x=0$, the solution for Eq. A.8 is:

$$\psi(x)=\psi_o\exp(-\kappa x) \tag{A.9}$$

where

$$\kappa^2=\frac{4\pi e^2}{\varepsilon kT}\sum_i z_i^2 c_i^{\infty}\,. \tag{A.10}$$

The dimensionless argument of the exponential term in Eq. A.9 requires that κ has units of m^{-1}. κ^{-1} is more commonly referred to as the Debye length and it essentially represents the thickness of the repulsive field of the double layer. Eq. A.10 defines three principal properties of the suspending solution that have an important influence the magnitude of the repulsive electric potential:

I) Debye length $\propto z_i^{-1}$

II) Debye length $\propto c^{-\frac{1}{2}}$.

III) Debye length $\propto \varepsilon^{\frac{1}{2}}$

Therefore, it is important to select a solvent with appropriate properties and maintain control over the ionic strength of the solution, $\propto z_i^2 c_i$, in order to maximize the effective size of the electric field.

The approach of charged particles causes their diffuse layers to begin to interpenetrate. This produces an electrostatic repulsive potential, V_R. Derjagiun and Landau have established the relationship between the repulsive potential, Debye length and particle size for two extreme cases:

$$\kappa a >> 1 \Rightarrow V_R = \frac{\varepsilon a \psi_o^2}{2} \ln[1 + \exp(-\kappa(D - 2a))], \qquad \text{(A.11a)}$$

$$\kappa a << 1 \Rightarrow V_R = \left(\frac{\varepsilon a \psi_o^2}{D}\right) \exp(-\kappa(D - 2a)), \qquad \text{(A.11b)}$$

where D is the separation distance between the centers of two particles. For both cases, a small change in the Debye length will have an appreciable impact on the repulsive potential.

According to DLVO theory, the stability of a colloid is determined by a balance of the van der Waals attractive potential and the repulsive potential of the electrical double layer. The total potential energy is given by:

$$V_T = V_A + V_R, \quad \text{(Eq. 2.1 + Eq. 2.11)}. \qquad \text{(A.12)}$$

As the particles approach, the attractive energy increases more rapidly than the repulsive component. The resulting total energy typically passes through a maximum, V_T^{MAX}, which represents an activation barrier to the particle flocculation. There is an abrupt increase in the repulsive energy at very close separations due to Born interactions. "Excited" particles that are able to overcome V_T^{MAX} adhere due to the strong attractive forces present at the primary minimum, V_1. A second, less energetic flocculated state may exist at the secondary minimum.

Stabilization is also commonly achieved by the chemical or physical adsorption of polymer molecules onto the surface of the particles. Generally, the polymer must be composed of two different groups (block structured polymers) in order to obtain stability. One end of the polymer chain has a strong affinity for the surface of the particle, while the opposite end prefers to be surrounded by the solvent.

The source of the stabilizing mechanism is best described by considering the approach of two particles that have polymer molecules attached to their surfaces (Figure A- 3). The polymer chains will begin to interact when the particle separation, h, is approximately twice the length of the polymer chain (Figure A- 3a). As the particles continue to approach (Figure A- 3b), the chains interpenetrate, which effectively corresponds to the separation of the polymer from the solvent. This "demixing" effect causes the chemical potential of the solvent, $\mu_{solvent}$, to increase with respect to the chemical potential of the solution, $\mu_{solution}$, i.e. the free energy of mixing of the system increases. The origin of the steric repulsive force is $\Delta\mu = \mu_{solvent} - \mu_{solution}$, which is commonly described in terms of a positive *osmotic pressure* (Chapter 3). The repulsive force increases at very close separations (Figure A- 3c) due to the elastic compression of the polymer chains. Deformation contributions to the repulsive force can be expressed simply as an entropic effect. Unique chain conformations become

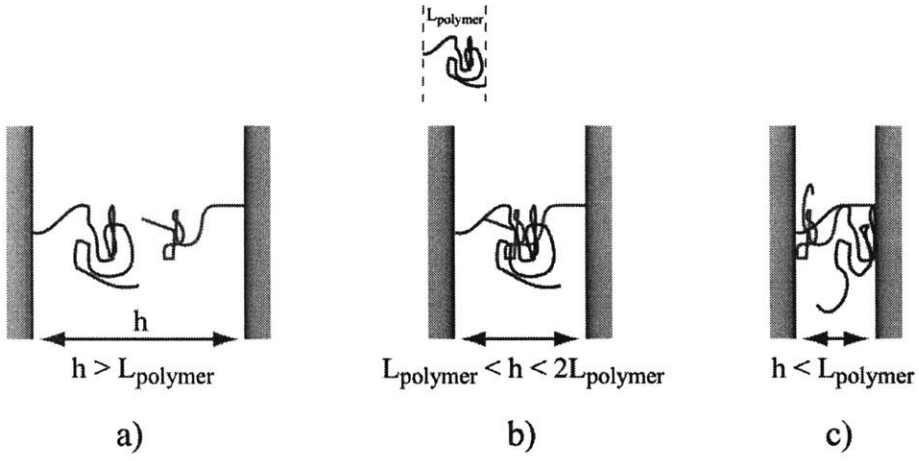

Figure A- 3: Interaction and Interpenetration of Adsorbed Polymer Molecules.

inaccessible. The free energy of the system increases since

$$\Delta G \approx -T\Delta S_{configuration}, \tag{A.13}$$

where $\Delta S_{configuration}$ is the change in the configurational entropy. Using Boltzmann's equation:

$$\Delta S_{configuration} = k\ln(\Omega), \tag{A.14}$$

where Ω is the loss in the number of configurational states of the polymer. The free energy always increases at this stage since $\Omega < 0$.

A less common polymeric stabilizing mechanism is known as depletion stabilization. In this case, the stabilizing polymers are free in solution. The approach of the particles causes the dissolved polymers to be expelled from the intermediating medium. Similar to the previous case, demixing and the thermodynamics of polymer solutions is frequently used to describe the repulsive mechanism.

The most common polymeric dispersants are polyelectrolytes that utilize both electrostatic and steric stabilization mechanisms. Polyelectrolytes have many ionizable side groups. The side groups have a strong impact on the effectiveness of the polymer as a dispersant. The charge of the side groups determines the surface adsorption mechanism, while their electrostatic interactions control the confirmation of the polymer coil. An important application of polyelectrolytes is for dispersing multi-ceramic suspensions. Slurries that contain materials with widely varying ZPCs with flocculate in the presence of a simple acidic or basic solution due to their opposite surface charges. The adsorption of polyelectrolyte molecules onto one or more of the materials produces surfaces with like charges and facilitates multi–component stabilization. Two common polyelectrolytes are polyacrylic acid and polymethacrylic acid, which can be in the form of neutralized salt (NH_4^+ or Na^+) solutions. These polymers have been used to stabilize Al_2O_3[140], ZrO_2[111] and $BaTiO_3$[70,109]. There are numerous other examples that utilize similar polyelectrolytes such as aqueous Si_3N_4 slurries that contain Al_2O_3 and Y_2O_3 as sintering aids[36].

A.2. MR2 Slurry Stabilization

A.2.1. Chemical Stability of MR2 in Aqueous Environments

The solubility of the MR2 powder must be minimized in order to maintain the desired chemistry as well as to promote the stability of the slurry (Eq. A.10). Twenty volume percent MR2 suspensions were used to determine the solubility of MR2 in aqueous systems as a function of time and pH. Starting solutions of pH 4, 6, 8 and 10 were formed using 1.0 M HNO_3 and 1.0 M KOH stock solutions. The suspensions were equilibrated for 0, 4, 8, 24, 48 and 168 hours at 25 °C. The pH of each sample was recorded and the supernatant liquid was removed by centrifuging (DPR-6000, IEC, Wakefield, MA) at 3000 rpm for 60 minutes. The supernatant was filtered to remove particulate impurities and stored in nitrogen. Inductively coupled plasma techniques (ICP – MS, Environmental Health Laboratories, South Bend, IN) were used to determine the concentration of dissolved species, i.e. Ba^{2+}, Nd^{3+} and Bi^{3+}. ICP measurements indicate that the overall solubility of MR2 is very low in aqueous suspensions (< 10 ppm). The dissolution of Bi^{3+} and Nd^{3+} is essentially negligible with concentrations less than 40 ppb for all conditions. The concentration of dissolved barium ions was the largest of the three metal species studied. The concentration of Ba^{2+} increased over time for all initial slurry pH conditions. Slurries with an initial pH of 4 yielded a maximum value of 4.8 ppm after aging for 7 days compared to 1.4 ppm at $pH_{initial}$ 10 (Figure A- 4).

A.2.2. MR2 Slurry Characterization

All slurries were batched using the previously–outlined techniques. ESA measurements[141] were used to characterize the stability of MR2 slurries directly. ESA measurements were performed on 1.0 vol.% suspensions using an acoustic analyzer (ESA 8000, Matec Applied Science, Hopkinton, MA). The zeta potential was measured as a function of pH (titrants: 0.1 M HNO_3 and 0.1 M KOH) and as a function of dispersant concentration (Aron A-30 SL, ammonium polyacrylate, MW = 2400 g/mol, Toagosei, Japan).

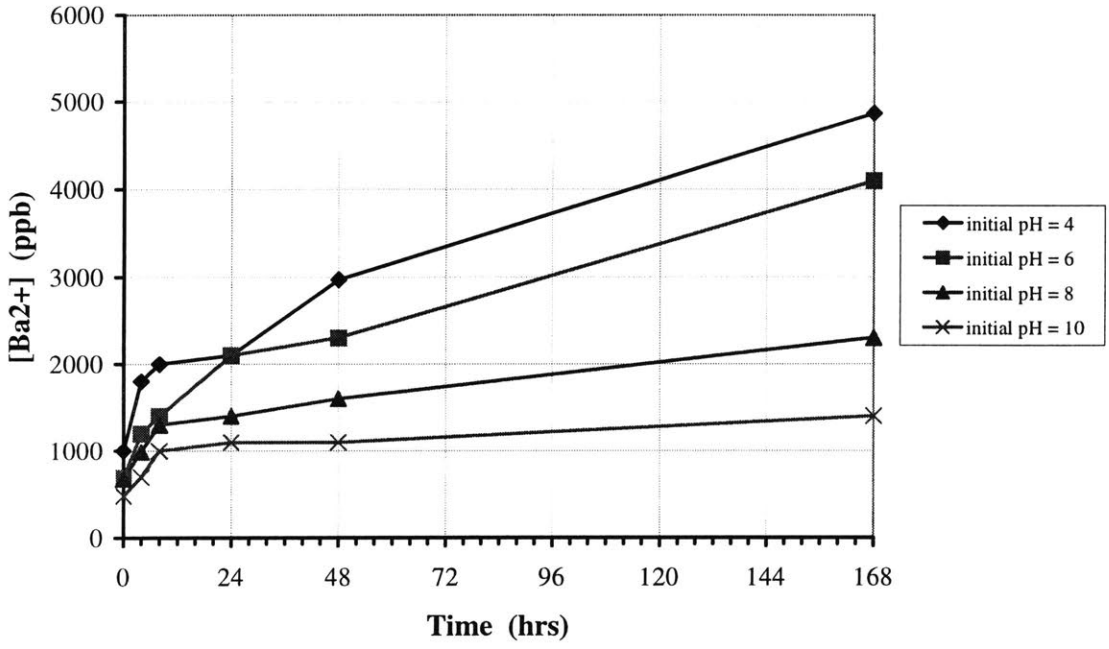

Figure A- 4: The Effect of Time and pH on the Concentration of Dissolved Ba^{2+} in 20 vol.% Aqueous MR2 Slurries.

The potentiometric behavior of a 1.0 vol.% MR2 aqueous slurry is shown in Figure A- 5. The maximum zeta potential is in the acidic end of the potentiometric scan at pH 3 with a value of 69 mV. The potential changes rapidly as the pH increases until the iso-electric point is reached at pH 5.8. The electric potential characteristically becomes more negative as the pH increases and a minimum value of -39 mV is generated at pH 11.

Potentiometric studies indicate that the MR2 system is slightly acidic in nature with an IEP of pH 5.8. This value is similar to reported IEP values for $BaTiO_3$ and TiO_2. The maximum potential was achieved at pH 3. According to DLVO theory, this point represents the maximum electrostatic force. The acidic region is not the favorable region for slurry formulation. The electrostatic forces change rapidly in the pH range of 3 to 6.5. Additionally, dissolution of Ba^{2+} is higher in the low pH range, which will compress the stabilizing double layer (see Eq. A.10). Therefore, the basic pH range is of most interest. The maximum zeta potential achieved in the basic region was –39 mV at pH 11. Even though the dissolution of the Ba^{2+} is minimized and the zeta potential is less sensitive to fluctuations in pH, the potential is inadequate to guarantee a well-dispersed suspension. Flocculation is likely to occur due to the thermal energy of the particles at room temperature, $\frac{kT}{e} = 26\,\text{mV}$.

Aron, an ammonium polyacrylate, was added to the slurry chemistry in order to overcome the instability. Figure A- 6 shows the zeta potential behavior for a 1.0 vol.% slurry at pH 9.5 as a function of Aron concentration (wt.% powder). Upon the addition of Aron, zeta potential scans demonstrated a sharp decrease, reaching –108 mV at 0.5 wt.%. This generates a large increase in the electrostatic repulsion (Eq. A.11), and stabilization is promoted because the resistance to flocculation due to thermal excitation is increased.

Indirect methods were used to characterize the MR2 slurry system. Sedimentation studies were performed on 10 vol.% MR2 slurries that were milled for 16 hours. Figure A- 7 shows the sedimentation results for Aron concentrations of 0.0 wt.%, 0.2 wt.%, 0.4 wt.%, 0.6 wt.%, 0.8 wt.% and 1.0 wt.%. The addition of Aron to

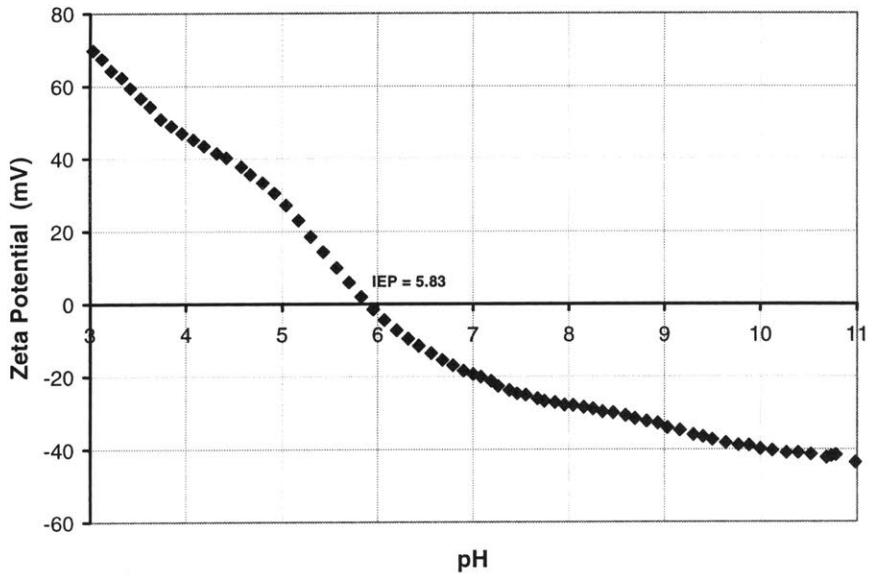

Figure A- 5: Potentiometric Behavior of a 1.0 vol.% MR2 Slurry.

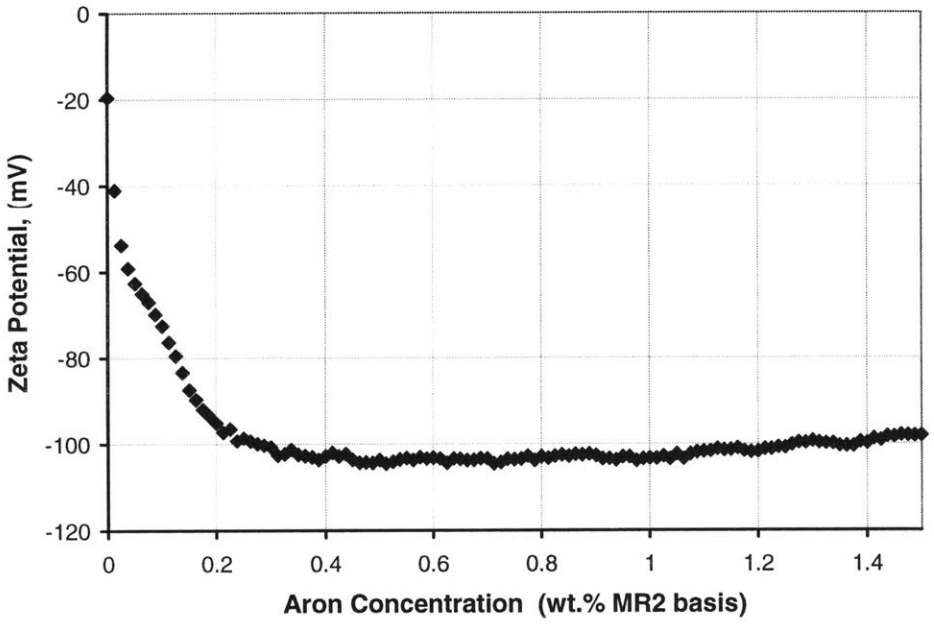

Figure A- 6: The Effect of Aron on the Zeta Potential of a 1 vol.% MR2 Slurry.

the slurry clearly improved the sedimentation characteristics. The densities decreased dramatically upon addition of 0.2 wt.% dispersant. Sedimentation values were highest for dispersant concentrations ranging from 0.2 wt.% to 0.6 wt.%, whereas the densities began to decrease upon further additions of Aron.

Alcohols were added to the slurry solvent in order to minimize differential slip casting defects[37]. Slurries containing no alcohol packed most efficiently. The addition of methanol to the solvent decreased the sedimentation density with respect to the pure water system regardless of the dispersant concentration, as indicated in Figure A- 7. All solvent compositions had a maximum sedimentation density at a dispersant concentration of 0.4 wt.%.

The rheological behavior of the slurries was measured as a function of dispersant concentration and solvent chemistry. Slurry viscosities were measured at 25°C using a cone-and-plate configured viscometer (Hakke CV100, Hakke, Paramus, NJ; Physica UDS 200, Paar Physica, Eatontown, NJ).

Figure A- 8 illustrates the viscosity behavior for slurries having Aron concentrations of 0.0 wt.%, 0.3 wt.%, 0.75 wt.% and 1.5 wt.%. The viscosity of the slurry containing no Aron decreased as the shear rate increased. The minimum viscosity for this suspension was 125 cP, which was measured at the maximum shear rate of 180 sec^{-1}. A considerable decrease in viscosity resulted for the slurries containing Aron. The average viscosities for the slurries containing 0.3 wt.%, 0.75 wt.% and 1.5 wt.% dispersant were 9.7 cP, 10.7 cP and 11.3 cP, respectively, over the shear rate range of 16 sec^{-1} to 180 sec^{-1}.

The viscosities of 30 vol.% MR2 slurries were adversely affected by the addition of methanol (MeOH) to the solvent. All slurries studied contained 0.4 wt.% Aron and had pH values of 9.5. Figure A- 9 illustrates the behavior of 30 vol.% MR2 slurries for solvent compositions of 100 vol.% water, 75 vol.% water – 25 vol.% MeOH and 50 vol.% water – 50 vol.% MeOH. The viscosity at 300 sec^{-1} of the water-based slurry was 7 cP, while the 75-25 vol.% and 50-50 vol.% samples were 17 cP.

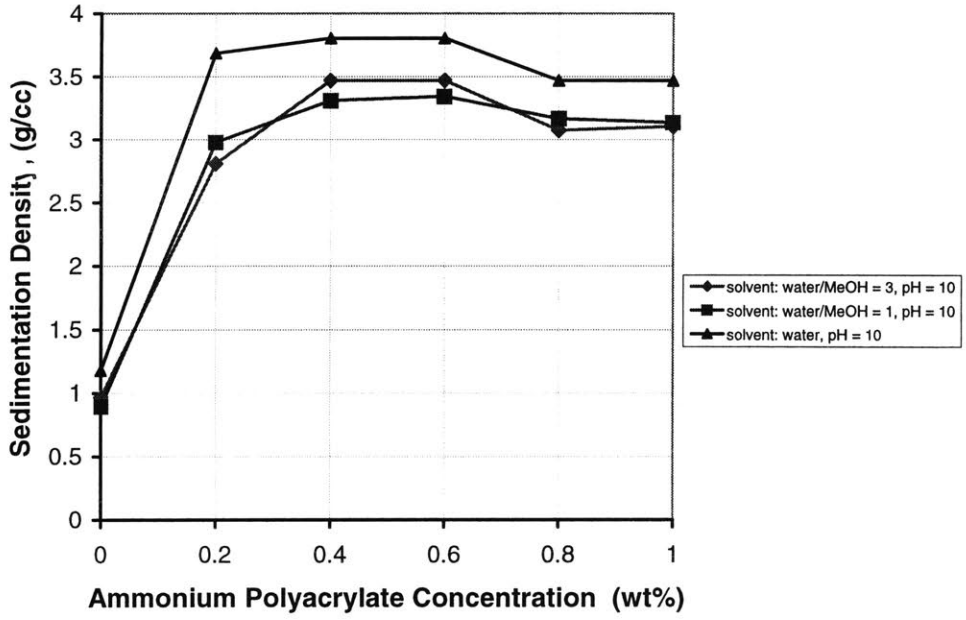

Figure A- 7: Sedimentation Densities of 10 vol.% MR2 Slurries with Varying Solvent Chemistries.

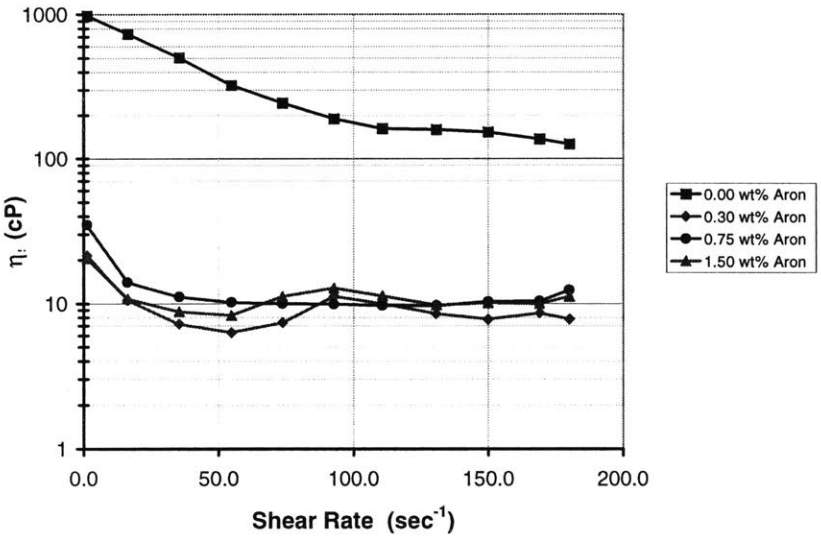

Figure A- 8: Viscosity Characterization for 30 vol.% MR2 Aqueous Slurries as a Function of Aron Concentration (pH 9.5, milled for 16 hrs).

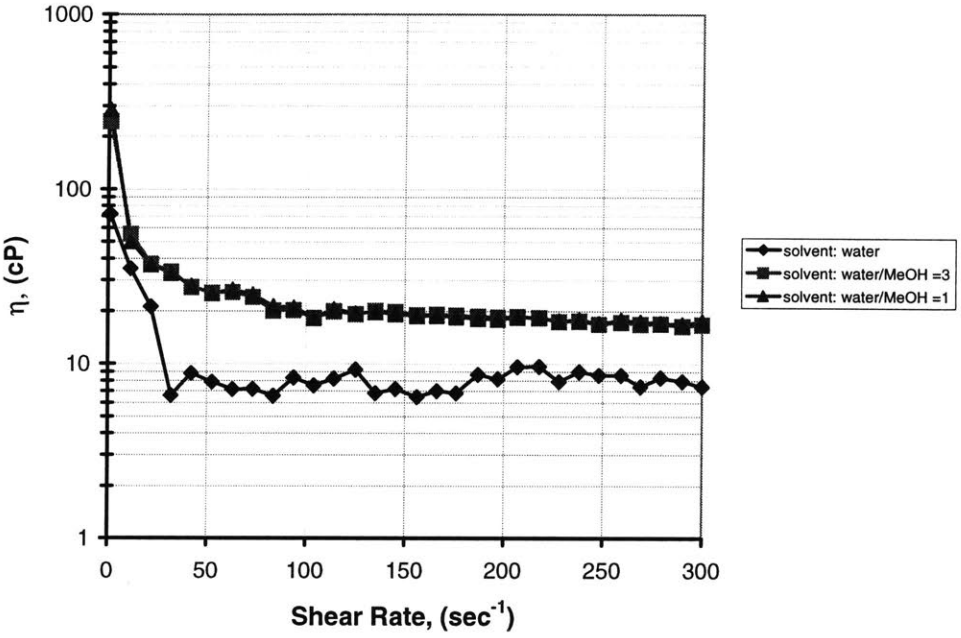

Figure A- 9: Viscosity Characterization for 30 vol.% MR2 Slurries as a Function of Solvent Chemistry (0.4 wt.% Aron, pH 9.5, milled for 16 hrs).

Bibliography

[1]Reed, J., Principles of Ceramic Processing, New York, 1988.

[2]Mistler, R., "Tape Casting: The Basic Process for Meeting the Needs of the Electronics Industry," *American Ceramic Society Bulletin*, **69 (6)**, pp. 1022-1026, 1990.

[3]Rowlands, R., "A Review of the Slip Casting Process," *American Ceramic Society Bulletin*, **45 (1)**, pp. 16-19, 1966.

[4]Schwartzwalder, K., "Injection Molding of Ceramic Materials," *American Ceramic Society Bulletin*, **28 (11)**, pp. 459-461, 1949.

[5]McEntire, B., "Dry Pressing", Ceramics and Glasses, 1991.

[6]Messing, G., C. Markoff and L. McCoy, "Characterization of Ceramic Powder Compaction," *American Ceramic Society Bulletin*, **61 (8)**, pp. 857-860, 1982.

[7]Traff, A., and P. Skotte, "Isostatic Pressing of Ceramic Materials, Methods and Trends," *Powder Metallurgy Int.*, **8**, pp. 65-68, 1976.

[8]Mutsuddy, B., "Injection Molding", Ceramics and Glasses, 1991.

[9]Griffith, M. and J. Halloran, "Freeform Fabrication of Ceramics via Stereolithography," *Journal of the American Ceramic Society*, **79**, pp. 2601-2608, 1996.

[10]Brady, G. and J. Halloran, "Stereolithography of Ceramic Suspensions," *Rapid Prototyping Journal*, **3**, pp. 61-65, 1997.

[11]Hinczewski, C., S. Corbel and T. Chartier, "Stereolithography for Fabrication of Ceramic Three-Dimensional Parts," *Rapid Prototyping Journal*, **4**, pp. 104-111, 1998.

[12]Dickens, P., "Research Developments in Rapid Protoyping," *Proceedings of the Institution of Mechanical Engineers*, **209**, pp. 261-266, 1995.

[13]University, Pennsylvania State, http://www.me.psu.edu/rapidpro/primer/chapter2.htm, 2000

[14]Subramanian, K., N. Vail, et. al., "Selective Laser Sintering of Alumina with Polymer Binder," *Rapid Prototyping Journal*, **1**, pp. 24-35, 1995.

[15]Ahmad, L., L. Eckstrand and J. Pantarotto, "Rapid Prototyping & Solid Freeform Manufacturing," *Canadian Ceramics Quarterly*, pp. 104-107, 1997.

[16]Langdon, R., "A Decade of Rapid Prototyping," *Automotive Engineer*, **22**, pp. 44-46, 1997.

[17]Wang, G., and V. Krstic, "Rapid Prototyping of Ceramic Components - Review," *Journal of the Canadian Ceramic Society*, **67**, pp. 52-58, 1998.

[18]Texas, University, http://lff.me.utexas.edu/sls.html, 2000

[19]Feygin, M., and B. Hsieh, "Laminated Object Manufacturing (LOM): A Simpler Process," *Proceedings of the Solid Freeform Fabrication Symposium*, pp. 123, 1991.

[20]Griffin, E., D. Mumm and D. Marchall, "Rapid Prototyping of Functional Ceramic Composites," *American Ceramic Society Bulletin*, **75**, pp. 65-68, 1996.

[21]Klosterman, D., et. al., "Direct Fabrication of Ceramics and Composites Through Laminated Object Manufacturing (LOM)," *International SAMPE Symposium and Exhibition Proceedings*, **43**, pp. 693-705, 1998.

[22]Klosterman, D. and R. Chartoff, "Structural Composites via Laminated Object Manufacturing," *Solid Freeform Fabrication Symposium Proceedings*, pp. 105-115, 1996.

[23]Cawley, J., A. Heuer, "Computer-Aided Manufacturing of Laminated Engineering Materials," *American Ceramic Society Bulletin*, **75:5**, pp. 75-79, 1996.

[24]Cawley, J., "Computer-aided Manufacturing of Laminated Engineering Materials (CAM-LEM) and Its Applications to the Fabrication of Ceramic Components without Tooling," **1**, pp. 1-5, 1997.

[25]Agarwala, M., et. al., "FDC, Rapid Fabrication of Structural Components," *American Ceramic Society Bulletin*, **75**, pp. 60-65, 1996.

[26]Wu, B., Microstructural Control during Three Dimensional Printing of Polymeric Medical Devices, **Ph.D.**, *Department of Materials Science and Engineering, Massachusetts Institute of Technology*, 1998.

[27]Sachs, E., M. Cima, et. al., "Three Dimensional Printing: Rapid Tooling and Prototypes Directly from a CAD Model," *J. Eng. Ind.*, **114**, pp. 481-488, 1992.

[28]Sachs, E., et. al., "CAD-Casting: Direct Fabrication of Ceramic Shells and Cores by Three Dimensional Printing," *Man. Rev.*, **5**, pp. 117-126, 1992.

[29]Sachs, E., M. Cima, et. al., "Three-Dimensional Printing: The Physics and Implications of Additive Manufacturing," *Annals of the CIRP*, **42**, pp. 257-260, 1993.

[30]Khanuja, S., Origin and Control of Anisotropy in Three Dimensional Printing of Structural Ceramics, **Ph.D.**, *Department of Materials Science and Engineering, Massachusetts Institute of Technology*, 1996.

[31]Yoo, J., Fabrication and Microstructural Control of Advanced Ceramic Components by Three Dimensional Printing, **Ph.D.**, *Department of Materials Science and Engineering, Massachusetts Institute of Technology*, 1996.

[32]Chiang, Y., D. Birnie and W. Kingery, Physical Ceramics, 2, New York, 1997.

[33]Kingery, W., H. Bowen, D. Uhlmann, Introduction to Ceramics, 2, New York, 1976.

[34]Lange, F., "Powder Processing Science and Technology for Increased Reliabilility," *Journal of the American Ceramic Society*, **72(1)**, pp. 3-15, 1989.

[35]Lange, F., B. Velamakanni, J. Chang and D. Pearson, "Colloidal Powder Processing for Structural Reliability: Role of Interparticle Potential on Particle Consolidation," *11th RISO Int. Symposium of Metallurgy and Materials Science*, **September 3-7**, pp. 57-78, 1990.

[36]Moon, J., J. Grau, S. Uhland, M. Cima and E. Sachs, "High Green Density Ceramic Components Fabricated by the Slurry-Based 3DP Process," *Proceedings of the 8th Solid Freeform Fabrication Symposium, University of Texas at Austin,* August 11-13, 1997

[37]Grau, J., Fabrication of Engineered Ceramic Components by the Slurry-Based Three Dimensional Printing Process, **Ph.D.**, *Department of Materials Science and Engineering, Massachusetts Institute of Technology*, 1998.

[38]Aksay, I., and C. Schilling, "Advances in Ceramics; Forming of Ceramics," *Proceedings of the 85th Annual Meeting of the American Ceramic Society*, **9**, pp. 85-93, 1984.

[39]Holman, R., *Personal Communication.*

[40]Uhland, S., R. Holman, M Cima, E Sachs and Y. Enokido, "New Process and Materials Developments in 3-Dimensional Printing, 3DP^{TM}," *Solid Freeform and Additive Fabrication - Proceedings of the Materials Research Society*, **542**, pp. 153-158, 1999.

[41]Rumpf, H., The Strength of Granules and Agglomerates: International Symposium on Agglomeration., London, 1962.

[42]Smith, O., P. Foote and P. Busang, 1929

[43]Kamiya, H., K. Isomura, J. Genji and T. Jun-ichiro, "Powder Processing for the Fabrication of Si_3N_4 Ceramics. I - Influence of Spray-Dried Granule Strength on Pore Size Distribution in Green Compacts," *Journal of the American Ceramic Society*, **78(1)**, pp. 49-57, 1995.

[44]Kuhn, W., Ultrafine Particles, John Wiley and Sons, New York, 1963.

[45]Cheng, D., and F. Valentin, "Fundamental Aspects of Powder Behavior," *Chem. Eng. Sci.*, **23(7)**, pp. 723-738, 1968.

[46]Hartley, P., and G. Parfitt, "Dispersion for Powders in Liquids. 1. The Contribution of the van der Waals Force to the Cohesiveness of Carbon Black Powders," *Langmuir*, **1(6)**, pp. 651-657, 1985.

[47]Rumpf, H., Particle Technology, *Powder Technology Series, Chapman and Hall,*New York, 1975

[48]Shanefield, D., Organic Additives and Ceramic Processing, Kluwer Academic Publishers, Boston, 1995.

[49]Hamaker, H., "The London-van der Waals Attraction Between Spherical Particles," *Physics IV*, **10**, pp. 1058-1072, 1937.

[50]Griffith, A., "The Phenomena of Rupture and Flow in Solids," *Philos. Trans. R. Soc.*, **A221**, pp. 163-198, 1920.

[51]Sutton, H., Characterization of Powder Surfaces, New York, 1976.

[52]Wildman, R., S. Blackburn and M. Gee, "Comparison of Agglomerate Strength Testing Techniques," pp. 1997.

[53]Kendall, K., N. McNalford and J. Birchall, "The Strength of Green Bodies," *British Ceramic Proceedings*, **37**, pp. 255-265, 1986.

[54]Serdy, J., and B. Polito, *Personal Communication.*

[55]Israelachvili, Intermolecular & Surface Forces, *Academic Press*, Boston, 1992.

[56]Cheng, B., M. Gabbay, W. Duffy and G. Fantozzi, "Mechanical Loss and Young's Modulus Associated with Phase Transitions in Barium Titanate Based Ceramics," *J. Mater. Sci.*, **31(18)**, pp. 4951-4955, 1996.

[57]1161-94, ASTM Designation: C, Standard Test Method for Flexural Strength of Advanced Ceramics at Ambient Temperature, 1994

[58]1421-99, ASTM Designation: C, Standard Test Method for Determination of Fracture Toughness of Advanced Ceramics at Ambient Temperature, 1999

[59]Thoma, S., D. Smith and M. Ciftcioglu, "Deterination of Agglomerate Strength Distributions Part 2. Application to Modle Agglomerates," *Powder Technology*, **68**, pp. 63-69, 1991.

[60]Capes, C., "The Correlation of Agglomerate Strength with Size," *Powder Technology*, **5(2)**, pp. 119-125, 1972.

[61]Hartley, P., "The Role of the van der Waals Force in the Agglomeration of Powders Containing Submicron Particles," *Powder Technology*, **42**, pp. 35-46, 1985.

[62]Kendall, K., "Agglomerate Strength," *Powder Metallurgy*, **30(1)**, pp. 28-31, 1987.

[63]Rao, A., "Cohesive Strength of Alumina Powder Compacts," *Ceram. Int.*, **13(3)**, pp. 139-143, 1987.

[64]Maskara, A., and D. Smith, "Agglomeration during the Drying of Fine Silica Powders, Part II: The Role of Particle Solubility," *Journal of the American Ceramic Society*, **80(7)**, pp. 1715-1722, 1997.

[65]Iler, R., The Chemistry of Silica, John Wiley & Sons, New York, 1979.

[66]Lide, D., CRC Handbook of Chemistry and Physics, CRC Press, Boca Raton, 1991.

[67]Ziemniak, S., M. Jones, K. Combs, "Solubility Behavior of Titanium(IV) Oxide in Alkaline Media at Elevated Temperatures," *GE Industrial & Power Systems - Knolls Atomic Power Laboratory,* **Technical Report KAPL-4729**, pp. 1-31, 1992

[68]Wefers, K., and C. Misra, "Oxides and Hydroxides of Aluminum", Alcoa Technical Paper No. 19, Alcoa Laboratories, 1987

[69]Lencka, M., and R. Riman, "Thermodynamic Modeling of Hydrothermal Synthesis of Ceramic Powders," *Chem. Mater.*, **5**, pp. 61-70, 1993.

[70]Jean, J.-H., and H.-R. Wang, "Dispersion of Aqueous Barium Titanate Suspensions with Ammonium Salt of Poly(methacrylic acid)," *Journal of the American Ceramic Society*, **81(6)**, pp. 1589-1599, 1998.

[71]Kendall, K., N. Alford and J. Birchall, "A New Meethod for Measuring the Surface Energy of Solids," *Nature*, **325(26)**, pp. 794-795, 1987.

[72]Chiu, R., Drying of Granular Ceramic Films, **Ph.D.**, *Department of Materials Science and Engineering, Massachusetts Institute of Technology*, 1991.

[73]Bruce, R., "Surface Energy of Ceramics: I. Calculations of Surface Free Energies," *Sci. Ceram.*, **2**, pp. 359-367, 1965.

[74]Derjaguin, B., and L. Landau, "Theory of the Stability of Strongly Charged Particles in Solutions of Electrolytes," *Acta Physiochem: URSS*, **14**, pp. 633-662, 1941.

[75]Lifshitz, E., "The Theory of Molecular Attractive Forces Between Solids," *Sov. Phys. JETP*, **2**, pp. 73-83, 1956.

[76]Shaw, D., Introduction to Colloid and Surface Chemistry, Butterworth Group, London, 1970.

[77]van Olphen, H., An Introduction to Clay Colloid Chemistry, *Interscience*, New York, 1963

[78]Verwey, E., and J. Overbeek, Theory of the Stability of Lyophobic Colloids: the Interaction of Sol Particles Having an Electric Double Layer, New York, 1948.

[79]Vaslin-Reimann, S., F. Lafuma and R. Audebert, "Reversible Flocculation of Silica Suspensions by Water-Soluble Polymers," *Colloid Polym. Sci.*, **268**, pp. 476-483, 1990.

[80]Pietsch, W., E. Hoffman and H. Rumph, "Tensile Strength of Moist Agglomerates," *Ind. Eng. Chem.*, **8(1)**, pp. 58-62, 1969.

[81]Song, J., and J. Evans, "A Die Pressing Test for the Estimation of Agglomerate Strength," *Journal of the American Ceramic Society*, **77(3)**, pp. 806-814, 1994.

[82]Flory, P., Principles of Polymer Chemistry, Cornel University Press, Menasha, Wisconsin, 1953.

[83]Huggins, M., "Thermodynamics of Polymer Solutions," *Phys. Chem.*, **8**, pp. 123-152, 1975.

[84]Sato, T., and R. Ruch, Stabilization of Colloidal Dispersions by Polymer Adsorption, Marcel Dekker, New York, 1980.

[85]Napper, Polymeric Stabilization of Colloidal Dispersions, Boston, 1983.

[86]McClendon, J., and G. Somers, "Simple Large Scale Ultrafiltration Using Osmotically Forced Dialysis," *Plant Physiol.*, **30**, pp. 485, 1950.

[87]Tsao, T., D. Evans, R. Rand and V. Parsegian, "Osmotic Stress Measurements of Dehexadecyldimethylammonium Acetate Bilayers as a Function of Temperature and Added Salt," *Langmuir*, **9**, pp. 1993.

[88]Prouty, M., A. Schechter and V. Parsegian, "Chemical Potential Measurements of Deoxyhemoglobin S Polymerization: Determination of the Phase Diagram of an Assembling Protein," *Journal of Molecular Biology*, **184**, pp. 517-528, 1985.

[89]Miller, K., and C. Zukoski, "Osmotic Consolidation of Suspensions and Gels," *Journal of the American Ceramic Socitey*, **77(9)**, pp. 2473-2478, 1994.

[90]Parsegian, V., R. Rand, N. Fuller and D. Rau, "Osmotic Stress for the Direct Measurement of Intermolecular Forces," *Methods Enzymol.*, **127**, pp. 400-416, 1986.

[91]Uhland, S., and M. Cima, "The Strength of Binder-Free Ceramic Agglomerates," *Journal of the American Ceramic Society*, **to be submitted**, pp. 2000.

[92]Barringer, E., The Synthesis, Interfacial-Electrochemistry, Ordering and Sintering of Mono-Disperse TiO_2 Powders, **Ph.D.**, *Department of Materials Science and Engineering, Massachusetts Institute of Technology*, 1983.

[93]Heertjes, P., W. Witvoet, "Some Aspects of the Wetting of Powders," *Powder Techology*, **3**, pp. 393-343, 1970.

[94]Walker, W., et. al., "Adsorption Behavior of Poly(ethylene glycol) at the Solid/Liquid Interface," *Journal of the American Ceramic Society*, **82(3)**, pp. 585-590, 1999.

[95]Mathur, S., and B. Moudgil, "Adsorption Mechanisms of Poly(Ethylene Oxide) on Oxide Surfaces," *Journal of Colloid and Interface Science*, **196**, pp. 92-98, 1997.

[96]Waggoner, R., F. Blum, and J. Lang, "Diffusion in Aqueous Solutions of Poly(ethylene glycol) at Low Concentrations," *Macromolecules*, **28**, pp. 2658-2664, 1995.

[97]Money, N., "Osmotic Pressure of Aqueous Polyethylene Glycols," *Plant Physiol.*, **91**, pp. 766-769, 1989.

[98]Michel, B., and M. Kaufmann, "The Osmotic Potential of Polyethylene Glycol 6000," *Plant Physiol*, **51**, pp. 914-916, 1973.

[99]Michel, B., "Evaluation of the Water Potentials of Solutions of Polyethylene Glycol 8000 Both in the Absence and Presence of Other Solutes," *Plant Physiol.*, **72**, pp. 66-70, 1983.

[100]Applegate, H., "Freezing-Point Depressions of Hoagland's 'Carbowax' Systems," *Nature*, **186**, pp. 232-233, 1960.

[101]Rogers, J., and T. Tam, "Solution Behavior of Polyethylene Glycols in Water Using Vapor Pressure Osmometry," *Can. Journal Pharm. Sci.*, **12**, pp. 65-70, 1977.

[102]Eliassi, A., H. Modarress and G. Mansoori, "Measurement of Activity of Water in Aqueous Poly(ethylene glycol) Solutions (Effect of Excess Volume on the Flory-Huggins χ-Parameter)," *J. Chem. Eng. Data*, **44**, pp. 52-55, 1999.

[103]Descamps, M., G. Ringuet, D. Leger and B. Thierry, "Tape Casting: Relationship Between Organic Constituents and the Physical and Mechanical Properties of Tapes," *Journal of the European Ceramic Society*, **15**, pp. 357-362, 1995.

[104]Kristofferson, A., E. Roncari and C. Galassi, "Comparison of Different Binders for Water-Based Tape Casting of Alumina," *Journal of the European Ceramic Society*, **18**, pp. 2123-2131, 1998.

[105]Hotza, D., and P. Greil, "Review: Aqueous Tape Casting of Ceramic Powders," *Materials Science and Engineering*, **A202**, pp. 206-217, 1995.

[106]Kristofferson, A., and E. Carlstrom, "Tape Casting of Alumina in Water with an Acrylic Latex Binder," *Journal of the European Ceramic Society*, **17**, pp. 289-297, 1997.

[107]Wu, X., and T. Donato, "Acrylic Binders for Alumina and othe Non-Clay Ceramic Extrusions," *Ceramic Trans.*, **62**, pp. 281-288, 1996.

[108]Wu, X., et. al., "Acrylic Binders for Dry Pressing Ceramics," *American Ceramic Society Bulletin*, **76(1)**, pp. 49-52, 1997.

[109]Chen, Z.-C., T. Ring and J. Lemaitre, "Stabilization and Processing of Aqueous $BaTiO_3$ Suspension with Polyacrylic Acid," *Journal of the American Ceramic Society*, **75(12)**, pp. 3201-3208, 1992.

[110]Vedula, R., and H. Spencer, "Adsorption of Poly(Acrylic Acid) on Titania and Zirconia Colloids," *Colloids and Surfaces*, **58**, pp. 99-110, 1991.

[111]Biggs, S., and T. Hardy, "Electrosteric Stabilization of Colloidal Zirconia with Low-Molecular Weight Polyacrylic Acid," *J. Chem. Soc. Faraday Trans.*, **90(22)**, pp. 3415-3421, 1994.

[112]Santhiya, D., G. Nandini, S. Subramanian, K. Natarajan and S. Malghan, "Effect of Polymer Molecular Weight on the Adsorption of Polyacrylic Acid at the Alumina-Water Interface," *Colloids and Surfaces A-Physicochemical and Engineering Aspects*, **133**, pp. 157-163, 1998.

[113]Buchholz, F., and A. Graham, Modern Superabsorbent Polymer Technology, New York, 1998.

[114]de Barra, E., and R. Hill, "Influence of Poly(acrylic acid) Content on the Fracture Behavior of Glass Polyalkenoate," *Journal of Materials Science*, **33**, pp. 5487-5497, 1998.

[115]Gedde, U., Polymer Physics, New York, 1995.

[116]Cauich-Rodriquez, J., S. Deb and R. Smith, "Effect of Cross-linking Agents on the Dynamic Mechanical Properties of Hydrogel Blends of Poly(acrylic acid) - Poly(vinyl alcohol - vinyl acetate)," *Biomaterials*, **17(23)**, pp. 2259-2264, 1996.

[117]Onoda, G., "Theoretical Strength of Dried Green bodies with Organic Binders," *Journal of the American Ceramic Society*, **59(5)**, pp. 236-239, 1976.

[118]Uhland, S., J. Moon and M. Cima, "Additive Enhanced Redispersion of Agglomerates," *Journal of the American Ceramic Society*, **to be submitted**, pp. 2000.

[119]Brandrup, J., E. Immergut and E. Grulke, Polymer Handbook, New York, 1999.

[120]Cowie, J., I. McEwen and M. Garay, "Molecular Weight and Tacticity Effects on the Glass Transition of Pol(Arcylic Acid)," *Eur. Polym. J.*, **23(11)**, pp. 917-920, 1987.

[121]Flaningham, O., The Electrokinetic Properties of Goethite, **M.S.**, *Mining and Technology, Michigan College*, 1960.

[122]Johansen, P., and A. Buchanan, *Australian J. Chem*, **10**, pp. 398, 1957

[123]Purcell, G., and S. Sun, *Trans. AIME*, **6**, pp. 226, 1963

[124]Flory, P., "Molecular Size Distribution in Three Dimensional Polymers. I. Gelation," *J. Amer. Chem. Soc.*, **63**, pp. 3082-3090, 1941.

[125]Peppas, N., and F. Buchholz, Superabsorbent Polymers Science and Technology, Washington, DC, 1994.

[126]Weininger, S., and F. Stermitz, Organic Chemistry, New York, 1984.

[127]Ponomariova, T., et. al., "Influence of the Crosslinks Density on the Crystallization of Water in PAA Gels," *Polymer*, **38(14)**, pp. 3561-3564, 1997.

[128]Balakrishnan, M., and R. Huang, "Pervaporation Separation of Pentane-Alcohol Mixtures through Ionically Crosslinked Blended Membranes. 1. Thermal Measurements, Electron-Microscopy adn Tensile Studies.," *Angewandte Makromolekulare Chemie*, **191**, pp. 39-69, 1991.

[129]Greenberg, A., and R. Kusy, "Influence of Crosslinking on the Glass Transition of Poly(Acrylic Acid)," *J. Applied Polym. Sci.*, **25(8)**, pp. 1785- 1788, 1980.

[130]Vinogradov, S., and R. Linnell, Hydrogen Bonding, New York, 1971.

[131]Ruckenstein, E, and L. Liang, "Poly(acrylic acid) - Poly(vinyl alcohol) Semi- and Interpenetrating Polymer Network Pervaporation Membranes," *Journal of Applied Polymer Science*, **62(7)**, pp. 973-987, 1996.

[132]Wachtman, J., Mechanical Properties of Ceramics, John Wiley & Sons, Inc., New York, 1996.

[133]McGary, C., "Degradation of Poly(ethylene Oxide)," *Journal of Polymer Science*, **45**, pp. 51-57, 1960.

[134]Reich, L., "Autoxidation of Poly(alkylene glycols) in Solution," *Journal of Applied Polymer Science*, **13**, pp. 977-988, 1969.

[135]Busby, D., Union Carbide, Personal Communication.

[136]Saxton, P., Reducing Powder Bed Layer Defects in Slurry-Based Three Dimensional Printing, **M.S.**, *Department of Mechanical Engineering, Massachusetts Institute of Technology*, 1999.

[137]DeBear, B., Slurry Deposition of High Quality Layers for 3D Printing, **M.S.**, *Department of Mechanical Engineering, Massachusetts Institute of Technology*, 1999.

[138]Enokido, Y., *Personal Communication.*

[139]Tsuchiya, H., *Personal Communication.*

[140]Cesarano, J. and I. Aksay, "Stability of Aqueous α-Al_2O_3 Suspensions with Poly(methacrylic acid) Polyelectrolyte," *Journal of the American Ceramic Society*, **71(4)**, pp. 250-255, 1988.

[141]Rahaman, M., Ceramics Processing and Sintering, New York, 1995.